

POLITECNICO DI MILANO

SCHOOL OF INDUSTRIAL AND INFORMATION ENGINEERING

Master in Engineering Physics

Specialization: Photonics and Nano Optics



**Ytterbium-fiber laser system for detection
of deposited chemical warfare agents
by coherent Raman scattering**

Supervisor: Prof. Ing. Nicola Coluccelli

Students:

SIMONE FRANCAVILLA Matr. 897561

DANILO LENTINI Matr. 898029

Academic Year 2018/2019

Contents

1	Introduction	1
2	Theoretical Principles	4
2.1	Mode-Locked Oscillators	4
2.1.1	Frequency Domain Description	5
2.1.2	SESAM - Semiconductor Saturable Absorber Mirrors	9
2.1.3	Cavity Dispersion in Femtosecond Mode-Locked Lasers	14
2.2	Fiber Amplifiers and SPM-enabled Spectral Broadening in Optical Fibers	18
2.2.1	Fiber Amplifiers	18
2.2.2	SPM-enabled Spectral Broadening in Optical Fibers	22
2.3	Raman Scattering	30
2.3.1	Spontaneous Raman Scattering	30
2.3.2	Coherent Raman Scattering	37
2.3.3	FT-CARS - Fourier Transform CARS	42
3	Laser Source	45
3.1	Historical Introduction	45
3.2	Experimental Setup	47
3.2.1	Pulse Generation	47
3.2.2	Pulse Amplification	48

3.2.3	Spectral Broadening and Pulse Compression	49
3.2.4	Autocorrelation Setup	49
3.3	Setup Components	51
3.3.1	Low Power Ytterbium Fiber Laser	51
3.3.2	High Power Pump Diode	52
3.3.3	Amplification Fibers	53
3.3.4	Photonic Crystal Fiber	54
3.4	Broadband Ultrashort Pulse delivered for FT-CARS	56
4	FT-CARS enabled by Michelson Interferometer	58
4.1	Experimental Setup	59
4.1.1	Transmission Configuration	59
4.1.2	Back-reflection configuration	63
4.1.3	Transmission Configuration with a Resonant Galvo-Mirror	65
4.1.4	Electronics	67
4.2	Results and Discussion	71
4.2.1	Transmission Configuration	71
4.2.2	Back-reflection Configuration	82
4.3	Sampling Process	96
5	Conclusions	102
	Bibliography	102

List of Figures

2.1.1 Mode amplitudes vs frequency for a mode-locked laser.	5
2.1.2 Behavior of the squared amplitude of the electric field for $n = 9$ modes with locked phase and equal amplitude E_0	6
2.1.3 SESAM scheme in a cavity.	9
2.1.4 Quarter-wave Bragg Mirror.	10
2.1.5 Refractive index profile and optical intensity distribution. [1] . .	11
2.1.6 Time dependent absorption for different saturation parameters. .	13
2.1.7 Phase velocity and group velocity in a dispersive medium.	15
2.1.8 Time delay dispersion for two pulses.	16
2.2.1 Single-clad, co-pumped fiber amplifier.	19
2.2.2 Cladding pumped, double-clad fiber amplifier.	20
2.2.3 (a) Power profile of the input pulse; (b) Generated wavelengths as a function of time, for different propagation length z in the fiber.	24
2.2.4 (a) Spectrum evolution versus fiber length; (b) Optical spectrum after propagating 6 cm in the fiber. [2]	25
2.2.5 Optical spectra for simulations after 6 cm propagation, including SPM and SS (blue curve) or including SPM, SS, and SRS (red curve). Inset: optical pulse at the fiber output when the simulation includes SPM, SS, and SRS. [2]	26
2.2.6 (a) Spectrum for simulations after 6 cm propagation including SPM, SS, SRS, and GVD ($5 \text{ fs}^2/\text{mm}$). Inset: close-up of the spectral range from 600-800 nm . (b) Corresponding pulse. Inset: close-up of the pulse envelope in the temporal range of 250-300 fs. [2]	27

2.2.7 Evolution of 50 nJ pulses propagating in 6 cm fiber and evolution of 150 nJ pulses propagating in 2 cm fiber. (a) spectral evolution. (b) temporal evolution. [2]	28
2.3.1 Diagram of transitions between vibrational energy levels corresponding to the processes of Rayleigh and Raman scattering.	34
2.3.2 Energy diagram of two-color CARS process, all the input pulses are narrow-band.	38
2.3.3 Energy diagram of non-resonant processes.	39
2.3.4 Phase matching condition.	40
2.3.5 (a) Purely resonant contribution; (b) Purely non-resonant contribution; (c) Dispersive mixing term $2Re\{\chi_R^{(3)}\}\chi_{NR}^{(3)}$; (d) Typical line shape of the CARS intensity for a single resonance.	41
2.3.6 Generation of FT-Cars signal from one molecular vibrational mode.	43
3.2.1 Experimental Setup	47
3.2.2 Pulse generation stage.	48
3.2.3 Pulse amplification stage.	48
3.2.4 Spectral broadening and pulse compression stage.	49
3.2.5 Commercial Autocorrelator, FR-103XL FemtoChrome	50
3.2.6 Internal insight of Commercial Autocorrelator, FR-103XL FemtoChrome	50
3.3.1 Spectral Power Density of The low power Yb laser	51
3.3.2 SH Intensity measured at the output of The low power Yb laser	52
3.3.3 High-power pump diode at 976 nm with heat sink	53
3.3.4 Output power of the Yb-fiber amplifier as a function of the pump diode current.	54
3.3.7 Photonic Crystal Fiber structure	54
3.3.5 Autocorrelation trace of the pulses at the output of the Yb amplifier as measured after the grating compressor	55
3.3.6 Spectrum of pulses at the output of the Yb amplifier as measured after the grating compressor	55
3.4.1 Spectrum of the supercontinuum at the output of the PCF fiber	56

3.4.2 Autocorrelation trace of the pulses at the output of the SF10 prism pair	57
4.1.1 Schematic of the rapid-scan FT-CARS system.	59
4.1.2 Photo of the implemented Michelson interferometer.	60
4.1.3 Photo of the implemented transmission stage.	61
4.1.4 Interferogram with detail of the time window used for Fourier transform.	62
4.1.5 Scan-arm in 4-f configuration.	63
4.1.6 Schematic of the rapid-scan FT-CARS system in back-reflection configuration.	64
4.1.7 Back-reflection segment.	65
4.1.8 Photo of the implemented set up.	66
4.1.9 Non resonant galvo-mirror [3].	67
4.1.10 Resonant galvo-mirror [4].	67
4.1.11 Driver board of GVS001 Thorlabs [3].	68
4.1.12 Command input connector pin identification [3].	69
4.1.13 Siglent SDG 5162 wave generator.	69
4.1.14 Driver board of CRS4Hz Cambridge Technology.	70
4.1.15 Pin identification of connector J2 [4].	70
4.2.1 CARS spectrum generated by an acetonitrile sample.	71
4.2.2 Raman spectra of acetonitrile as observed by Fourier transform of one interferogram (no averaging, black line), and 10 (red line), 100 (blue line), 1000 (pink line) averaged interferograms.	72
4.2.3 Raman spectrum of dimethyl methylphosphonate (DMMP) (CAS number 756-79-6) [5].	73
4.2.4 Raman spectrum of tris(2-ethylhexyl) phosphate (TEHP) (CAS number 78-42-2) [5].	73
4.2.5 Raman spectrum of Thiodiglycol (TDG) (CAS number 111-48-8) [5].	74

4.2.6 CARS spectra of DMMP as measured with a single acquisition (black line) and by the average of 10 (red line), 100 (blue line), 1000 (green line) spectra.	75
4.2.7 CARS spectrum of DMMP as measured by the average of 1000 spectra (red line), and spontaneous Raman spectrum (blue line) as measured with a commercial Nicolet Raman 950 [5].	76
4.2.8 CARS spectra of TDG as measured with a single acquisition (black line) and by the average of 10 (red line), 100 (blue line), 1000 (green line) spectra.	77
4.2.9 CARS spectrum of a 50:50 solution by volume of TDG and acetonitrile.	78
4.2.10 CARS spectrum of TDG as measured by the average of 1000 spectra (red line), and spontaneous Raman spectrum (blue line) as measured with a commercial Nicolet Raman 950 [5].	79
4.2.11 CARS spectra of TEHP as measured with a single acquisition (black line) and by the average of 10 (red line), 100 (blue line), 1000 (green line) spectra.	80
4.2.12 CARS spectrum of TEHP as measured by the average of 1000 spectra (red line), and spontaneous Raman spectrum (blue line) as measured with a commercial Nicolet Raman 950 [5].	81
4.2.13 Stainless-steel substrate.	83
4.2.14 Glass substrate.	83
4.2.15 Epi-CARS of DMMP deposited on stainless steel for 0.01 s (green line), 0.1 s (blue line), 1 s (red line) and 10 s (black line) integration times.	84
4.2.16 Epi-CARS spectrum of DMMP as measured with acquisition time 10 s (red line), and spontaneous Raman spectrum (black line) [5].	85
4.2.17 Epi-CARS of TDG deposited on stainless steel for 0.01 s (green line), 0.1 s (blue line), 1 s (red line) and 10 s (black line) integration times.	86
4.2.18 Epi-CARS spectrum of TDG as measured with acquisition time 10 s (red line), and spontaneous Raman spectrum (black line) [5].	87
4.2.19 Epi-CARS of TEHP deposited on stainless steel for 0.01 s (green line), 0.1 s (blue line), 1 s (red line) and 10 s (black line) integration times.	88
4.2.20 Epi-CARS spectrum of TEHP as measured with acquisition time 10 s (red line), and spontaneous Raman spectrum (black line) [5].	89

4.2.2	Epi-CARS of DMMP deposited on glass for 0.01 s (green line), 0.1 s (blue line), 1 s (red line) and 10 s (black line) integration times.	90
4.2.2	Epi-CARS spectrum of DMMP as measured with acquisition time 10 s (red line), and spontaneous Raman spectrum (black line) [5].	91
4.2.2	CARS of acetonitrile for a single acquisition (green line), 10 (blue line), 100 (red line) and 1000 (black line) averages, at 4kHz. . . .	93
4.2.2	CARS of DMMP for 125 μ s (green line), 1.25 ms (blue line), 12.5 ms (red line) and 125 ms (black line) integration times.	94
4.2.2	CARS spectrum of DMMP as measured with acquisition time 125 ms (red line), and spontaneous Raman spectrum (black line) [5].	95
4.3.1	(a) Ramp signal at 100 Hz used to pilot the galvo-mirror; (b) Interferogram of the He-Ne.	96
4.3.2	Distorted interferogram at the edges of the ramp.	97
4.3.3	Comparison between acetonitrile measured with 1000 averages, using asynchronous (red line) and synchronous (black line) sampling, using a ramp signal at 100 Hz.	98
4.3.4	(a) Sine signal at 100 Hz used to pilot the galvo-mirror; (b) Interferogram of the He-Ne.	99
4.3.5	Comparison between acetonitrile measured with 1000 averages, using asynchronous (red line) and synchronous (black line) sampling, using a sine signal at 100 Hz.	100
4.3.6	(a) Sine signal at 4 kHz used to pilot the galvo-mirror; (b) Interferogram of the He-Ne.	101
4.3.7	Comparison between acetonitrile measured with 1000 averages, using asynchronous (red line) and synchronous (black line) sampling, using a sine signal at 4 kHz.	101

List of Tables

4.1	SNR of DMMP strongest Raman line as a function of spectral averaging.	75
4.2	SNR of TDG strongest Raman line as a function of spectral averaging.	77
4.3	SNR of TEHP strongest Raman line as a function of spectral averaging.	80
4.4	SNR of DMMP strongest Raman line as a function of spectral averaging, with DMMP deposited onto a stainless steel substrate.	84
4.5	SNR of TDG strongest Raman line as a function of spectral averaging, with TDG deposited onto a stainless steel substrate.	86
4.6	SNR of TEHP strongest Raman line as a function of spectral averaging, with TEHP deposited onto a stainless steel substrate.	88
4.7	SNR of DMMP strongest Raman line as a function of spectral averaging, with DMMP deposited onto a glass substrate.	90
4.8	SNR of DMMP strongest Raman line as a function of spectral averaging at 4 kHz.	94

Chapter 1

Introduction

In recent years, the risk of terrorist attacks based on the use of chemicals warfare agents (CWAs) has increased, thus requiring new systems for prevention and detection of these agents: the main necessity is to develop fast, precise and efficient techniques. In this thesis a set up based on Raman spectroscopy is exploited, in particular, the coherent anti-stokes Raman spectroscopy (CARS) technique is implemented in the Fourier transform version (FT-CARS). To implement this technique, ultra-short pulses are required, thus we first needed to develop a pulse generation stage too.

In order to obtain ultra-short pulses a fiber-based configuration has been chosen. We started from a low power mode-locking Ytterbium laser and the generated pulses were injected in a Ytterbium fiber amplifier. The choice of Ytterbium was led by the fact that light amplification in such a material involves two energy levels manifold separated by an extremely small energy gap resulting in extremely low quantum defects. High power efficiency is thus achievable and detrimental effects such as thermal effects, quenching and excited state absorption are significantly reduced [6]. In order to obtain the required bandwidth, the pulses undergo a spectral broadening stage consisting in the propagation through a photonic crystal fiber (PCF). Although such a short-pulse can easily get stretched by transmitting through a medium, we carefully chose the optical components and keep the amount of dispersion of the system as low as possible so that we achieve the large spectral bandwidth by compensating the dispersion with chirped mirrors and a prism pair. This simple dispersion management drastically reduces the complexity of the system, otherwise one has to use an additional device such as a spatial light modulator in order to compensate higher-order dispersion.

The choice of Raman scattering spectroscopy is driven by the fact that it provides the intrinsic molecular vibrational information about the sample in a label-free and non-invasive manner, thus it is widely used for investigating materials, chemicals, and biological specimens. However, since the spontaneous Raman scattering process typically has a low scattering cross-section, measurements demand long data acquisition times, thus representing a limiting factor

for many applications. On the other hand, spectroscopy based on coherent Raman scattering (CRS) including CARS and stimulated Raman scattering (SRS) has significantly improved the data acquisition time by virtue of the enhanced nonlinear signal. In particular, CRS spectroscopy has been employed in different applications such as: cancer detection, drug delivery, endoscopy, single molecule analysis and lipid metabolism. To improve the measurement speed, several broadband CRS spectroscopies have been developed with a multi-channel detector, frequency-swept lasers, dual frequency combs or a Michelson interferometer.

FT-CARS spectroscopy is a version of time-domain coherent Raman scattering spectroscopy whose principle is analogous to impulsive stimulated Raman scattering. In FT-CARS, a train of dual pulses with a time delay with respect to each other is used to excite and probe the target molecular vibrations. The first pulse excites the vibrations, whose periods are longer than the pulse width, which are then probed by the second pulse. The time delay is scanned by every pulse pair to pulse pair, which generates anti-Stokes or Stokes pulses alternately. When the probe pulse probes the molecular vibration out-of-phase, it gains energy from the molecules (anti-Stokes shift). The resulting filtered anti-Stokes signal is encoded in the time-domain interferogram, which is detected by a photodetector. The CARS spectrum can be obtained by taking the Fourier-transform of the interferogram.

In this thesis, an FT-CARS technique combined with femtoseconds pulses is presented, that enabled us to measure a large spectral bandwidth by virtue of the excitation mechanism of impulsive stimulated Raman scattering. Thus we were able to perform CARS measurements acquired at a range of different integration times, which let us elucidate the shortest time to acquire a CARS spectrum with acceptable signal-to-noise ratio for different chemical/surface combinations.

Before getting into the heart of the thesis, **Chapter 2: Theoretical Principles** provides the background theory about the most important aspects of the project. First of all, the basic features of mode-locked oscillators are presented in Section 2.1, then Section 2.2 focuses on fiber non-linear optics, in particular fiber amplifiers are briefly presented and the principles of SPM broadening in optical fibers are discussed. Finally, Section 2.3 first presents the basic principles of spontaneous Raman scattering, then coherent Raman scattering is introduced and the FT-CARS technique is presented.

In **Chapter 3: Laser Source**, the experimental set-up developed and the properties of the obtained laser source are presented. In particular in Sections 3.2.1 and 3.3, the experimental setup is presented and discussed in its main components. In Section 3.4 the properties of the obtained pulse are shown.

Chapter 4: FT-CARS enabled by Michelson Interferometer is divided in 3 main Sections. In the first one, Section 4.1 the experimental set-up, in its different iterations, is presented. Next, in Section 4.2, the results we achieved in the detection of CWAs simulants are discussed. Then, Section 4.3 describes in deeper details the sampling process implemented.

Chapter 2

Theoretical Principles

In the following chapter the basic physical principles of the project will be discussed. In Section 2.1, the concept of mode-locking laser will be discussed; in Section 2.2 the principles of fiber amplifiers and spectral broadening due to fiber non-linearities are presented; finally in Section 2.3 Raman scattering spectroscopy is discussed in its different implementations.

2.1 Mode-Locked Oscillators

The basic principles of mode-locking will be discussed as in the literature [7]. Consider a laser oscillating on a large number of longitudinal modes. Usually, the phases of these modes will have random values and for CW oscillation, the beam intensity will show a random time behavior. Despite this randomness, since these pulses arise from the sum of N frequency components evenly spaced, the pulse waveform has the following general properties, characteristic of a Fourier series:

1. The waveform is periodic with period $\tau_p = \frac{1}{\Delta\nu}$ where $\Delta\nu$ is the frequency difference between two consecutive longitudinal modes.
2. Each light pulse has a duration $\Delta\tau_p$ roughly equal to $\frac{1}{\Delta\nu_L}$, where $\Delta\nu_L = N\Delta\nu$ is the total oscillating bandwidth.

Notice that, for lasers with large gain bandwidths, such as solid-state, dye or semiconductor lasers, $\Delta\nu_L$ may be comparable to this gain bandwidth, so it is possible to obtain short noise pulses with duration of picoseconds or less.

Assume now that the oscillating modes, still having comparable amplitudes, are somehow oscillating with some definite relation between their phases. Such a laser is referred to as mode locked, and the process by which the modes are made to adopt a definite phase relation is referred to as mode locking.

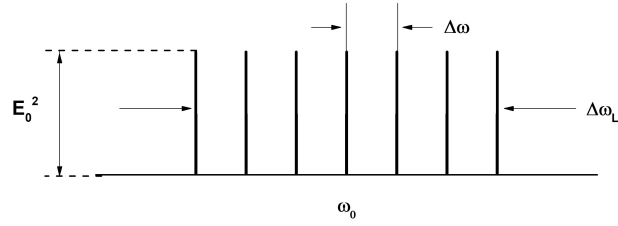


Figure 2.1.1: Mode amplitudes vs frequency for a mode-locked laser.

2.1.1 Frequency Domain Description

Consider the case of $2n + 1$ longitudinal modes, oscillating with the same amplitude for simplicity. We assume the phases ϕ_k of the modes in the output beam to be described by the so called phase-locking condition:

$$\phi_k - \phi_{k-1} = \phi \quad (2.1.1)$$

where ϕ is constant.

The electric field $E(t)$, of the e.m. wave can be written as:

$$E(t) = \sum_{k=-n}^n E_0 \exp\{i[(\omega_0 + k\Delta\omega)t + k\phi]\} \quad (2.1.2)$$

where ω_0 is the frequency of the central mode, $\Delta\omega$ is the frequency difference between two consecutive modes and where we assumed the value of the phase of the central mode to be zero for simplicity.

One can write Eq. 2.1.2 as:

$$E(t) = A(t) \exp(i\omega_0 t) \quad (2.1.3)$$

where:

$$A(t) = \sum_{k=-n}^n E_0 \exp[ik(\Delta\omega t + \phi)] \quad (2.1.4)$$

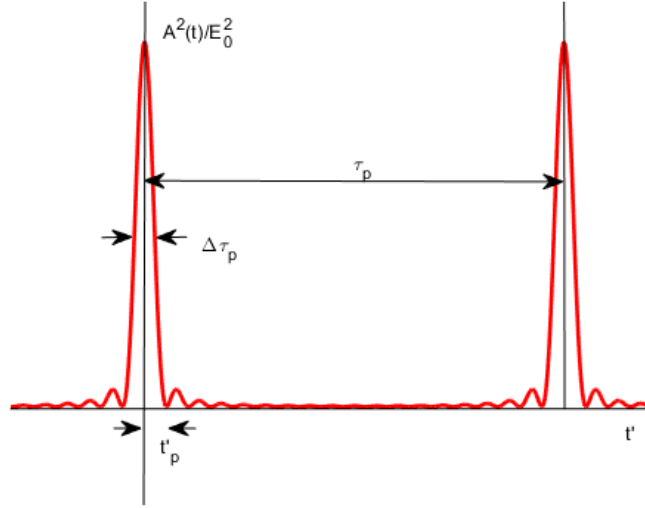


Figure 2.1.2: Behavior of the squared amplitude of the electric field for $n = 9$ modes with locked phase and equal amplitude E_0 .

Eq. 2.1.3 shows how the electric field can be represented as a sinusoidal carrier wave at ω_0 , with a time dependent amplitude $A(t)$.

Changing the time reference such that $\Delta\omega t' = \Delta\omega t + \phi$, equation 2.1.4 becomes:

$$A(t) = \sum_{k=-n}^n E_0 \exp(ik\Delta\omega t') \quad (2.1.5)$$

The sum is a geometric progression, so one can obtain:

$$A(t') = E_0 \frac{\sin[(2n+1)\Delta\omega t'/2]}{\sin[\Delta\omega t'/2]} \quad (2.1.6)$$

The behavior of the quantity $A^2(t')/E_0^2$, with $A^2(t')$ proportional to the intensity, versus time t' is showed in Fig. 2.1.2.

One can notice that, as a result of the phase-locking condition Eq. 2.1.1, the modes interfere producing a train of evenly spaced pulses. It is easy to compute the time separation between the light pulses:

$$\tau_p = 2\pi/\Delta\omega = 1/\Delta\nu \quad (2.1.7)$$

One can see that the first pulse vanishes after a time t'_p ; since the width $\Delta\tau_p$ is approximately equal to t'_p , one can easily obtain:

$$\Delta\tau_p = 2\pi/[(2n+1)\Delta\omega] = 1/\Delta\nu_L \quad (2.1.8)$$

where $\Delta\nu_L$ is the total oscillating bandwidth.

So far it has been showed how, under the mode-locking condition, the output beam consists of a train of mode-locked pulses, with duration $\Delta\tau_p$, about equal to the inverse of the total oscillating bandwidth $\Delta\nu_L$. Since $\Delta\nu_L$ can be of the order of the gain line $\Delta\nu_0$, very short pulses can be obtained from mode-locking solid state or semiconductor lasers. Note also that the peak power of the pulse is proportional to $(2n+1)^2 E_0^2$, while for random phases the average power is proportional to $(2n+1)E_0^2$. We can thus see that in the mode-locked case the peak power is larger of a $(2n+1)$ factor, which can be rather high. So, mode-locking is not only useful for producing very short pulses but also for producing high peak powers.

All these results are however obtained in the rather unrealistic case of an equal amplitude mode-spectrum. In general the envelope has a bell-shaped form and as an example we can consider an envelope with a Gaussian distribution. In this case, skipping calculations, we have:

$$\Delta\tau_p = \frac{2 \ln 2}{\pi \Delta\nu_L} = 0.441/\Delta\nu_L \quad (2.1.9)$$

So, in general, when the mode-locking condition holds, $\Delta\tau_p$ is related to $\Delta\nu_L$ by the relation $\Delta\tau_p = \beta/\Delta\nu_L$ with β a numerical factor depending on the shape of the spectral intensity distribution. A pulse of this sort is said to be transform limited.

Under different locking conditions. the output pulse may be far from being transform limited. Consider for example the following condition:

$$\phi_k = k\phi_1 + k^2\phi_2 \quad (2.1.10)$$

with ϕ_1 and ϕ_2 two constants.

In this case, assuming again a Gaussian amplitude distribution, one can notice the following:

1. we still have a Gaussian function with width:

$$\Delta\tau_p = (2 \ln 2/\alpha)^{1/2} \quad (2.1.11)$$

2. the presence of a phase term $k^2\phi_2$ results in $E(t)$ having a phase term βt^2 , quadratic in time. So the instantaneous carrier frequency $\omega(t) = d(\omega_0 t + \beta t^2)/dt = \omega_0 + 2\beta t$ has a frequency chirp.
3. depending of the value of ϕ_2 , the product $\Delta\tau_p\Delta\nu_L$ can be much larger than 0.441, in fact:

$$\Delta\nu_L = \frac{0.441}{\Delta\tau_p} \left[1 + \left(\frac{\beta\Delta\tau_p^2}{2 \ln 2} \right) \right]^{1/2} \quad (2.1.12)$$

The physical explanation for this result is that the spectral broadening now arises both from the modulation of $E(t)$ and from the frequency chirp term $2\beta t$ of $E(t)$.

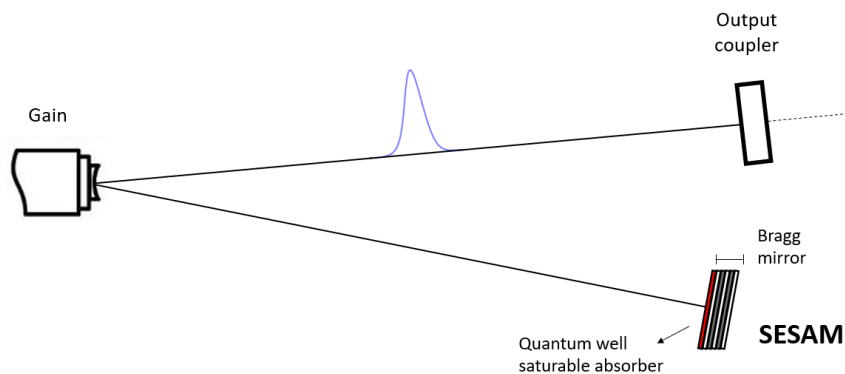


Figure 2.1.3: SESAM scheme in a cavity.

2.1.2 SESAM - Semiconductor Saturable Absorber Mirrors

The methods for obtaining mode-locking can be divided into two categories [7]:

1. Active-mode-locking, in which the mode-locking element is driven by an external source.
2. Passive-mode-locking, in which the element inducing mode-locking is not externally driven, but exploits some non linear optical effect.

In this thesis we will briefly consider the case of passive mode-locking, in particular on the use of semiconductor saturable absorber mirrors (SESAM) since it is the one used in our case.

A SESAM usually consists of a mirror structure with an incorporated saturable absorber, all made in semiconductor technology, as shown in Fig. 2.1.3. These devices allow for self-starting, stable, and reliable mode-locking of diode-pumped ultra-fast solid-state lasers [8].

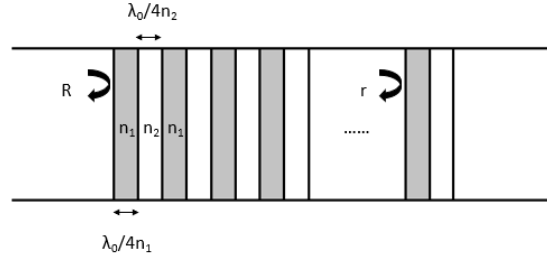


Figure 2.1.4: Quarter-wave Bragg Mirror.

Bragg Mirrors

Typically, the mirror structure of a SESAM is given by a Bragg mirror: it consists of an alternating sequence of layers of two different optical materials. The most frequently used design is that of a quarter-wave mirror, where each optical layer thickness corresponding to one quarter of the wavelength for which the mirror is designed [9], as shown in Fig. 2.1.4. The essential idea is that, at the Bragg wavelength, the reflections at each index discontinuity add up in phase, leading to a large reflectivity. Generally, more than 20 Bragg pairs are required for a mirror [10].

The reflectivity of a Bragg mirror depends on the difference between n_1 and n_2 and on the number of layer pairs. When the number of layer pairs is sufficiently high, the reflectivity is characterized by a broad spectral region of very high reflectivity around the Bragg wavelength [10]. This region is called stop-band and it represents the wavelength interval where the periodic photonic structure does not allow transmission.

The width of this band is roughly given by [10]:

$$\Delta\lambda_{stop} \approx \frac{2\lambda_B \Delta n}{\pi \bar{n}_g} \quad (2.1.13)$$

where $\Delta n = |n_1 - n_2|$ and \bar{n}_g is the spatial average of the group index.

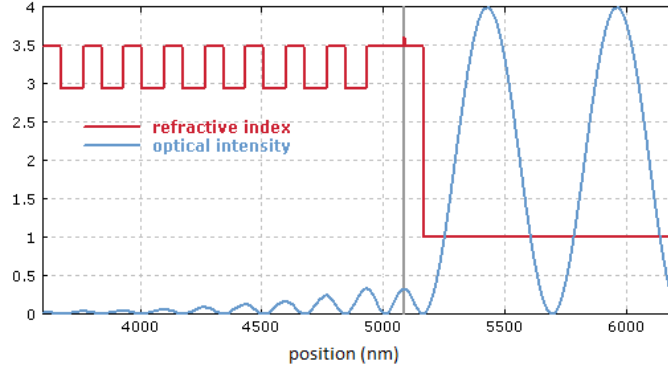


Figure 2.1.5: Refractive index profile and optical intensity distribution. [1]

Saturable Absorber

A saturable absorber is an optical component with a certain optical loss, which is reduced at high optical intensities. This can occur, for example, in a medium with absorbing dopant ions, when a strong optical intensity leads to depletion of the ground state of these ions [1]. Similar effects can occur in semiconductors, where excitation of electrons from the valence band into the conduction band reduces the absorption for photon energies just above the band gap energy.

Typically, a SESAM contains a semiconductor Bragg mirror and a single quantum well absorber layer near the surface. The penetration of the optical field into a SESAM can be calculated with the same matrix method applied to other types of dielectric mirrors. Of particular importance is the optical intensity in the region where the saturable material is placed. This influences the modulation depth and also the saturation fluence [1]. However, the design of the structure also influences the bandwidth and the chromatic dispersion.

The saturation energy of a laser gain medium is the pulse energy of an incident short signal pulse which leads to a reduction in the gain to $1/e$ ($\approx 37\%$) of its initial value. Similarly, the saturation energy of a saturable absorber is defined. The saturation fluence is the saturation energy per unit area.

Typically, an absorber layer is placed in an anti-node of the electric field as shown in Fig. 2.1.5 [1]. That leads to maximum saturable absorption and the smallest possible saturation fluence. If multiple absorber layers are required for a high modulation depth, they may be placed in separate anti-nodes, or possibly several of them near one anti-node.

The derivation of the absorption of the saturable absorber will be presented in the following [11].

Consider the saturable absorber as a two level system. The electrons in the valence band of the semiconductor absorber material are in their ground state and can be excited into the conduction band when photons with energy $E = h\nu$ are absorbed. Calling the number of states in the valence band N_V and in the conduction band N_C , during the illumination of the absorber the rate of transitions between the two states can be described as:

$$\frac{\partial N_C}{\partial t} = -\frac{\partial N_V}{\partial t} = B_{12}\rho(\nu)(N_V - N_C) - \frac{N_C}{\tau} \quad (2.1.14)$$

where $B_{12} = B_{21}$ is the B Einstein coefficient, $\rho(\nu)$ is the density of incident photons and τ is the relaxation time of excited electrons in the conduction band.

The excited electrons in the conduction band relax either by spontaneous photon emission or by non-radiative energy loss with a mean relaxation time constant τ . The sum of states in the valence and conduction band gives the total number of electrons N_T which take place on the absorption process: $N_T = N_C + N_V$. Without illumination of the absorber all electrons are in the ground state $N_V = N_T$. In case of very high density of incident photons the maximum value for the excited states $N_C = N_V = N_T/2$ is approached and the absorber is transparent. The absorption A of the saturable absorber is proportional to the number of electrons N_V in the ground state.

If we consider that the incident photon density is proportional to the time dependent optical beam intensity $I(t)$ then we can rewrite the rate equation for the number of states into a rate equation for the absorption $A(t)$ as:

$$\frac{\partial A(t)}{\partial t} = \frac{A_0 - A(t)}{\tau} - \frac{A(t)I(t)}{F_{sat}} \quad (2.1.15)$$

where A_0 is the non-saturated absorption, $I(t)$ is the optical intensity and $F_{sat} = I(t)/B_{12}\rho(\nu)$ is the saturation fluence. For laser mode-locking the relaxation time τ of the excited carriers shall be somewhat longer than the pulse duration, thus we are in the approximation of long relaxation time $\tau \gg t_p$, where t_p is the pulse duration. In this case the relaxation term in the rate equation of the absorption can be neglected, so we are left with:

$$\frac{\partial A(t)}{\partial t} = -\frac{A(t)I(t)}{F_{sat}} \text{ with solution } A(t) = A_0 \exp \left[-\int_{-\infty}^t \frac{I(t)}{F_{sat}} dt \right] \quad (2.1.16)$$

For a Gaussian pulse, the integration delivers:

$$A(t) = A_0 \exp \left\{ -S \left[1 + \operatorname{erf} \left(\frac{t}{t_p} \right) \right] \right\} \quad (2.1.17)$$

where $S = F_0/F_{sat}$ is called saturation parameter and F_0 is the fluence of the pulse. A representation of the time dependence of the absorption is shown in Fig. 2.1.6.

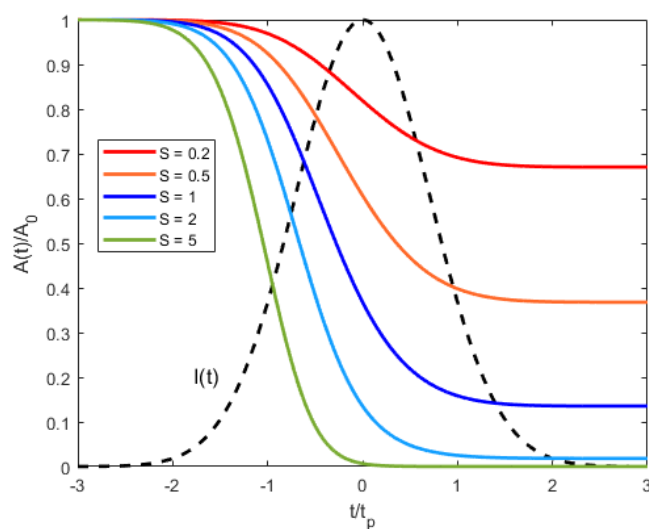


Figure 2.1.6: Time dependent absorption for different saturation parameters.

2.1.3 Cavity Dispersion in Femtosecond Mode-Locked Lasers

When ultra-broad-band gain media are involved, cavity dispersion plays an important role in establishing the pulse duration achieved by ML [7].

Phase Velocity, Group Velocity and Group-Delay-Dispersion

Consider for simplicity a plane, linearly polarized, monochromatic e.m. wave at frequency ω , which propagates along direction z of a transparent medium. The electric field $E(z, t)$ can be written as $E = A_0 \exp i(\omega t - \beta z)$. The propagation constant β is a function of ω and the relation $\beta = \beta(\omega)$ is referred to as dispersion relation of the medium. The total phase of the wave is $\phi_t = \omega t - \beta z$, so the velocity of the phase front is obtained by imposing $d\phi_t = \omega dt - \beta dz = 0$. So the phase velocity is given by:

$$v_{ph} = \frac{dz}{dt} = \frac{\omega}{\beta} \quad (2.1.18)$$

Consider now a light pulse traveling in a medium with ω_L and $\Delta\omega_L$, respectively the central frequency and the width of the corresponding spectrum. Assuming $\Delta\omega_L$ to be not very large, we can approximate the dispersion relation linearly: $\beta = \beta_L + (d\beta/d\omega)_{\omega=\omega_L}(\omega - \omega_L)$, where $\beta_L = \beta(\omega_L)$. In this case, one can show that the electric field can be expressed as:

$$E(t, z) = A[t - (z/v_g)] \exp[i(\omega_L t - \beta_L z)] \quad (2.1.19)$$

where A is the amplitude of the pulse and the second term is the carrier wave.

The quantity v_g is instead given by:

$$v_g = \left(\frac{d\omega}{d\beta} \right)_{\beta=\beta_L} \quad (2.1.20)$$

One can see the pulse amplitude is a function of $t - (z/v_g)$ meaning that the pulse propagates without changing its shape at speed v_g , referred to as group velocity. Note that, for a general dispersion relation, as shown in Fig. 2.1.7, the phase velocity of the carrier wave is different from the group velocity.

The pulse, when traversing a length l of the medium, will accumulate a time delay:

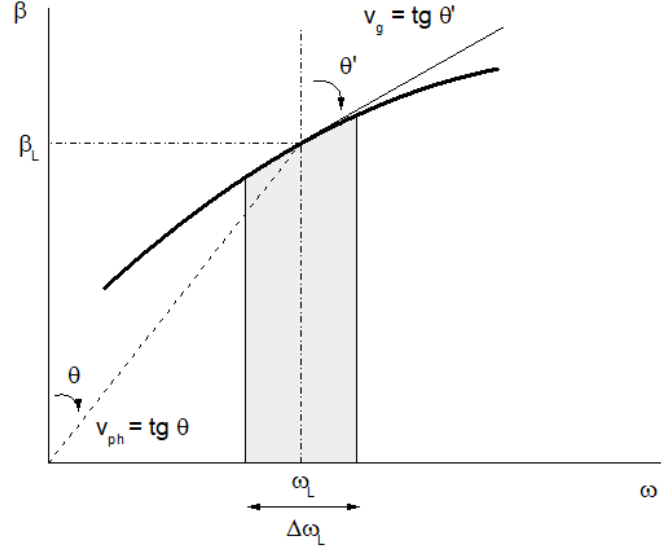


Figure 2.1.7: Phase velocity and group velocity in a dispersive medium.

$$\tau_g = \frac{l}{v_g} = l \left(\frac{d\beta}{d\omega} \right)_{\omega_L} = \phi'(\omega_L) \quad (2.1.21)$$

where we defined ϕ as a phase term dependent on ω :

$$\phi(\omega - \omega_L) = \beta(\omega - \omega_L)l \quad (2.1.22)$$

and $\phi'(\omega_L) = [d\phi(\omega - \omega_L)/d\omega]_{\omega_L}$. The quantity τ_g is referred to as group delay of the medium at ω_L .

Consider now two pulses traveling in a medium, with central frequencies ω_1 and ω_2 , and with bandwidths $\Delta\omega_1$ and $\Delta\omega_2$ respectively, where $\omega_2 > \omega_1$, as shown in Fig. 2.1.8.

The slope of the dispersion relation is different at the two frequencies, so the two pulses will travel at different group velocities v_{g1} and v_{g2} . Therefore, after traversing the length l of the medium, the two pulse will be separated in time by:

$$\Delta\tau_g = \phi'(\omega_2) - \phi'(\omega_1) \approx \phi''(\omega_1) (\omega_2 - \omega_1) \quad (2.1.23)$$

with $\phi''(\omega_1) = [d^2\phi/d\omega^2]_{\omega_1}$.

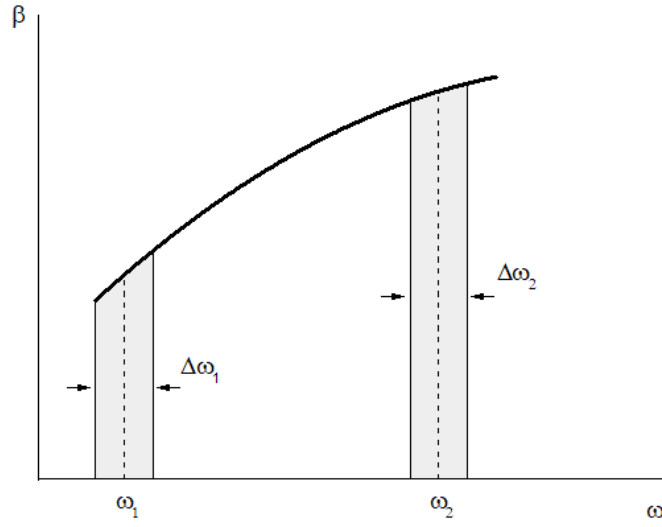


Figure 2.1.8: Time delay dispersion for two pulses.

Consider next the case of a light pulse with a very large bandwidth $\Delta\omega_L$. In this case, it is no longer a good approximation to describe the dispersion linearly, in fact, different spectral regions of the pulse will travel with different group velocities and thus the pulse will broaden as it propagates. Assuming a dispersion relation approximated by a parabolic law in $\Delta\omega_L$, the broadening of the pulse is approximately given by the difference in group delay between the fastest and slowest spectral components. According to Eq. 2.1.23:

$$\Delta\tau_d \approx |\phi''(\omega_L)|\Delta\omega_L \quad (2.1.24)$$

The quantity $\phi''(\omega_L)$ is referred to as group delay dispersion (GDD) of the medium, at ω_L , and represents the pulse broadening per unit bandwidth of the pulse.

The quantity GVD is expressed by [7]:

$$\text{GVD} = (d^2\beta/d^2\omega)_{\omega_L} = [d(1/v_g)/d\omega]_{\omega_L} \quad (2.1.25)$$

It is referred to as group velocity dispersion and represents the pulse broadening per unit length of the medium and per unit bandwidth of the pulse.

Limitation on Pulse Duration

When a dispersive medium is present in the cavity, an approximated value of the steady state pulse duration is obtained from the condition that the relative time shortening $(\delta\tau_p/\tau_p)_s$, due to the net gain time window, must equal the pulse broadening due to both the gain medium, $(\delta\tau_p/\tau_p)_g$, and the dispersive medium, $(\delta\tau_p/\tau_p)_d$. One can derive [7]:

$$\left(\frac{\delta\tau_p}{\tau_p}\right)_s = 0.14 \frac{g_0}{\Delta\tau_p^2 \Delta\nu_0^2} + 3.84 \frac{\phi''^2}{\Delta\tau_p^4} \quad (2.1.26)$$

The two term are inversely proportional to $\Delta\tau_p^2$ and $\Delta\tau_p^4$, therefore the importance of GDD in establishing the pulse duration becomes more important as $\Delta\tau_p$ decreases.

In order to obtain the shortest possible pulse, second order dispersion GDD should be compensated, together with higher order dispersion terms. The now classical solution to providing negative and controllable second order GDD in a laser cavity utilizes a four prisms sequence.

2.2 Fiber Amplifiers and SPM-enabled Spectral Broadening in Optical Fibers

2.2.1 Fiber Amplifiers

Among many ultra-fast laser systems, ultra-fast Yb-fiber lasers have attracted intensive research efforts because of their superior power scalability, small footprint, excellent beam quality, and potential maintenance-free operation [2]. In this section the basics about optical fibers, fiber amplifiers, and nonlinear fiber optics will be presented.

Passive Fiber

Optical fibers are the fundamental components of fiber optics. They are usually made of some kind of glass; the most commonly used glass material for fibers is fused silica and optical fibers with a length of hundreds of kilometers can be obtained this way. Most optical fibers used in laser technology have a core with a refractive index higher than that of the surrounding medium, known as cladding. For the simple case of step-index optical fibers, the refractive indexes are constant for both the core and the cladding. Light launched into the fiber is guided by the core: the light propagates mainly in the core region, though the intensity distribution may extend beyond the core. Due to the guidance and the low propagation losses, the optical power can be maintained in the fiber for long propagation distances [2].

The design of a step-index fiber can be characterized with only three parameters: the core radius and the refractive indexes of the core and the cladding. Single mode fibers (SMFs) for guiding light at about $1.030 \mu m$ (the Yb-fiber laser wavelength) have a nominal core diameter of a few microns. The core-cladding refractive index contrast determines the fiber's numerical aperture(NA), which is defined as [2]:

$$NA = \frac{1}{n_0} \sqrt{n_{core}^2 - n_{cladding}^2} \quad (2.2.1)$$

where n_0 is the refractive index of the surrounding medium. The numerical aperture NA corresponds to the maximum acceptable angle of an incident beam with respect to the fiber axis and quantifies the strength of the fiber guidance.

Photonic crystal fiber (PCF) is a special type of optical fiber consisting of only one material (usually fused silica), containing small air holes with diameters well below $1 \mu m$. PCFs are fabricated by drawing fiber preforms that are prepared by stacking capillary tubes. By varying the arrangement of air holes, PCFs can be fabricated with customized properties and they have found many important applications such as fabrication of extremely nonlinear fiber devices,

high-energy and high-power laser beam delivery, and construction of high energy fiber amplifiers.

Active Fiber

If the core of an optical fiber is doped with rare-earth ions, such as ytterbium, erbium, thulium and so on, the fiber now becomes an active fiber and can work as a gain medium to construct ultra-fast fiber lasers. Single-pass of an Yb-doped fiber can provide small signal gain up to > 30 dB [2]. The schematics of a single-clad co-pumped fiber amplifier [6] is shown in Fig. 2.2.1. The pump and seed light are both confined in the single-mode core by total internal reflection, which results in excellent overlap between pump and seed.

An important aspect related to fiber amplifiers is the pump scheme. Based on the coupling technique, some common pump schemes are side-pumping, end-pumping and V-groove side-pumping [6]. Based on the direction of pump propagation with respect to seed/laser propagation, the pump schemes are classified as counter-pumping, co-pumping and bidirectional-pumping [6]. Optical isolators are used at the input and output ends to protect the seed and pump sources from backreflections.

Though single-clad fiber devices can achieve a very high gain, the maximum output power is limited due to the power available from single-mode pump sources. High power pump sources typically have a multi-mode output and hence cannot be used effectively to pump single-clad fibers. This is the reason why different fiber designs and architecture were investigated [12][13], such as the double-clad fibers [14].

In this design, the high power multi-mode pump laser is coupled into a large inner cladding (ic) with refractive index lower than the core but higher than the outer cladding (oc) ($n_{core} > n_{ic} > n_{oc}$), so that the pump light is guided in the inner cladding by total internal reflection. When the pump light overlaps with the core, it is absorbed by the active dopants in the core and

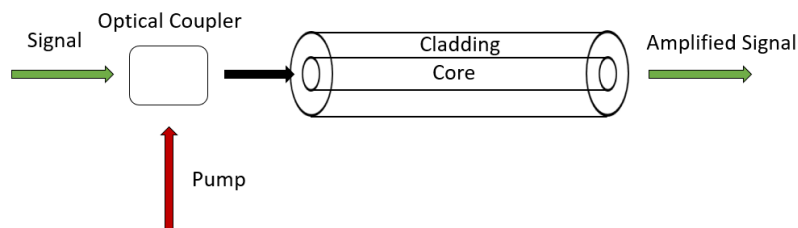


Figure 2.2.1: Single-clad, co-pumped fiber amplifier.



Figure 2.2.2: Cladding pumped, double-clad fiber amplifier.

thus enables amplification of the seed light [6]. Thus single mode beam quality can be maintained despite the use of high power multi-mode laser diodes as pump sources [6]. Such fiber systems are said to be "cladding pumped" and the schematic of such an amplifier is shown in Fig. 2.2.2.

The main advantage of a single-clad fiber, namely the excellent overlap of pump modes with the doped area, is lost in case of a double-clad fiber design. The simple centered circular core geometry shown in Fig. 2.2.2 is the easiest to fabricate and use, however, in such a structure, a large number of pump modes in the inner cladding have poor overlap with the core area, resulting in low efficiency of pump absorption in the core thus reducing the gain and power efficiency of the active fiber. Different inner cladding geometries have been proposed in order to increase the overlap of the pump modes with the core area [15][16].

Non-Linear Fiber Optics

When ultra-fast pulses propagate in the core of an optical fiber, with a nominal diameter of several microns, the intense peak power modifies the refractive index of the fiber material and leads to non-linear fiber optic effects [2]. This material response can be represented by an expansion of the material polarization [17]:

$$P = \chi^{(1)}E + \chi^{(2)}EE + \chi^{(3)}EEE + \dots \quad (2.2.2)$$

where $\chi^{(n)}$ is the n th order susceptibility of the material. Glasses are usually optically isotropic material and thus the second-order susceptibility vanishes. The different kinds of non-linearities considered here can be expressed in terms of the real and imaginary parts of the third-order nonlinear susceptibility appearing in Eq. 2.2.2. The real part is associated with the refractive index, the imaginary part corresponds to a time or phase delay in the material response, giving rise to either loss or gain. For instance, the nuclear contribution to stimulated Raman scattering or the electrostrictive stimulated Brillouin effect, both resulting in loss or gain, can be expressed in terms of the imaginary part of $\chi^{(3)}$, while four-wave mixing is associated with the real part of $\chi^{(3)}$ [18][19][20].

Given the small non-linear index of silica ($n_2 = 2.6 \cdot 10^{-26} \text{ cm}^2/W$), one would expect non-linear effects to be not prominent in optical fibers. However, two other fiber parameters, the mode field area (MFA) A_{eff} and the effective length L_{eff} , that strongly enhance the light-fiber non-linear interaction. These two parameters are given by [21]:

$$A_{eff} = \frac{\left(\int_{-\infty}^{+\infty} |A(x, y)|^2 dx dy\right)^2}{\int_{-\infty}^{+\infty} |A(x, y)|^4 dx dy} \quad (2.2.3)$$

$$L_{eff} = \frac{1}{\alpha} (1 - e^{-\alpha L}) \quad (2.2.4)$$

where $A(x, y)$ is the field distribution and α is the loss coefficient. MFA of conventional SMFs is about $80 \mu\text{m}$. L_{eff} is the effective propagation length taking into account loss. It is possible to compare the non-linearities in bulk media and silica fibers using the following ratio [21]:

$$\frac{I_f L_{eff}(fiber)}{I_b L_{eff}(bulk)} = \frac{\lambda}{\pi r_0^2 \alpha} \quad (2.2.5)$$

where I_f and I_b are the intensity (power per unit area) in the fiber and bulk, respectively. λ is the wavelength and r_0 the mode field radius of the fiber. As one can see from Eq. 2.2.5, a small mode field radius and low loss can greatly enhance the ratio and thus the optical non-linearities in fibers. For example, if we choose the wavelength to be $1 \mu\text{m}$ and a fiber with a typical loss of 0.2 dB/km , the nonlinear enhancement simply due to the small core can be of the order of 108.

GVD is another critical parameter in non-linear fiber optics causing mainly three effects [2]:

1. it determines the phase matching of parametric non-linear processes;
2. it causes group velocity mismatch and thus limits the effective interaction length for ultra-short pulses;
3. it stretches the propagating pulses, reduces the pulse peak power and therefore weakens the nonlinear interaction.

Fiber-optic non-linear effects can be a severe disadvantage for high energy pulse amplification and delivery in fibers because high peak intensities cause many fiber-optic non-linear effects that distort both the optical pulse and the optical spectrum. As a result, suppressing these non-linearities is crucial in

designing ultra-fast fiber laser systems. For example, high-energy ($>1 \mu J$) ultra-fast Yb-fiber amplifiers usually employ chirped-pulse amplification (CPA) to mitigate the detrimental nonlinear effects. In a typical Yb-fiber CPA system, weak pulses are temporally stretched before seeding into an Yb-fiber amplifier followed by a compressor to compress the stretched, amplified pulses to the transform-limited duration. However, fiber-optic non-linearities are extremely useful for many applications, such as wavelength conversion, spectral broadening and pulse compression, supercontinuum generation, etc.

2.2.2 SPM-enabled Spectral Broadening in Optical Fibers

Non-linear spectral broadening of ultra-short pulses in an optical fiber can be precisely modeled by the generalized non-linear Schrödinger equation (GNLSE) [22]:

$$\frac{\partial A}{\partial z} + \left(\sum_{n=2} \beta_n \frac{i^{n-1}}{n!} \frac{\partial^n}{\partial T^n} \right) A = i\gamma \left(1 + \frac{i}{\omega_0} \frac{\partial}{\partial T} \right) \left(A(z, T) \int_{-\infty}^{+\infty} R(t') |A(z, T - t')|^2 dt' \right) \quad (2.2.6)$$

where $A(z, t)$ is the envelope of the amplitude of the pulse and β_n represents the n -th order fiber dispersion. The non-linear parameter γ is defined as $\gamma = \omega_0 n_2 / (c A_{eff})$, where ω_0 is the pulse center frequency, n_2 the nonlinear-index coefficient of fused silica (with a typical value of $2.4 \cdot 10^{-20} m^2 W^{-1}$), c the light speed in vacuum and A_{eff} the mode-field area. A_{eff} is connected to the mode-field diameter by $A_{eff} = \pi(d/2)^2$. $R(t)$ describes both the instantaneous electronic and delayed molecular responses of fused silica, and is defined as:

$$R(t) = (1 - f_R)\delta(t) + f_R(\tau_1^2 + \tau_2^2) / (\tau_1 \tau_2) \exp(-t/\tau_2) \sin(t/\tau_1) \quad (2.2.7)$$

Taking into account dispersion, self-phase modulation (SPM), self-steepening (SS) and stimulated Raman scattering (SRS), Eq. 2.2.7 has been used to study non-linear propagation of ultra-short optical pulses inside an optical fiber [2]. Such a non-linear propagation can significantly broaden the optical spectrum and, under certain conditions, lead to supercontinuum generation.

Pure SPM

Consider first SPM only, neglecting dispersion, SS and SRS [2]. Eq. 2.2.6 is thus simplified:

$$\frac{\partial A}{\partial z} = i\gamma|A|^2A \quad (2.2.8)$$

The analytical solution of Eq. 2.2.8 is:

$$A(z, t) = A(0, t) \exp(i\gamma|A(0, t)|^2 z) \quad (2.2.9)$$

We can see that the phase term is dependent on the intensity profile of the pulse itself, thus, the electric field:

$$\begin{aligned} E(z, t) &= A(z, t) \exp[-i(\omega_0 t - k_0 z)] = \\ &= A(0, t) \exp[-i(\omega_0 t - k_0 z - \gamma|A(0, t)|^2 z)] = \\ &= A(0, t) \exp[-i\phi(z, t)] \end{aligned} \quad (2.2.10)$$

where ω_0 is the central frequency, k_0 is the wave-vector at that frequency and we defined the overall phase as $\phi(z, t)$.

Since the instantaneous frequency is the time partial derivative of the overall phase, one has:

$$\omega_i(z, t) = \frac{\partial \phi(z, t)}{\partial t} = \omega_0 - \gamma \frac{\partial |A(0, t)|^2}{\partial t} z \quad (2.2.11)$$

As one can see, new frequencies are generated by this process. In terms of wavelengths, the behavior of a 200-fs hyperbolic secant-squared pulse with central wavelength at $1.03 \mu m$ (Yb emission) and 50 nJ pulse energy, propagating inside an optical fiber with a mode-field diameter of $6 \mu m$, is shown in Fig. 2.2.3. From the picture one can notice that the spectrum of generated wavelengths dramatically increases with the fiber length z .

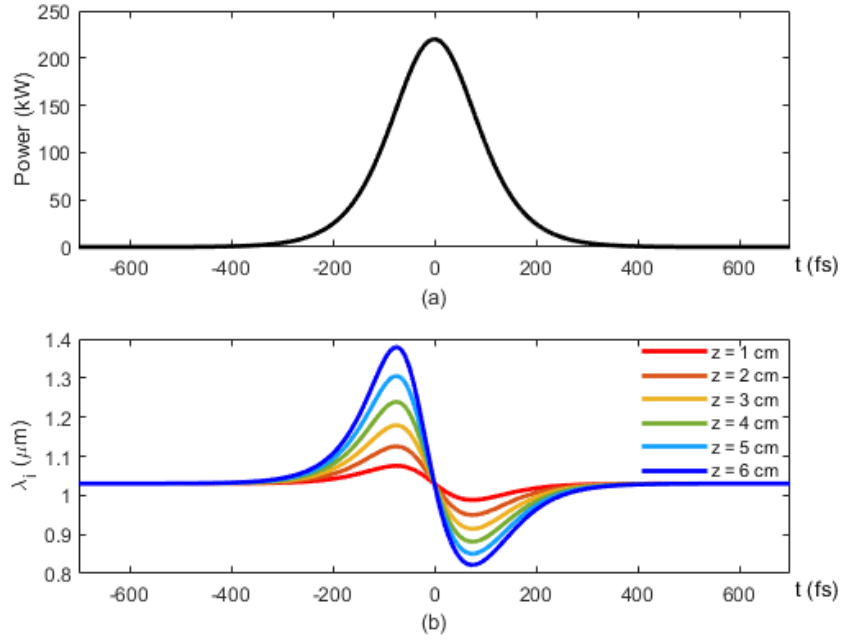


Figure 2.2.3: (a) Power profile of the input pulse; (b) Generated wavelengths as a function of time, for different propagation length z in the fiber.

It is also possible to observe this behavior in the frequency domain, as shown in Fig. 2.2.4 [2]. Fig. 2.2.4 not only shows that the spectrum is broadened along the fiber length, but also that the spectrum is composed of isolated spectral lobes, whose number is linearly proportional to the fiber length: this is a unique feature of an SPM broadened spectrum. Another peculiar feature of the spectrum is that the leftmost and rightmost spectral lobes are the strongest, having an energy $> 40\%$ of the overall energy.

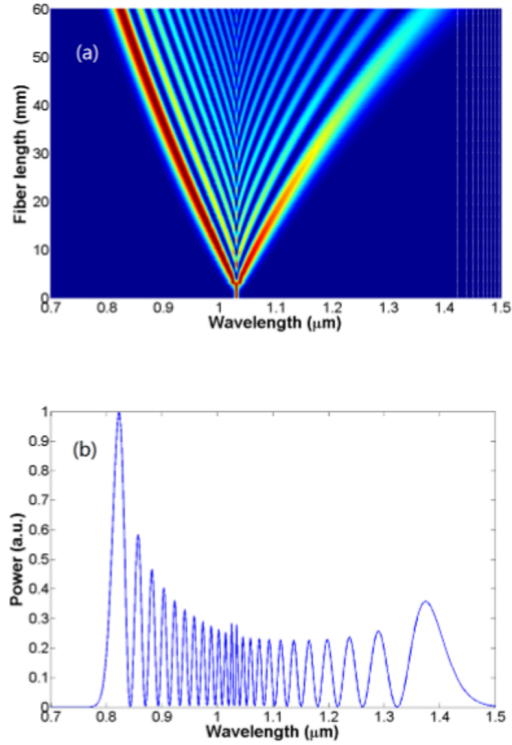


Figure 2.2.4: (a) Spectrum evolution versus fiber length; (b) Optical spectrum after propagating 6 cm in the fiber. [2]

Effect of SS and SRS

Even though the results shown previously are interesting and informative, they are unpractical since SPM only is considered. In fact, other non-linear effects takes place: SS and SRS. In Eq. 2.2.6, self-steepening is related to the term proportional to $\frac{1}{\omega_0}$ while the stimulated Raman scattering is related with the term $R(t)$ [23]. It is possible to solve Eq. 2.2.6 taking into account these terms [2] and considering a pulse as in the previous section, one obtains the behavior shown in Fig. 2.2.5 [2].

The spectrum broadened due to SPM and SS (blue curve in Fig. 2.2.5) is significantly blue shifted compared with the SPM-broadened spectrum (Fig. 2.2.4 (b)). When one considers also SRS, the spectrum (red curve in Fig. 2.2.5) becomes slightly narrower due to the small red shift of those spectral lobes on the left side; the corresponding pulse of this spectrum is shown as the inset. Maintaining almost its initial duration of 200 fs, the pulse exhibits a steeper trailing edge because of SS. It is the SS-induced steep trailing edge that extends the overall spectrum more into the shorter wavelength range.

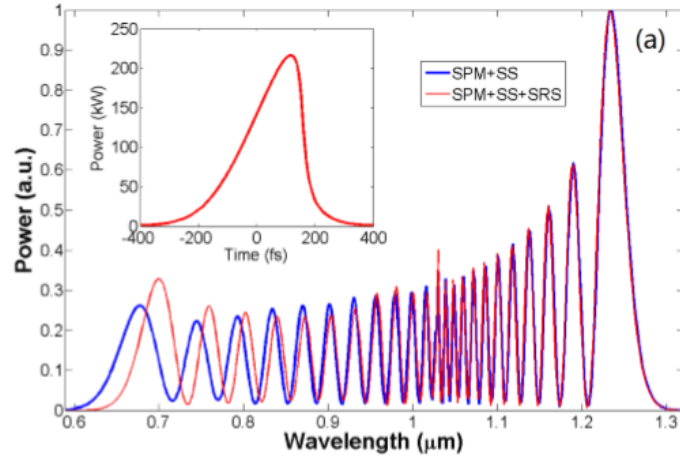


Figure 2.2.5: Optical spectra for simulations after 6 cm propagation, including SPM and SS (blue curve) or including SPM, SS, and SRS (red curve). Inset: optical pulse at the fiber output when the simulation includes SPM, SS, and SRS. [2]

So, summing up, one can observe that:

1. SS extends the broadened spectrum more towards shorter wavelengths;
2. For pure SPM, the energy of the leftmost and rightmost lobes is the same, while when SS and SRS are included, more energy is converted in the rightmost lobe;
3. The effect of SRS is minimal when compared with the effect of SS.

Effect of Dispersion

The results shown in Fig. 2.2.5 let us understand the physical processes related to spectral broadening. However, the fact that we are neglecting GVD makes the simulation inaccurate: GVD plays in fact an important role in non-linear fiber optics. Different nonlinear phenomena arise from the nonlinear pulse propagation inside a fiber with negative GVD: due to these complicated nonlinear interactions, the resulting broadened spectrum features fine structures with reduced phase coherence and generation of nearly transform-limited becomes challenging and suffers from poor efficiency [2]. In contrast, spectral broadening in a positive GVD fiber avoids involving above mentioned nonlinear phenomena and generates much smoother optical spectrum. Therefore the discussion will be restricted to positive GVD only.

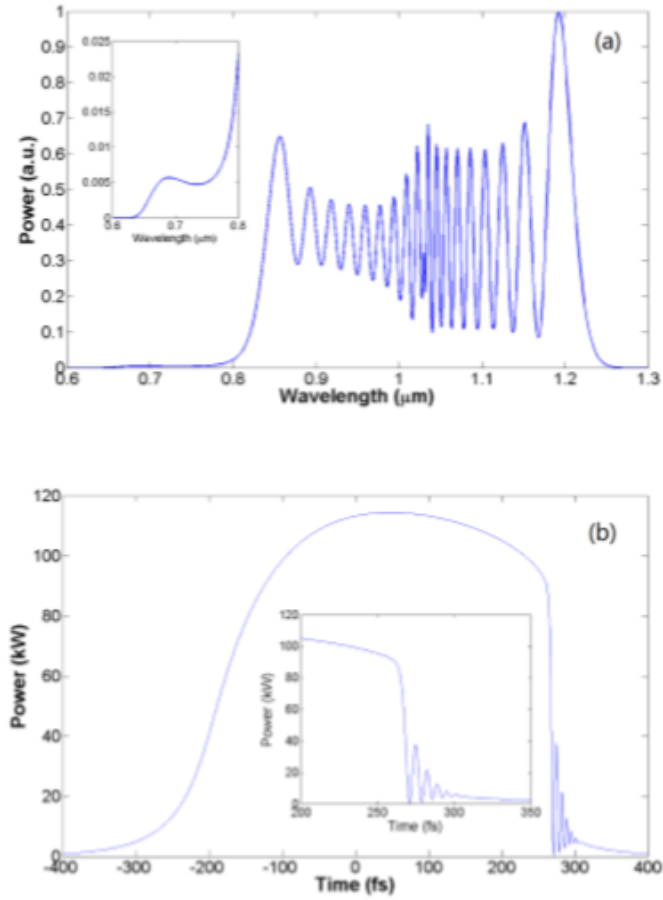


Figure 2.2.6: (a) Spectrum for simulations after 6 cm propagation including SPM, SS, SRS, and GVD ($5 \text{ fs}^2/\text{mm}$). Inset: close-up of the spectral range from 600-800 nm. (b) Corresponding pulse. Inset: close-up of the pulse envelope in the temporal range of 250-300 fs. [2]

The terms responsible for dispersion are the β_n terms in the sum of Eq. 2.2.6. It is possible thus possible to redo the simulation reported before accounting for dispersion too [2]. Assuming a GVD of $5 \text{ fs}^2/\text{mm}$ and considering all the other parameters unchanged, the behavior obtained is reported in Fig. 2.2.6 [2].

Due to the positive GVD, the initial 200-fs pulse increases its duration along the propagation, this results in a reduced non-linearity and thus a narrower broadened-spectrum. In fact, Fig. 2.2.6(b) shows that the pulse at 6 cm propagation distance has a duration of ~ 400 fs. Rapid oscillations (inset of Fig. 2.2.6(b)) are present at the steep trailing edge of the pulse, indicating onset of optical wave breaking, which in the spectral domain appears as a pedestal extending to $< 650 \text{ nm}$ (inset of Fig. 2.2.6(a)). It is possible to observe that the positive GVD tends to wash out the lobe structures in the optical spectrum, thus the spectral valley between two adjacent peaks become shallower.

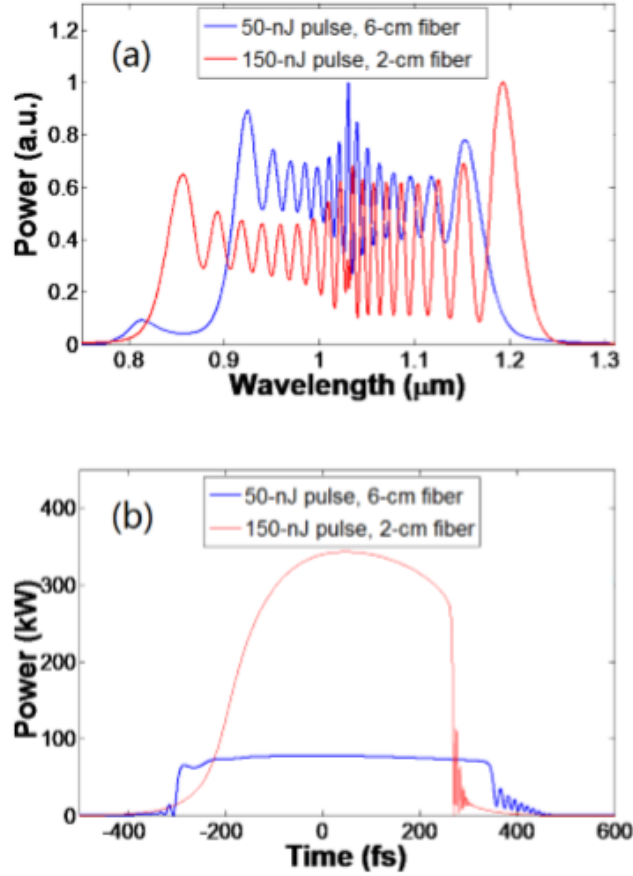


Figure 2.2.7: Evolution of 50 nJ pulses propagating in 6 cm fiber and evolution of 150 nJ pulses propagating in 2 cm fiber. (a) spectral evolution. (b) temporal evolution. [2]

To have better insight of the effect of GVD, another simulation with the GVD increased to $15 \text{ fs}^2/\text{mm}$ (all other parameters unchanged) is presented in Fig. 2.2.7 [2]. The blue curve in Fig. 2.2.7(a) shows that the resulting optical spectrum becomes much narrower and the lobe structures tend to wash out. Due to larger GVD, optical wave breaking occurs also at the leading edge of the pulse and becomes stronger at the trailing edge (blue curve in Fig. 2.2.7(b)), manifesting in the spectral domain as pedestals emerging at both the short- and long-wavelength edges (blue curve in Fig. 2.2.7(a)).

These detrimental effects caused by GVD can be prevented by increasing the input pulse energy and reducing the fiber length. Indeed, Eq. 2.2.6 is unchanged if $A(z, t)$, β_n and z are replaced by $\sqrt{N}A(z, t)$, $N\beta_n$, and z/N , where N is a positive number. This scaling property suggests that increasing the input pulse energy and shortening the propagation distance can cancel out the unfavorable effects of an increased GVD. To confirm this scaling property, a 150 nJ pulse

through 2-cm fiber with $15 \text{ fs}^2/\text{mm}$ GVD is numerically propagated and the results are plot as the red curves in Fig. 2.2.7. As expected, the resulting spectrum (red curve in Fig. 2.2.7(a)) and pulse (red curve in Fig. 2.2.7(b)) share exactly the same profile as their counterparts shown in Fig. 2.2.6(a) and Fig. 2.2.6(b) that are obtained from propagating 50 nJ pulse through 6-cm fiber with $5 \text{ fs}^2/\text{mm}$ GVD. These results suggest an energy scalable approach in implementing wavelength tunable ultra-fast sources: increase input pulse energy and shorten fiber length to minimize the GVD effect such that fiber non-linearities (mainly SPM) dominate the spectral broadening process.

2.3 Raman Scattering

In this section, first the basic concepts of Raman scattering [24] will be presented, then coherent Raman scattering [25] [26] will be introduced and finally FT-CARS [25] [27] will be discussed.

2.3.1 Spontaneous Raman Scattering

When a transparent medium is illuminated with a beam of monochromatic light of wavenumber $\tilde{\nu}_0$, the majority of the incident light gets transmitted without any change, while a smaller portion is scattered within the whole solid angle [24]. The spectral analysis of the scattered light shows that, in addition to scattering without change of wavenumber of the incident light (Rayleigh scattering), there are also discrete components with a different wavenumber. In general, there are pairs of new lines appearing in the spectrum at wavenumbers positioned symmetrically with respect to the Rayleigh line, i.e. $\tilde{\nu}' = \tilde{\nu}_0 \pm \tilde{\nu}_M$, where the wavenumbers $\tilde{\nu}_M$ correspond to transitions between rotational or vibrational energy levels of molecular systems [24]. The appearance of these altered frequencies in scattered light is called Raman effect or Raman scattering, after its discoverer.

Raman scattering is a very weak effect, it is in fact always accompanied with Rayleigh scattering, having an intensity usually 3–5 orders of magnitude greater. Note, however, that Rayleigh scattering itself is only about 10^{-4} – 10^{-3} of the intensity of the incident exciting radiation. The new components appearing in the spectrum at shifted wavenumbers are referred to as Raman lines or Raman bands, and collectively they are called to Raman spectrum. The Raman bands at wavenumbers less than the exciting wavenumber are referred to as Stokes lines, whereas those appearing at higher wavenumbers as anti-Stokes lines.

Lighth-Matter Interaction: a Brief Reminder

According to classical theory, the most efficient source of e.m. radiation is an oscillating electric dipole, with a radiation intensity several orders of magnitude greater than that of other sources of radiation, such as oscillating magnetic dipoles, electric quadrupoles, or higher order multipoles [24]. Thus, in order to understand the origin of scattering of light by molecules, we should consider the distribution of electric charges within the molecule and establish whether there is a permanent or induced electric dipole able to oscillate when modulated by the normal vibrations.

An electric dipole is given by a pair of point charges $-q$ and $+q$ separated by a distance r and it is characterized by its dipole moment vector $\boldsymbol{\mu}$, defined as:

$$\boldsymbol{\mu} = q \mathbf{s} \tag{2.3.1}$$

where \mathbf{s} is a vector pointing from $-q$ to $+q$. If the dipole oscillates at frequency ν , corresponding to the wavenumber $\tilde{\nu} = \nu/c$ (where c is the speed of light), then it emits e.m. radiation at the same frequency. The dipole moment may change during normal vibrations, the nuclei are in fact displaced from their equilibrium position [24]. The change is periodical in time, with the frequency of the given normal vibration ν_M :

$$\boldsymbol{\mu} = \boldsymbol{\mu}_0 \cos 2\pi\nu_M t \quad (2.3.2)$$

where $\boldsymbol{\mu}_0$ is the amplitude vector of the oscillating dipole. This oscillating dipole of the molecule is capable of producing electromagnetic radiation at frequency ν_M ; it is also capable of absorbing radiation of the same frequency, which will excite the given molecular vibration. Scattering of light by a molecule is associated with oscillations of an induced electric dipole. Electric dipoles can be induced by external electric fields, either static or alternating; these external electric fields will polarize the molecule. If this induced dipole oscillates, it can produce electromagnetic radiation. In the case of a static external field, the induced dipole oscillates only with the frequencies of the normal vibrations of the molecule. Instead, in the case of an oscillating field, the induced dipole follows the alternating electric field of the radiation and it is also modulated by the vibrations of the nuclei [24]. As a result, it oscillates at the frequency of the electric field as well as at combination or beat frequencies of the external field frequency and the frequencies of normal vibrations, radiating at all these frequencies.

Classical Treatment of Raman Scattering

The classical theory of Raman scattering is based on the concept that scattered light is generated by oscillating electric dipoles induced by the electric field of incident radiation [24]. The relation between the induced dipole moment vector $\boldsymbol{\mu}'$ and the electric field vector \mathbf{E} can be written in the form of the following power series:

$$\boldsymbol{\mu}' = \boldsymbol{\alpha}\mathbf{E} + \frac{1}{2}\boldsymbol{\beta}\mathbf{E}\mathbf{E} + \frac{1}{6}\boldsymbol{\gamma}\mathbf{E}\mathbf{E}\mathbf{E} + \dots \quad (2.3.3)$$

where $\boldsymbol{\alpha}$ is the polarizability, $\boldsymbol{\beta}$ the hyperpolarizability, and $\boldsymbol{\gamma}$ the second hyperpolarizability of the molecule, all of them are tensors.

The polarizabilities can be interpreted as the measure of the flexibility of the electron cloud: it describes how easily the electron cloud of the molecule can be deformed or displaced to produce an electric dipole due the influence of the external electric field [24]. The nonlinear terms in Eq. 2.3.3 are usually small compared to the linear term, so they can be neglected in normal, linear Raman scattering.

If we restrict the discussion to the linear term in Eq. 2.3.3, we have:

$$\boldsymbol{\mu}' = \boldsymbol{\alpha}\mathbf{E} \quad (2.3.4)$$

that can be written in matrix form as:

$$\begin{bmatrix} \mu'_x \\ \mu'_y \\ \mu'_z \end{bmatrix} = \begin{bmatrix} \alpha_{xx} & \alpha_{xy} & \alpha_{xz} \\ \alpha_{yx} & \alpha_{yy} & \alpha_{yz} \\ \alpha_{zx} & \alpha_{zy} & \alpha_{zz} \end{bmatrix} \begin{bmatrix} E_x \\ E_y \\ E_z \end{bmatrix} \quad (2.3.5)$$

The polarizability tensor can be described by a real, symmetric matrix, where all $\alpha_{ij} = \alpha_{ji}$; thus it has at most six independent components: three diagonal and three off diagonal.

Consider now the time dependence of the induced dipole moment defined in Eq. 2.3.4 in a vibrating molecule, where the polarizability tensor can be modulated by the normal vibrations [24]. The dependence of the polarizability on the normal coordinates can be expressed in the form of the following Taylor series:

$$\alpha_{ij} = (\alpha_{ij})_0 + \sum_k \left(\frac{\partial \alpha_{ij}}{\partial Q_k} \right)_0 Q_k + \frac{1}{2} \sum_{k,l} \left(\frac{\partial^2 \alpha_{ij}}{\partial Q_k \partial Q_l} \right)_0 Q_k Q_l + \dots \quad (2.3.6)$$

where α_{ij} is an element of the polarizability tensor and $(\alpha_{ij})_0$ is its evaluation in the equilibrium configuration; Q_k is the normal coordinate associated with the vibration of wavenumber $\tilde{\nu}_k$ and one can see all the derivatives are evaluated in the equilibrium configuration.

We proceed with the double harmonic approximation, neglecting both the mechanical and electrical anharmonicities. On the one hand, linear dependence of polarizability on each vibrational coordinate is assumed:

$$\boldsymbol{\alpha}_k = \boldsymbol{\alpha}_0 + \left(\frac{\partial \boldsymbol{\alpha}}{\partial Q_k} \right)_0 Q_k \quad (2.3.7)$$

and on the other hand, vibrations are treated as harmonic:

$$Q_k = Q_{k0} \cos 2\pi c\tilde{\nu}_k t \quad (2.3.8)$$

Consider now the time dependence of the induced electric dipole moment $\boldsymbol{\mu}'$, generated under the influence of the electric field of incident radiation of wavenumber $\tilde{\nu}_0$ in a vibrating molecule [24]. The variation of the electric field with time is given by:

$$\mathbf{E} = \mathbf{E}_0 \cos 2\pi c\tilde{\nu}_0 t \quad (2.3.9)$$

Inserting Eq. 2.3.7 and Eq. 2.3.9 into Eq. 2.3.4 and performing some trigonometric transformations, for the k th vibration one obtain [24]:

$$\begin{aligned} \boldsymbol{\mu}' = & \boldsymbol{\alpha}_0 \mathbf{E}_0 \cos 2\pi c\tilde{\nu}_0 t + \frac{1}{2} \left(\frac{\partial \boldsymbol{\alpha}}{\partial Q_k} \right)_0 Q_{k0} \mathbf{E}_0 \\ & \times [\cos 2\pi c(\tilde{\nu}_0 - \tilde{\nu}_k)t + \cos 2\pi c(\tilde{\nu}_0 + \tilde{\nu}_k)t] \end{aligned} \quad (2.3.10)$$

There are three cosine terms in the equation, with different arguments, therefore the dipole is oscillating at three different frequencies simultaneously [24]. The first term is the Rayleigh scattering, observable at $\tilde{\nu}_0$, while the second and third terms account for Stokes Raman and anti-Stokes Raman scattering at $\tilde{\nu}_0 - \tilde{\nu}_k$ and $\tilde{\nu}_0 + \tilde{\nu}_k$. These beat frequencies are produced when the oscillating dipole is modulated by the molecular vibration.

Classical theory is thus able to successfully describe the frequency relationship of vibrational Raman scattering, showing that the Raman shift is independent on the frequency of the incident radiation. Raman shifts are in fact characteristic of the scattering molecule and this is the reason why each molecule has a distinct Raman spectrum.

Partial Quantum Treatment of Raman Scattering

According to the principles of quantum mechanics, the energy associated with electronic, vibrational and rotational degrees of freedom of a molecule can only take values from a discrete set, the quantized energy levels corresponding to the possible stationary states of the molecule. As well as their energies, these states are also characterized by a set of quantum numbers and by a wavefunction Ψ . In terms of quantum mechanics, radiation is absorbed or emitted by a molecular system as the result of an upward or downward transition between two energy levels, so the radiation absorbed or emitted is also quantized, with the energy

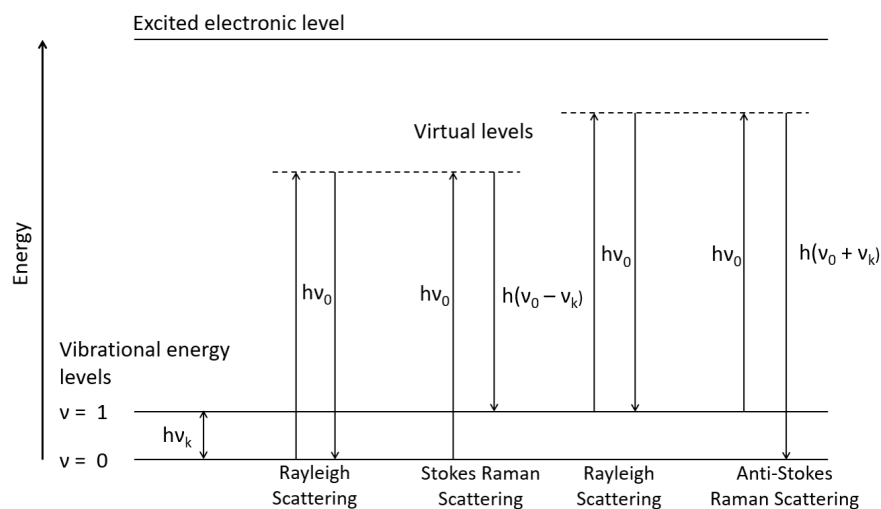


Figure 2.3.1: Diagram of transitions between vibrational energy levels corresponding to the processes of Rayleigh and Raman scattering.

enclosed in discrete photons [24]. The loss or gain of energy by the molecule is proportional to the wavenumber of the radiation:

$$\Delta E = h\nu = h\tilde{\nu}_k c \quad (2.3.11)$$

where h is the Planck constant.

Both Rayleigh and Raman scattering involve two almost simultaneous transitions proceeding via virtual states in which one photon of the incident radiation is annihilated and another photon, of the same energy, in case of Rayleigh scattering, or of lower energy or higher energy, in case of Stokes Raman and anti-Stokes Raman scattering respectively, is created, as shown in Fig. 2.3.1.

The term "virtual state" is used to refer to a transition state which does not correspond to an eigenstate of the molecule; it is only an imaginary state by which the energy exchange between the radiation field and the molecule during the scattering process can be split up into two one-photon transitions [24].

We proceed by presenting the results of a partial quantum mechanical treatment in which the molecule is treated quantum mechanically while the radiation still classically. For the description of the light-matter interaction, e.m. radiation is regarded as a perturbation for the molecular system. This partial quantum mechanical treatment yields correct results for most spectroscopic processes including Rayleigh and Raman scattering.

Any direct transition between two energy levels is accompanied with emission or absorption of radiation if the dipole moment of the transition, called transition moment, is different from zero:

$$\mu_{fi} = \langle \Psi_f | \hat{\mu} | \Psi_i \rangle \quad (2.3.12)$$

where Ψ_i and Ψ_f are the wavefunctions of the initial and final states, respectively, $\hat{\mu}$ is the dipole moment operator and the Dirac notation is used.

The quantum mechanical equivalent of the amplitude of the induced dipole of Eq. 2.3.4 is the transition moment amplitude related to the transition from an initial state i to a final state f , induced by radiation of wavenumber $\tilde{\nu}_0$:

$$\langle \mu_0 \rangle_{fi} = \langle \Psi_f | \boldsymbol{\alpha} | \Psi_i \rangle \mathbf{E}_0 \quad (2.3.13)$$

Since the frequency dependence of Raman scattering was correctly obtained from the classical theory, it is now interesting to determine the intensity of scattered radiation for a given vibrational transition. Thus, it is possible to avoid the consideration of the time dependence and examine only the transition moment amplitudes, considering Ψ_f and Ψ_i as time-independent vibrational wavefunctions [24]. The Raman selection rules and the intensity of the scattered radiation will be determined by the transition polarizability tensor $\boldsymbol{\alpha}_{if}$, whose components are the matrix elements of the polarizability tensor for the $i \rightarrow f$ transition. Thus it is necessary to examine the dependence of the transition polarizabilities on the vibrational normal coordinates in a manner similar to classical mechanics [24]. Neglecting again electrical and mechanical anharmonicities and exploiting the properties of the harmonic oscillator wavefunctions, one obtains that only those matrix elements, for which *one* vibrational quantum number changes by a unity ($v_k^f = v_k^i \pm 1$), differ from zero; all other vibrational quantum numbers remain unchanged ($v_j^f = v_j^i$, for all $j \neq k$). Then for a matrix element of the transition polarizability associated with Stokes Raman scattering ($v_k^f = v_k^i + 1$) at Raman shift $\tilde{\nu}_k$ we obtain [24]:

$$[\alpha_{xy}]_{v^f v^i} = (v_k^i + 1)^{\frac{1}{2}} b_{v_k} \left(\frac{\partial \alpha_{xy}}{\partial Q_k} \right)_0 = (v_k^i + 1)^{\frac{1}{2}} b_{v_k} (\alpha'_{xy})_k \quad (2.3.14)$$

Similarly, for anti-Stokes scattering ($v_k^f = v_k^i - 1$) [24]:

$$[\alpha_{xy}]_{v^f v^i} = (v_k^i)^{\frac{1}{2}} b_{v_k} \left(\frac{\partial \alpha_{xy}}{\partial Q_k} \right)_0 = (v_k^i)^{\frac{1}{2}} b_{v_k} (\alpha'_{xy})_k \quad (2.3.15)$$

where $b_{v_k}^2 = h/(8\pi^2 c \tilde{\nu}_k)$ is the quantum mechanical analog of the amplitude Q_k of the classical oscillator. From the last two equations, one can see that

for such transitions to be Raman active it is also required that at least one component of the polarizability tensor is nonzero, as in classical theory. A significant difference between the classical and quantum mechanical treatments is that in the latter there is a dependence on ν_k , leading to important consequences concerning the intensities of the Raman scattering [24].

The most pronounced difference is found in the relative intensities of the Stokes and anti-Stokes Raman lines [24]:

$$\frac{I_{Stokes}}{I_{anti-Stokes}} = \frac{I_{\tilde{\nu}_0 - \tilde{\nu}_k}}{I_{\tilde{\nu}_0 + \tilde{\nu}_k}} = \frac{(\tilde{\nu}_0 - \tilde{\nu}_k)^4}{(\tilde{\nu}_0 + \tilde{\nu}_k)^4} \exp\left(\frac{hc\tilde{\nu}_k}{kT}\right) \quad (2.3.16)$$

In addition to correctly accounting for the observed intensity relationships, this equation allows determination of the sample temperature by contact-free measurement.

Spontaneous Raman Spectroscopy

The simplest implementation of Raman spectroscopy is based on spontaneous Raman emission and it has many applications in different fields of physics, chemistry and biology. This technique presents different advantages with respect to others: high spatial resolution, minimum sample preparation and low damage if near-infrared radiation is used [26]. However, the technique is not free of drawbacks. The main disadvantage, as mentioned before, is the extremely small cross-section of Raman scattering compared with Rayleigh or fluorescence scattering, thus requiring a relatively long acquisition time to get a result with an acceptable signal to noise ratio. Moreover, the fluorescence signal and the spontaneous Raman Stokes signal are spectrally overlapped, thus they cannot be separated by mean of an optical filter. For this reason, relevant peaks can be hidden or there can be a decreased sensitivity.

2.3.2 Coherent Raman Scattering

The spontaneous Raman signal is an incoherent signal: the phase of the wave emitted by a single molecule is not correlated with the others in the sample [26]. The reason why is that the system input is only given by a single pumping frequency ω_p while a second frequency, ω_s , is spontaneously emitted. Coherent Raman scattering (CRS) instead is a parametric four-wave mixing process and exploits a type of light-matter interaction in which two synchronized train of pulses at ω_p and ω_s ($\omega_p > \omega_s$) are incident on the sample and the material response depends on their difference $\Omega = \omega_p - \omega_s$. In particular, Ω can be tuned to the vibrational modes, ω_v , of the material under study, thus achieving stimulated excitation of vibrational transitions. In CRS the molecule bonds oscillate in phase and the signal can be several order of magnitude higher [26].

The advantages of vibrational imaging through coherent Raman scattering are many [26]:

1. it does not require molecule staining;
2. there is no population transfer to the electronic states so there is no sample damage;
3. the sensitivity is higher than spontaneous Raman;
4. the signal generation mechanism intrinsically allows 3D sectioning capability;
5. near-IR excitation avoids sample heating because of water absorption, and allows a deep penetration depth;
6. being based on ultrashort pulses CRS allows to time resolve Raman free induction decay which can be the base for an additional chemical contrast mechanism.

The coherent anti-Stokes Raman scattering (CARS) and the stimulated Raman scattering (SRS) are the most common CRS techniques, in this thesis the focus will be on CARS.

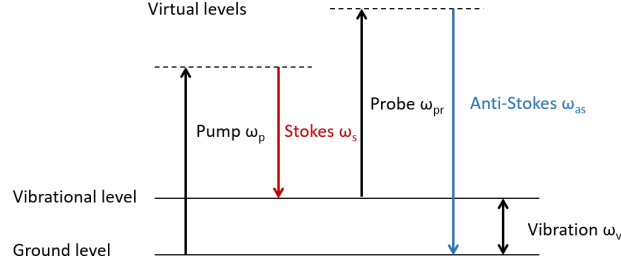


Figure 2.3.2: Energy diagram of two-color CARS process, all the input pulses are narrow-band.

CARS - Coherent anti-Stokes Raman Spectroscopy

Coherent anti-Stokes Raman scattering (CARS) is a nonlinear Raman spectroscopy technique involving three laser pulses: the pump, the Stokes and the probe beam, whose frequencies are referred to as ω_p , ω_s and ω_{pr} respectively [26]. Interacting with the sample, they generate a blue-shifted anti-Stokes field at $\omega_{as} = \omega_p - \omega_s + \omega_{pr}$ which is resonantly enhanced when the Raman shift $\omega_{pr} - \omega_s$ coincides with the frequency of a Raman active molecular vibration. We will consider two-color CARS, in which $\omega_p = \omega_{pr}$, as shown in Fig.2.3.2. One of the main advantages of CARS is that, being an anti-Stokes process, it is emitted in a frequency range where no fluorescence is emitted. Thus, it is possible to obtain fluorescent-free spectra.

CARS is a third order non-linear process, we can write the third order polarization at the anti-Stokes frequency, in the case of two-color CARS, as:

$$P^{(3)} = \chi^{(3)} E_p^2 E_s^* \quad (2.3.17)$$

where $\chi^{(3)}$ is the third order non-linear susceptibility, E_p is the electric field related to the pump and the probe and E_s is related to the Stokes beam. The symbol * stands for complex conjugate.

$\chi^{(3)}$ can be written as [28]:

$$\chi^{(3)} = \frac{A_R}{\Omega - (\omega_p - \omega_s) - i\Gamma_R} + \chi_{NR}^{(3)} \quad (2.3.18)$$

where Ω is the vibrational frequency, Γ_R is the HWHM of the Raman line, A_R is the Raman scattering cross-section and $\chi_{NR}^{(3)}$ is the non-resonant third order susceptibility. One can see that the first term of Eq.2.3.18 is a resonant contribution, reaching its maximum for $\Omega = \omega_p - \omega_s$ [26]. The second term represents instead the non-resonant contribution, which is due to the electronic contribution and it is real and constant and an example is shown in Fig.2.3.3.

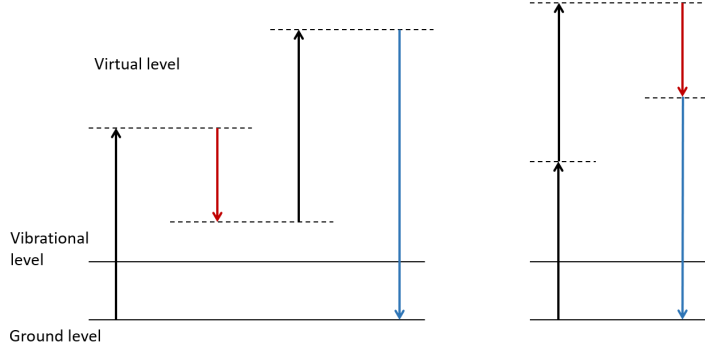


Figure 2.3.3: Energy diagram of non-resonant processes.

It is possible to derive the expression of the intensity of the CARS signal, resulting in [28]:

$$I_{CARS} \approx |\chi^{(3)}|^2 I_p^2 I_s \left[\frac{\sin(|\Delta\mathbf{k}| \cdot L/2)}{|\Delta\mathbf{k}|/2} \right]^2 \quad (2.3.19)$$

where I_s and I_p are the Stokes and pump intensities under non depletion approximation, L is the length of the propagation in the sample and $\Delta\mathbf{k}$ is the wavevector mismatch, given by $\Delta\mathbf{k} = \mathbf{k}_{as} - (2\mathbf{k}_p - \mathbf{k}_s)$. The dependence on $\Delta\mathbf{k}$ shows that the CARS signal depends on the directions of the involved beams [26]; it is clear that the intensity is maximized when the wavevectors satisfy the phase matching condition:

$$|\Delta\mathbf{k}|L = |\mathbf{k}_{as} - (2\mathbf{k}_p - \mathbf{k}_s)|L < \pi \quad (2.3.20)$$

The aforementioned condition is shown in Fig.2.3.4.

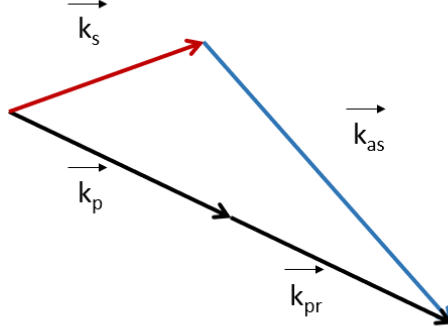


Figure 2.3.4: Phase matching condition.

In order to make further considerations on the intensity, we can write the susceptibility as:

$$\chi^{(3)} = \chi_{NR}^{(3)} + Re\{\chi_R^{(3)}\} + iIm\{\chi_R^{(3)}\} \quad (2.3.21)$$

which is the sum of a non-resonant part (NR) and a resonant part (R), divided in its real and imaginary parts. It is possible to derive that, for two-color CARS, the resonant component can be written in the following simpler way [26]:

$$\chi_R^{(3)} \propto \sum_r \frac{N}{\Delta_r - i\Gamma_r} \quad (2.3.22)$$

where the sum is performed over all the r th Raman active modes. N is the density of active Raman scatterers, Δ_r is the detuning $\Delta_r = \Omega_r - (\omega_p - \omega_s)$ and Γ_r is again the HWHM of the r th Raman line. We can thus see, that the intensity of the CARS signal will be proportional to the square of the scatterers density. In terms of real and imaginary part, considering a single Raman active mode:

$$Re\{\chi_R^{(3)}\} \propto \frac{N\Delta}{\Delta^2 + \Gamma^2} \quad (2.3.23)$$

$$Im\{\chi_R^{(3)}\} \propto \frac{N\Gamma}{\Delta^2 + \Gamma^2} \quad (2.3.24)$$

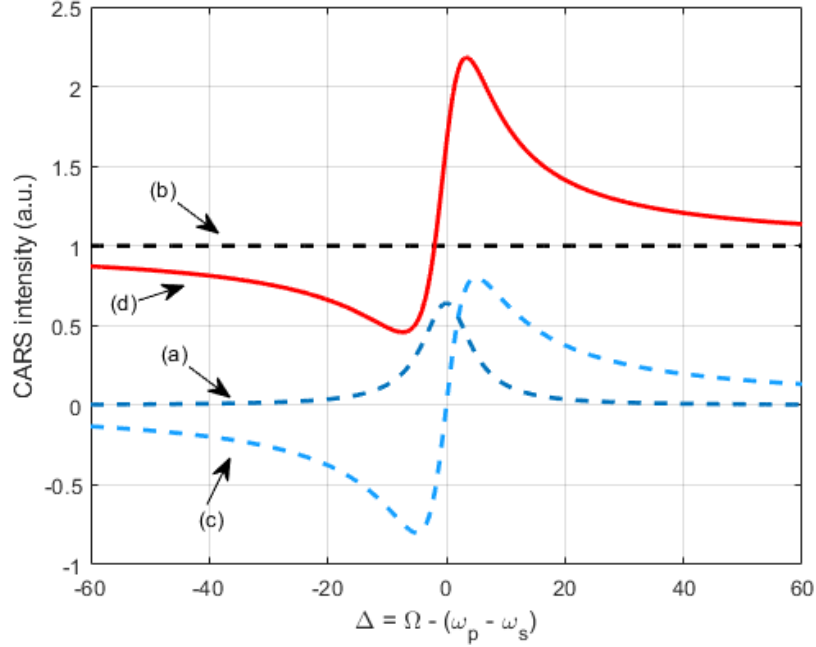


Figure 2.3.5: (a) Purely resonant contribution; (b) Purely non-resonant contribution; (c) Dispersive mixing term $2Re\{\chi_R^{(3)}\}\chi_{NR}^{(3)}$; (d) Typical line shape of the CARS intensity for a single resonance.

Thus, the measured intensity is proportional to the modulus square of $\chi^{(3)}$:

$$I_{CARS} \propto |\chi^{(3)}|^2 = |\chi_R^{(3)} + \chi_{NR}^{(3)}|^2 = |\chi_R^{(3)}|^2 + |\chi_{NR}^{(3)}|^2 + 2Re\{\chi_R^{(3)}\}\chi_{NR}^{(3)} \quad (2.3.25)$$

The behavior of the different contributions is shown in Fig.2.3.5, together with the overall intensity behavior.

One can notice that the non-linear mixing term between resonant and non-resonant components leads to a red-shift of the peak frequency [26]. We can also see that the non-resonant contribution increases the real part of the of $\chi_R^{(3)}$. Since the non-resonant contribution is in general unknown, this distortion makes the interpretation of CARS spectra difficult resulting in the major drawback of this technique. The non-resonant background is therefore problematic since [26]:

1. It generates spectral distortion;
2. It can generate image artifacts;
3. It introduces a non-linear dependence between the signal strength and the number of scatterers;
4. It limits the ultimate sensitivity of the technique.

These clearly represent a disadvantage of CARS when compared to other techniques which are insensitive to the to the non-resonant background or do not present it.

2.3.3 FT-CARS - Fourier Transform CARS

CARS microscopes can be tuned to detect a specific molecule vibration. This is inefficient and, besides, dynamical changes in a whole spectrum are difficult to follow [26]. The concept of the Fourier transform CARS was proposed and demonstrated in 1985 [29]. Two different color picosecond pulses excite molecular vibrations and the delayed probe pulse is scattered off and generates the anti-Stokes radiation. The vibrational modulation was observed on the intensity of the anti-Stokes radiation and Fourier transform of the modulation reveals the Raman vibrational spectrum [25]. The concept of Fourier transform CARS has been extended to a single femtosecond pulse excitation combined with a Michelson interferometer [30] [31] or a pulse-shaping method [32] instead of two picosecond pulses excitation.

Basic Principles

We start by describing the principles of FT-CARS spectroscopy combined with a Michelson interferometer [27]. We consider a femtosecond laser beam with a pulse repetition rate of f_{rep} , split by a beamsplitter into two arms of a Michelson interferometer. The end mirror in one of the arms, called reference arm, is fixed while the end mirror in the other arm, called scanning arm, is scanned in time. Assuming that the scanned pulse train's interval between consecutive pulses is $1/f_{rep} + \Delta t$, for every pair of nearby scanned and reference pulses, the CARS process starts with the excitation of the sample by the reference pulse.

The use of the femtosecond pulse laser enables coherent excitation of every molecular vibrational mode within the laser's broad spectral bandwidth. The subsequent scanned pulse either amplifies or weakens the coherent molecular vibration depending on its arrival time [33], indicating that the molecule's vibrational mode is encoded onto the time-domain waveform of the resulting blue-shifted anti-Stokes beam as shown in Fig. 2.3.6.

Once the blue-shifted anti-Stokes signal is extracted, it is digitized and processed by a computer to retrieve the CARS spectrum. Note that the molecular vibration is probed with a constant temporal resolution Δt , while each CARS process is probed with a refreshing period of $1/f_{rep}$, thus the detected waveform is a replica of the molecular vibration whose frequency is down-converted by a factor:

$$F = f_{rep}\Delta t \tag{2.3.26}$$

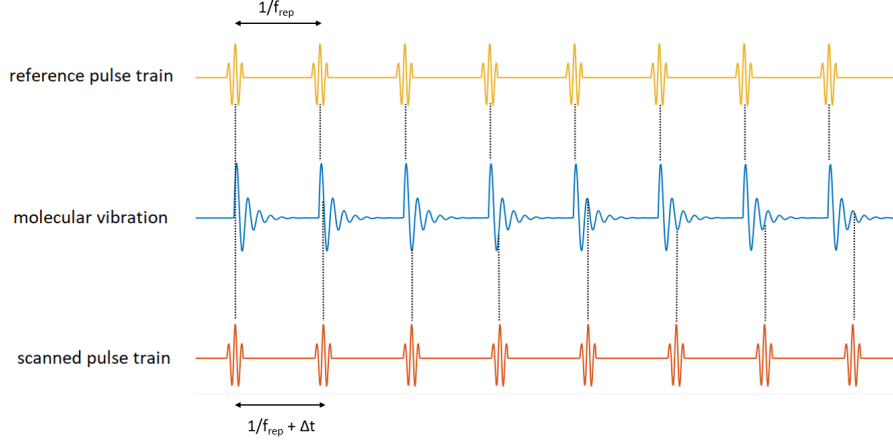


Figure 2.3.6: Generation of FT-CARS signal from one molecular vibrational mode.

This down-conversion F maps the THz frequency of the molecular vibration to a detectable MHz frequency, enabling a fast readout with a simple photodiode. The CARS spectrum of the sample is then retrieved by Fourier-transforming the acquired time-domain signal, referred to as CARS interferogram, consisting of multiple down-converted molecular vibrational frequencies. The non-resonant background, given by instantaneous electronic transitions can be eliminated by cutting out the zero-temporal-delay region of the interferogram [31].

The higher frequency limit of the Raman spectral region is given by the bandwidth of the frequency components that induce the CARS process, whereas the lower-frequency limit is given by the difference between the optical long-pass and short-pass boundary frequencies. However, due to the Nyquist-Shannon sampling theorem, a frequency that can be recovered from a pump-probe measurement is also limited by the pulse repetition rate, thus limiting the Raman spectral region to:

$$f_{high} = \frac{f_{rep}}{2F} \quad (2.3.27)$$

Theoretical Description

In femtosecond Fourier transform CARS, the electric field, which induces the non-linear polarization, consists of two pulse fields $E_1(t)$ and $E_2(t - \tau)$ with delay τ [25]:

$$E(\tau, t) = E_1(t) + E_2(t - \tau) \quad (2.3.28)$$

We can write the third order polarization induced by the field $E(t, \tau)$ as [25]:

$$\begin{aligned} P_{FT-CARS}(\tau, t) &= (\chi_R^{(3)} + \chi_{NR}^{(3)})E(\tau, t)E^*(\tau, t)E(\tau, t) \\ &= P_R^{(3)}(\tau, t) + P_{NR}^{(3)}(\tau, t) \end{aligned} \quad (2.3.29)$$

The total FT-CARS signal is described as a function of delay τ [25]:

$$S_{FT-CARS}(\tau) \propto \int_0^\infty dt |P_{FT-CARS}(\tau, t)|^2 \quad (2.3.30)$$

The polarization $P_{FT-CARS}(\tau, t)$ consists of a number of different processes. We are interested in the processes which depend on the delay τ and those which interfere with them. Therefore, the processes we investigate can be described [25]:

$$P_{FT-CARS}(\tau, t) \approx P_{R,1,2}^{(3)}(\tau) + P_{NR,1,2}^{(3)}(\tau) + P_{R,2}^{(3)} + P_{NR,2}^{(3)} \quad (2.3.31)$$

The first term $P_{R,1,2}^{(3)}(\tau)$ represents the process where pulse 1 excites the vibrational coherence and pulse 2 probes it. The second term $P_{NR,1,2}^{(3)}(\tau)$ represents the non-resonant processes both pulse 1 and pulse 2 contribute to, but these processes only happen when $\tau \approx 0$, so to avoid them it is possible to avoid looking at the signal for $\tau \approx 0$. The third and fourth terms, $P_{R,2}^{(3)}$ and $P_{NR,2}^{(3)}$ represent the processes only pulse 2 contributes to. They do not depend on τ but they may interfere with the first term because they are all generated at the same time [25]. We can ignore the processes governed only by pulse 1 because such induced polarizations do not interfere with the first term.

Thus, the modulated part of the FT-CARS signal, which depends on the delay τ is given by [25]:

$$\begin{aligned} S_{FT-CARS}(\tau) &\approx \text{Re}[P_{R,1,2}^{(3)*}(\tau)P_{R,1,2}^{(3)}(\tau) + P_{R,1,2}^{(3)*}(\tau)P_{R,2}^{(3)} + P_{R,1,2}^{(3)*}(\tau)P_{NR,2}^{(3)}] \\ &\propto \chi_R^{(3)} I_1^2 I_2 + \chi_R^{(3)} I_1 I_2^2 + \chi_R^{(3)} \chi_{NR}^{(3)} I_1 I_2^2 \end{aligned} \quad (2.3.32)$$

where I_1 and I_2 are the intensities of pulse 1 and 2. The three processes are detected at the same time. All of them share the feature that the pulse 1 excites the vibrational coherence and the pulse 2 probe it. The second and third terms are sort of heterodyne signals. The contribution of these processes depends on the sample and the condition of the pulses.

Chapter 3

Laser Source

The purpose of this chapter is to give an initial historical introduction on doped fiber laser, fiber amplification and supercontinuum generation; consequently the focus will be addressed on the experimental setup. At first, a general overview of the working mechanism will be presented, subsequently a more detailed analysis of the single components will be developed. In conclusion the achieved results will be exposed.

3.1 Historical Introduction

The concept of using fiber waveguide structures as optical gain media was first proposed by Snitzer *et al.* [14] as early as 1961. Potential single mode operation was the main reason for interest in fiber based optical systems since it would enable excellent beam quality.

Initially, Neodymium and Erbium were the dopants of highest interest in this application: the first one due to high power and efficiency of the 1060 nm transition, while the second one for the characteristic emission at 1.55 μm , thus available for telecommunication purpose [2].

Even though these dopants were extremely popular, they presented some significant disadvantages, as the excited state absorption for Erbium-doped fibers and the limited emission bandwidth in Neodymium-doped fibers.

Need for higher output powers and growth of fiber-based applications beyond the telecommunication industry, triggered the study of other rare earth dopants to overcome limitations related to Er and Nd: as object of our work, we will focus on Ytterbium-doped fiber as low energy pulses amplification system, with the purpose to generate supercontinuum radiation, enabling FT-CARS detection.

Light amplification in Ytterbium involves two energy levels manifold separated by an extremely small energy gap resulting in extremely low quantum defects:

high power efficiency is thus achievable and detrimental effects are significantly reduced [6]; in particular we can observe an extremely low quantum defect, $[(h\nu_p - h\nu)/h\nu_p \simeq 9\%]$ and hence a very low fractional heating with a consequent reduction of undesirable thermal effects. Furthermore, due to the simple energy level structure, one can use high doping levels without incurring in fluorescence quenching phenomena [7].

Pulses obtained through amplification within Yb high-doped fiber showed a bandwidth non sufficiently wide to be an information gathering tool for FT-CARS detection; the invention of nonlinear pure-silica photonic crystal fibers (PCF) in the 1990s stimulated a dramatic development in 1999 [34], termed as the “supercontinuum revolution”. The phenomenon of supercontinuum generation, manifested as the extreme spectral broadening of an optical pulse due to light-medium interaction, was first discovered in bulk materials [35]. However, the phenomenon occurring in optical fibers allows wide and cost-effective access to the supercontinuum, resulting in a pulsed laser-like source spanning a broad bandwidth. Thus, many biophotonics applications were greatly enhanced by the use of fiber supercontinuum generation in the past decade [36]: in our thesis, broadband pulses will be exploited to stimulate anti-Stokes emission from 500 cm^{-1} to 2000 cm^{-1} .

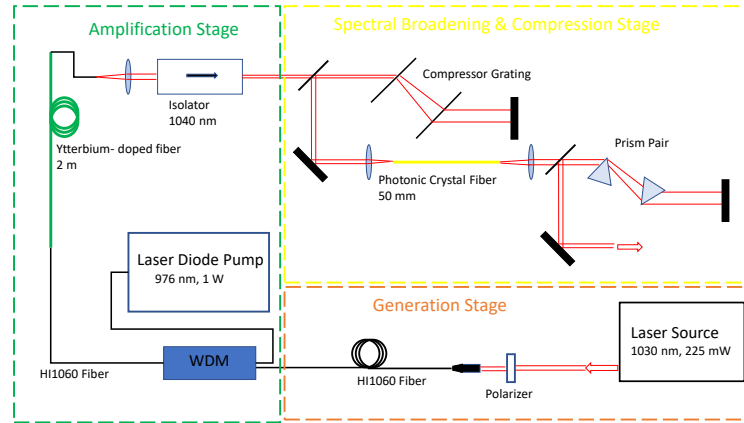


Figure 3.2.1: Experimental Setup

3.2 Experimental Setup

The structure of the source relies on three main stages as shown in figure 3.2.1: Pulse Generation, Pulse Amplification and Spectral Broadening.

In order to properly characterize the pulse during its propagation through these three main stages, a commercial autocorrelator (FR-103XL, FemtoChrome) was used.

3.2.1 Pulse Generation

The generation of light pulses is operated by an Yb-fiber femtosecond laser (Origami, OR/SMGNAS/100/10295/200/120/FS). This laser works in mode locking regime, generating pulses of 171 fs, average output power of 225 mW and a repetition rate of 100 Mhz.

The train of pulses passes through a polarizer attenuating its intensity and is thus coupled in the HI1060 Fiber, ready to be injected in Amplification stage.

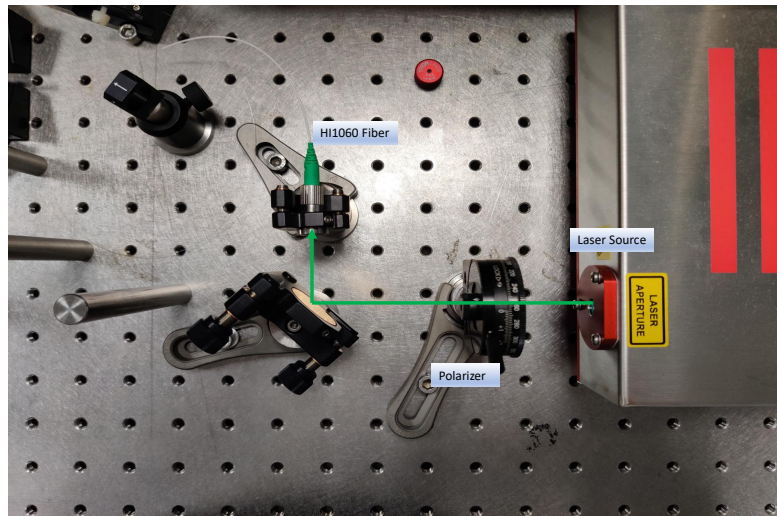


Figure 3.2.2: Pulse generation stage.

3.2.2 Pulse Amplification

In order to achieve the power of 0.92 W to operate the spectral broadening, a stage of pulse amplification is required.

This is performed through the use of a high-power fiber laser diode driven by a compact current driver (Wavelength Electronics, mod. LDTC 2/2E): the pump is thus coupled with the pulse through the use of a Wavelength Division Multiplexer (WDM, DPMP Photonics mod. FWDM-9806-NNN-BBB-1). The amplification mechanism occurs within the gain fiber: this is a Yb-doped double-clad fiber (Coractive model DCF-YB-20/128E) of length 2 m.

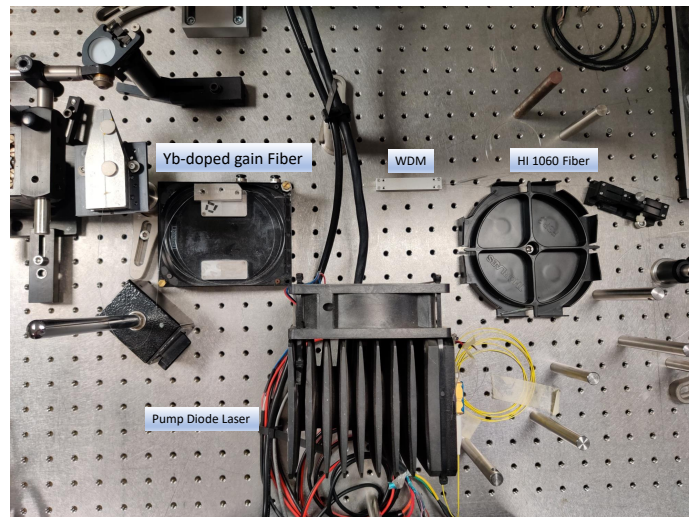


Figure 3.2.3: Pulse amplification stage.

3.2.3 Spectral Broadening and Pulse Compression

Once the pulse have been amplified within the double clad fiber, it passes through a grating compressor (LightSmyth Technologies, 1000 lines/mm) providing compensation of the GVD by fine tuning of the grating distance.

The pulse continues its propagation through a Photonic Cristal Fiber (NKT Photonics, LMA-PM-5 Large-Mode-Area Photonic Crystal Fiber, 5.0- μm core, 5 cm length) which aims to obtain a supercontinuum radiation extended from 900 nm to 1200 nm.

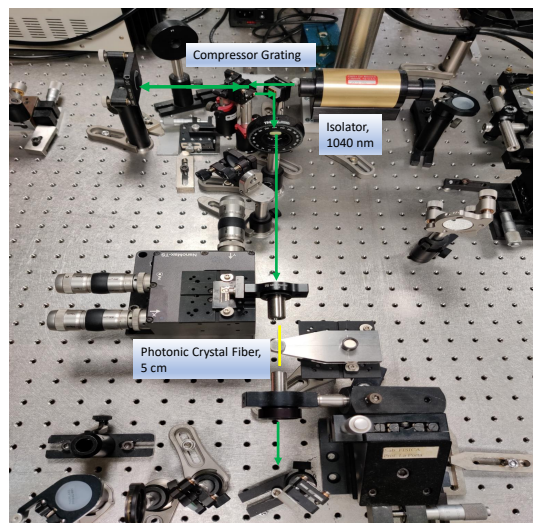


Figure 3.2.4: Spectral broadening and pulse compression stage.

3.2.4 Autocorrelation Setup

The need to know pulse duration within each stage previously described was satisfied through a intensity autocorrelation characterization technique.

FR-103XL Autocorrelator allows to characterize the incoming pulse through the non-collinear background-free Second Harmonic Generation (SHG) method; since the highest resolution settings (1 fs) were exploited, a Fringe Resolved AutoCorrelation (FRAC) was obtained.

The choice of this specific autocorrelator was led by different factors: due to the extremely low material dispersion, it allows to achieve a resolution lower than 5 fs; moreover, the delay line based on rotating parallel mirrors results in a reliable and error-free delay generation.

As shown in figure 3.2.6 a second order non linear crystal was exploited, in particular a 1 mm layer of LiIO_3 providing an operation range over IR wavelenghts [700-1800 nm].

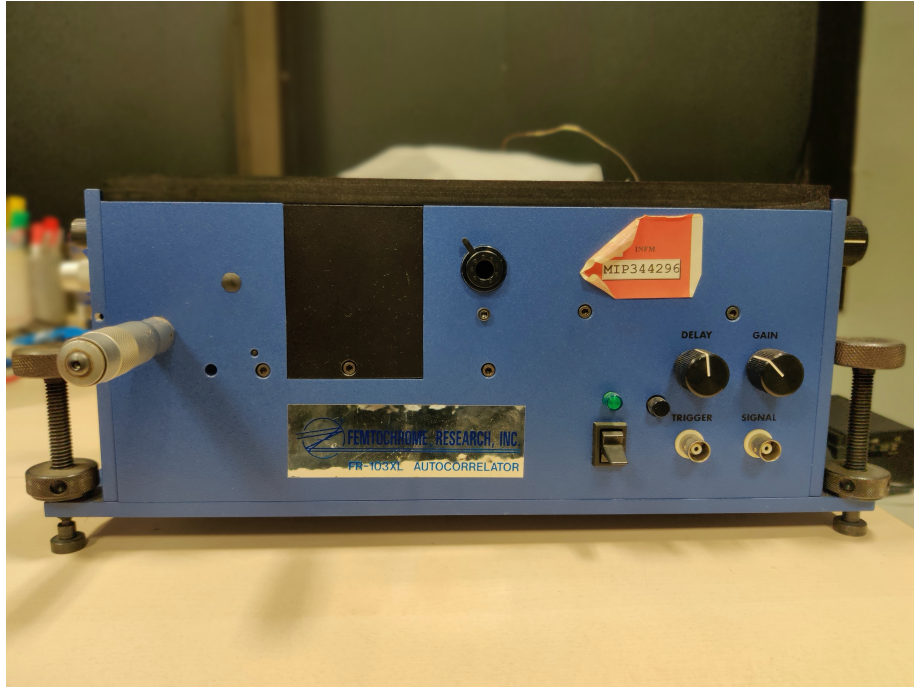


Figure 3.2.5: Commercial Autocorrelator, FR-103XL FemtoChrome

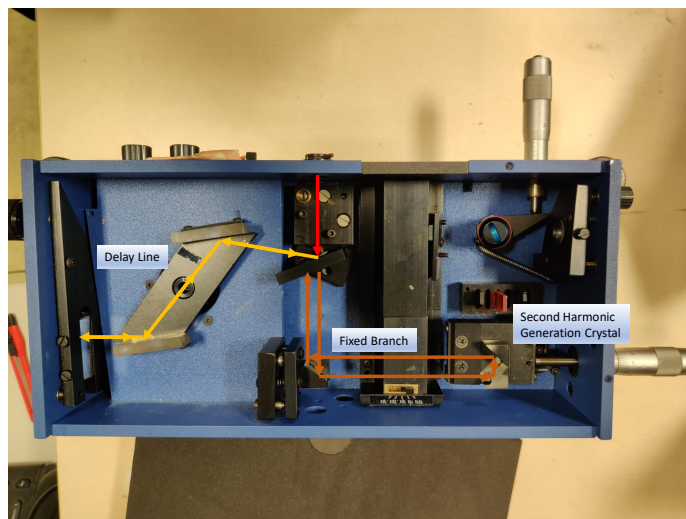


Figure 3.2.6: Internal insight of Commercial Autocorrelator, FR-103XL FemtoChrome

3.3 Setup Components

3.3.1 Low Power Ytterbium Fiber Laser

Among the compressible fiber continuum sources, the solid-state Yb laser-pumped fiber continuum developed recently appears to be a practical alternative to the ultrabroadband Ti:sapphire oscillator in terms of broad bandwidth, average power, pulse energy, and spectral power density [6].

To generate near transform-limited (TL) <20 fs fiber continuum pulses, it has been considered beneficial to select a short incident laser pulse, ≈ 110 fs and an average power transmitted in the fiber of 0.92 W. We note that these two conditions are intended to improve the coherence of the continuum conventionally generated by a PCF having a zero-dispersion-wavelength (ZDW) located inside the spectral range of the continuum. The reason such zero-dispersion PCF is of interest is because it can invoke soliton dynamics to generate the broadest continuum, which in principle, could lead to the shortest pulse [37].

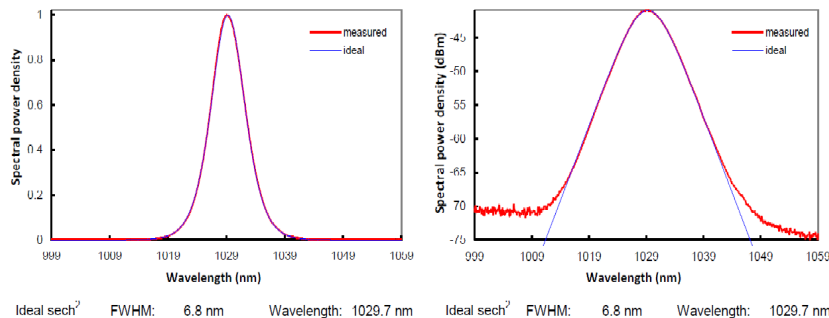


Figure 3.3.1: Spectral Power Density of The low power Yb laser

Low power pulses generation is realized through a commercial Ytterbium mode locked femtosecond Laser (OR/SMGNAS/100/10295/200/120/FS): it produces pulses of average output power 225 mW, duration 171 fs and repetition rate 99.95 MHz.

The full characterization of the pulse outgoing from the low power laser is required in order to evaluate our capability to generate coherent and transform limited supercontinuum radiation.

A first analysis of the spectral power density was made; as shown in figure 3.3.1, experimental results perfectly fit the model of solitonic pulse, presenting the shape of a sech^2 . Consequently, the analysis of the second harmonic autocorrelation

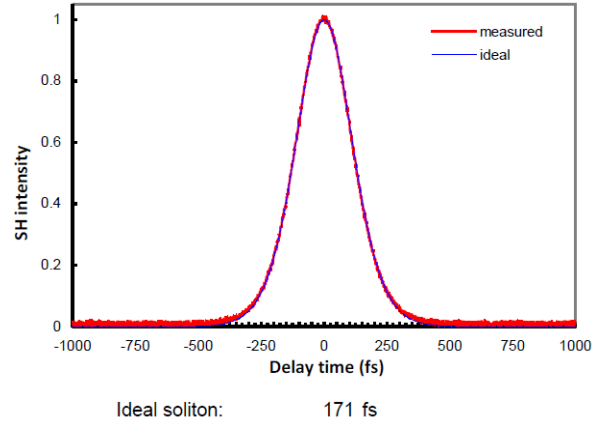


Figure 3.3.2: SH Intensity measured at the output of The low power Yb laser

was performed: in the hypothesis of emission of an ideal soliton, a FWHM of 171 fs was obtained, as we can see from figure 3.3.2.

3.3.2 High Power Pump Diode

The pump designed to amplify the pulse is supplied by a Diode Laser, injected in the WDM through multimode fiber with core/cladding diameter of 105/125 μm .

The high power pump laser is controlled through a current driver (Wavelength Electronics, mod. LDTC 2/2E) also equipped with temperature controller and a heat sink with the purpose to avoid excessive thermal load on the diode.

The maximum power generated at the output of the pump diode is 35 W, even though 10 W were never overcome for our experiment. The performance at the output of the high-power amplifier were characterized in terms of output power vs current, output spectrum, pulse duration, and power stability. Figure 3.3.4 shows the average power of the Yb-fiber amplifier as a function of the current supplied to the pump diode, with heat sink temperature of 25 $^{\circ}\text{C}$. Specifically the power has been measured after the collimator at the output of the double-clad fiber; a long-pass filter with cut-off at 1000 nm has been used to reject the pump light power that is not used during normal operation of the amplifier. The typical operating current of the pump diode for the measurements collected is 2 A, corresponding to an output power of 1.1 W after the collimator, and 0.92 W after the isolator and grating compressor.

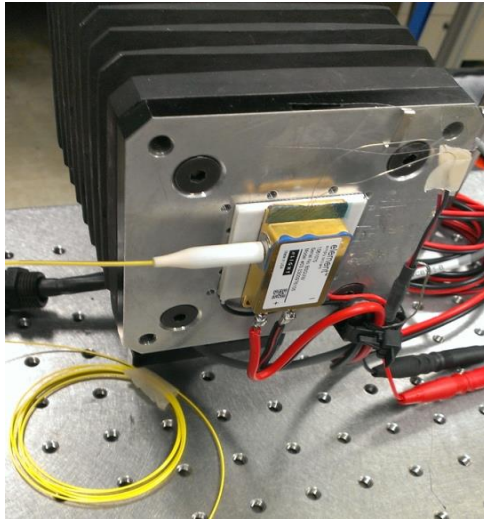


Figure 3.3.3: High-power pump diode at 976 nm with heat sink

3.3.3 Amplification Fibers

The beam at the output of the low-power oscillator is coupled into a HI1060 fiber (length 0.7 m) which is spliced to another HI1060 fiber (length 0.8 m) representing the input fiber of the hybrid WDM device. The hybrid WDM (DKPhotonics, model PSC-21-25-105/125-6/125DC-20/125DC-T3-08) multiplexes the low-power pulse train at 1040 nm (HI1060 fiber with core/cladding diameter of 6/125 μm) and the pump at 976 nm (multimode fiber with core/cladding diameter of 105/125 μm) into an output double-clad fiber of length 0.8 m, core, first cladding and second cladding diameter respectively of 20, 105 and 125 μm .

The double clad fiber propagates the signal at 1040 nm within the core and the pump at 976 nm within the first cladding, ensuring the capability to pump at high power without damage and avoiding excess nonlinearities degrading the signal.

The double-clad fiber at the output of the WDM is spliced to an Yb-doped double-clad fiber of length 2 m (Coractive model DCF-YB-20/128E) having a core numerical aperture of 0.08; amplification take place within the last fiber: the target output power of 0.92 W required to generate the supercontinuum radiation trough the PCF is thus reached.

With the purpose to characterize the pulse at the end of the amplification stage, both the spectrum and the autocorrelation were measured; results are reported respectively in figure 3.3.6 and in figure 3.3.5

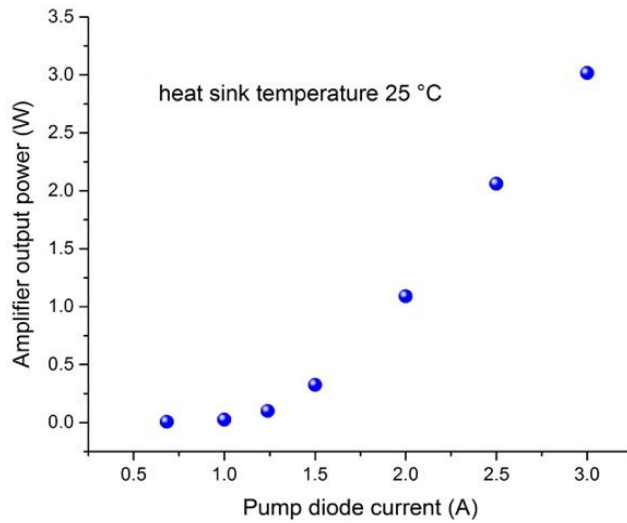


Figure 3.3.4: Output power of the Yb-fiber amplifier as a function of the pump diode current.

3.3.4 Photonic Crystal Fiber

The compressed pulses are coupled into a PCF by a focusing asphere lens (Thorlabs C110TMD-B). The characteristics of the PCF (NKT Photonics, LMA-PM-5 Large-Mode-Area Photonic Crystal Fiber, $5.0 \mu\text{m}$ core, 5 cm length) have been tailored to the power level of around 1 W adopted for the supercontinuum generation.

The adopted PCF is polarization maintaining because this characteristic allows to reduce the depolarization noise, typically observed in PCF, which limits the sensitivity performance of the system by introducing excess amplitude noise and reducing the coherence of the supercontinuum generated by the PCF [38].

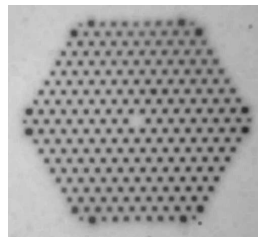


Figure 3.3.7: Photonic Crystal Fiber structure

The PCF has been glued inside a standard angled ceramic ferrule connector (APC connector) for best long term mechanical stability. The coupling into the PCF is obtained by using a high-precision NanoMax translation stage (Thorlabs, MAX313D/M) ensuring long-term alignment. To this concern, it should be noted that the larger core diameter of the PCF adopted here relaxes the requirements on the mechanical stability of the translation stage used for alignment of the focusing lens.

After turning on the Yb-fiber amplifier to the nominal power of 0.92 W, the assembly of PCF and connector requires a 30 min warm-up to reach steady state

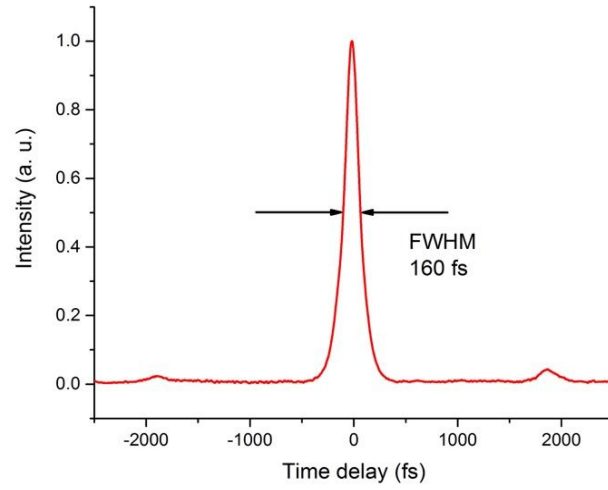


Figure 3.3.5: Autocorrelation trace of the pulses at the output of the Yb amplifier as measured after the grating compressor

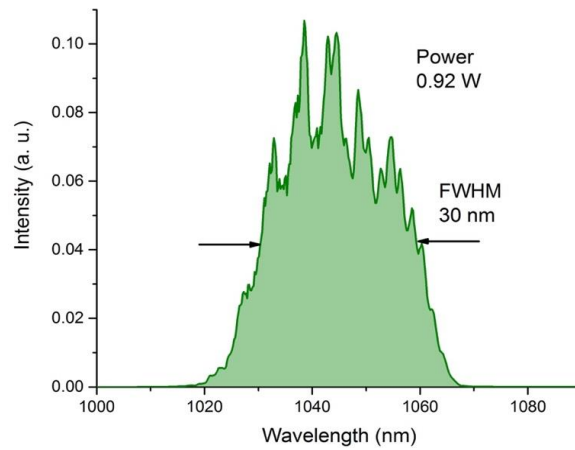


Figure 3.3.6: Spectrum of pulses at the output of the Yb amplifier as measured after the grating compressor

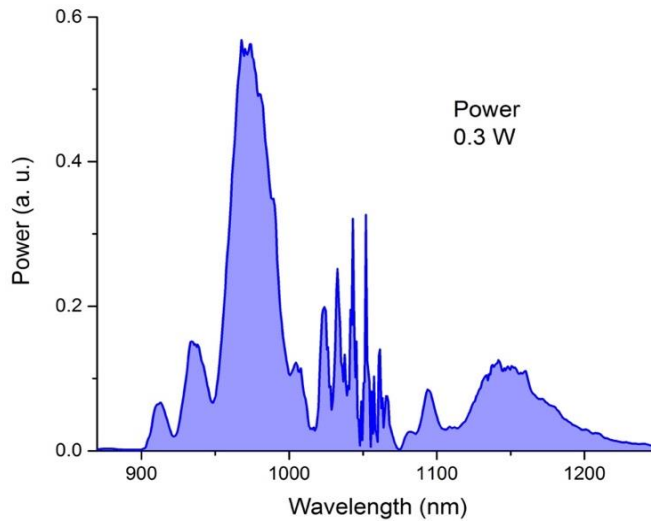


Figure 3.4.1: Spectrum of the supercontinuum at the output of the PCF fiber

deformations induced by the heat load; after this, the system can be operated for hours without any power drift due to thermal effects.

The output of the PCF is collimated by an achromatic lens (Thorlabs AC050-008-B-ML) with a focal length of 7.5 mm.

3.4 Broadband Ultrashort Pulse delivered for FT-CARS

With the purpose to evaluate the suitability of the pulse for the FT-CARS detection, the analysis of the spectral power distribution outgoing from the PCF is led. From figure 3.4.1 The band spanned by the continuum extends from 900 to 1200 nm with a power content of around 300 mW, as required for the detection of a sufficiently wide band of Coherent Anti-Stokes Raman transitions.

The propagation of the pulse through the PCF induces the broadening of its envelope: a prism compressor based on SF10 Brewster prisms has been selected for compensation of the positive GVD introduced. The choice of chirped mirror for pulse compression would have been more accurate since prism compressor are well-known for giving high insertion losses and extended footprint, however this optical element was not available.

By setting the distance between the SF10 prism to 400 mm, the pulses from the PCF fiber have been collapsed to durations in the sub-20 fs regime, according to the autocorrelation trace reported in figure 3.4.2, having a duration of 26 fs. The power of the pulse train at the output of the prism compressor is around 300 mW, still sufficiently high for CARS detection.

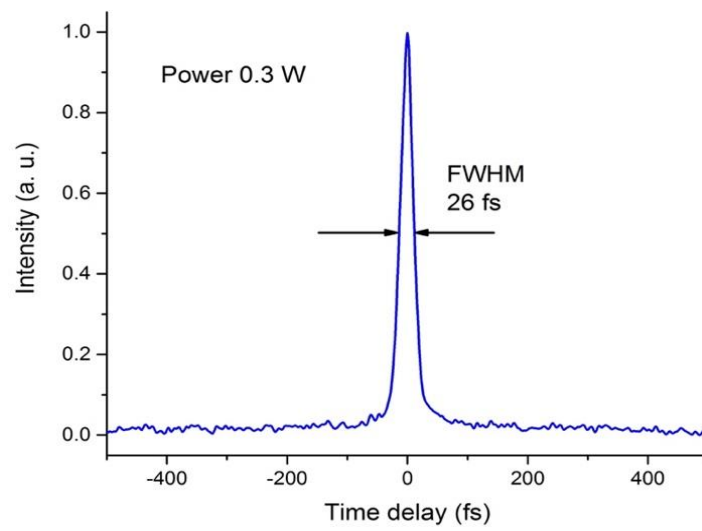


Figure 3.4.2: Autocorrelation trace of the pulses at the output of the SF10 prism pair

Chapter 4

FT-CARS enabled by Michelson Interferometer

As described in Section 2.3.2, Coherent anti-Stokes Raman Spectroscopy (CARS) is a form of optical spectroscopy whereby a pair of pulsed laser beams is irradiated onto a sample and the resultant spectrum of light analyzed. The technique has many similarities to Raman spectroscopy, often employed in chemical agent detection systems, but benefits in its ability to detect chemicals of interest in multi-component mixtures. In our thesis work, the Fourier transform variant of CARS was implemented, enabled by a Michelson interferometer, as showcased in Section 2.3.3. The objective the thesis work was to test a number of solutions of chemical agent simulants to see how sensitive the technique is and its potential as a chemical warfare agents (CWAs) sensor. Developing systems for the detection of CWAs with rapid response, high sensitivity and stability is in fact essential for prevention of terrorist attacks. In particular the detection of droplets of different chemicals was tested both in transmission and back reflection (deposited upon different surfaces: stainless steel and glass). CARS spectra were acquired at a range of different integration times in order to find out the shortest time to acquire a CARS spectrum with acceptable signal-to-noise ratio (SNR) for each chemical/surface combination. In Section 4.1, the different experimental setups we tested will be presented and the electronics will be discussed too, in Section 4.2 the results of our measurements and the relative discussion are reported and in Section 4.3.

4.1 Experimental Setup

In this section the different experimental setups will be presented, considering fs pulses to be obtained as described in Chapter 3.

4.1.1 Transmission Configuration

The first iteration of the experiment was performed in a transmission configuration described by the setup in Fig. 4.1.1.

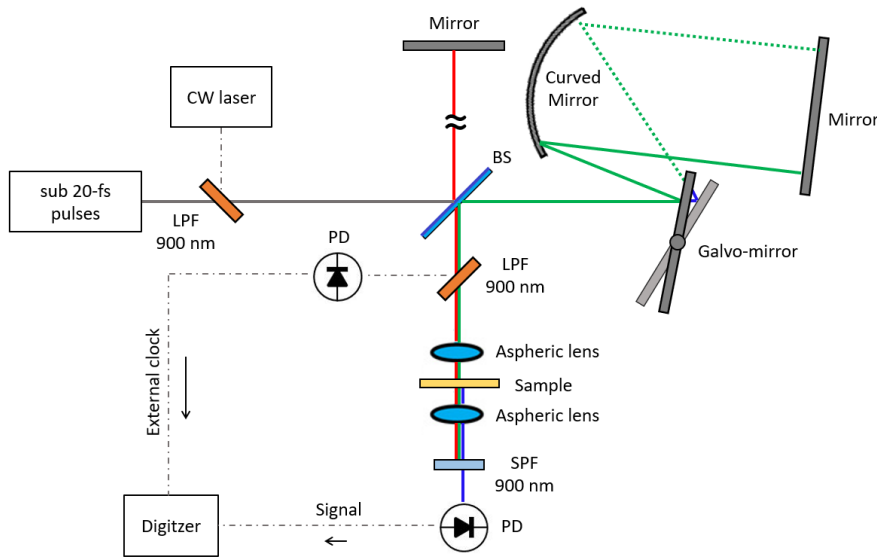


Figure 4.1.1: Schematic of the rapid-scan FT-CARS system.

The short pulse, centered at $\lambda = 1030 \text{ nm}$, propagates through an optical long-pass filter (LPF, cutoff around 900 nm , 11111 cm^{-1}) and then is sent to the input of the Michelson interferometer, together with a Nd-He continuous wave laser beam, which will be used for sampling reasons. After entering the interferometer, the pulse is splitted into two pulses by a 50:50 beam splitter. The two propagates through the two arms of the interferometer: one arm is equipped with a delay line based on a galvo-mirror (GVS001 Thorlabs), whereas the other arm has fixed length, thus a time delay is introduced between the pair of pulses. The two backreflected collinear pulses are then multiplexed on the beamsplitter and propagated toward the output of the interferometer. Here, another optical long-pass filter is placed in order to extract the CW Ne-He beam, which is directed towards a photodiode. The output pulses are focused onto the liquid sample within a cuvette, with a focusing lens of 8-mm focal length. The first pulse excites molecular vibrations via impulsive stimulated Raman scattering while the second probes them. Through the stimulation process, molecular vibrations having oscillation periods longer than the excitation pulse duration can be excited by this single pulse. Thus, the spectral bandwidth of the FT-

CARS is determined by the pulse duration of the excitation pulse. Depending on the delay, the second pulse generates either blue-shifted (anti-Stokes) or red-shifted (Stokes) scattered light due to the refractive index modulation of the sample induced by the first pulse [39]. By scanning the delay, the intensity of the scattered light is modulated at frequencies which reflect those of the molecular vibrations. The generated anti-Stokes beam and the residual comb beams are forward-collected with another lens of 6-*mm* focal length. Afterwards, the beams pass through an optical short-pass filter (SPF, cutoff around 900 *nm*, 11111 *cm*⁻¹) for filtering out the light of the fundamental and extract only the CARS signal, which is then directed to a 10 MHz avalanche photodiode. Then, the signal is digitized using an 12-bit oscilloscope with a sampling rate of 125 MS/s.

A photo of the implemented set up is shown in Fig. 4.1.2 and Fig. 4.1.3.

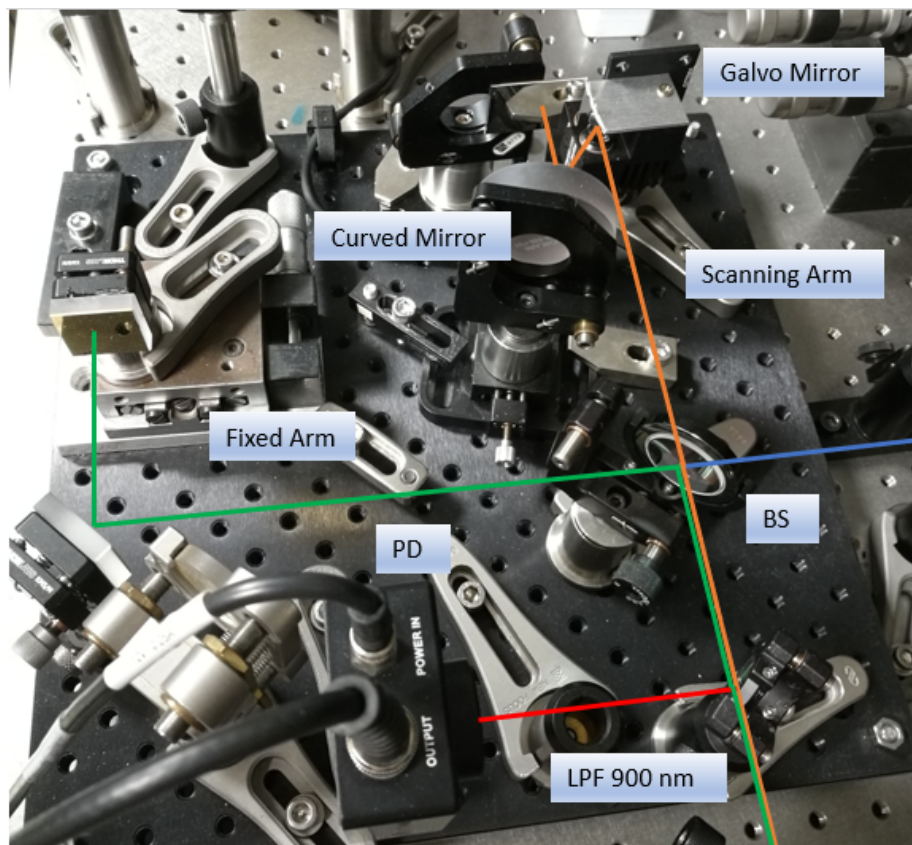


Figure 4.1.2: Photo of the implemented Michelson interferometer.

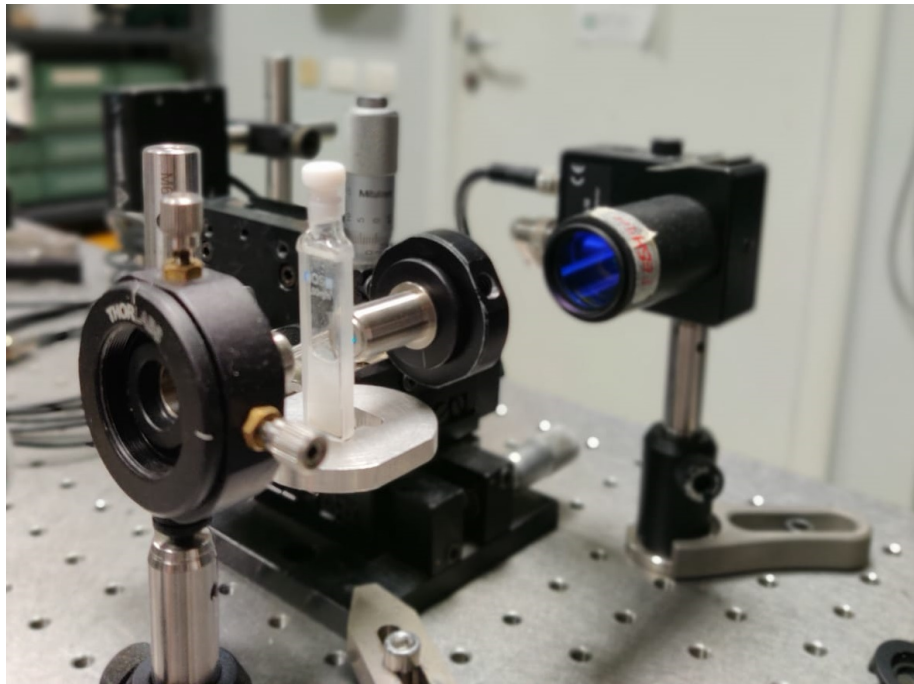


Figure 4.1.3: Photo of the implemented transmission stage.

By detecting the intensity modulation, we observe the molecular vibrations in the time domain. The broadband CARS spectrum can then be retrieved from a Fourier transform of the interferogram. A typical FT-CARS interferogram observed with the setup described here is shown in Fig. 4.1.4. The interferogram is windowed by a rectangular window (no apodization) with a duration of around $100 \mu s$, so that the non-resonant impulsive background at time delay close to zero is totally rejected, and only the part of the interferogram containing the decaying ringing signal due to molecular vibrations is used for Fourier transformation. The dispersion is controlled with a prism compressor based on SF10 Brewster prisms placed before the Michelson interferometer and it is finely regulated observing the CARS interferogram.

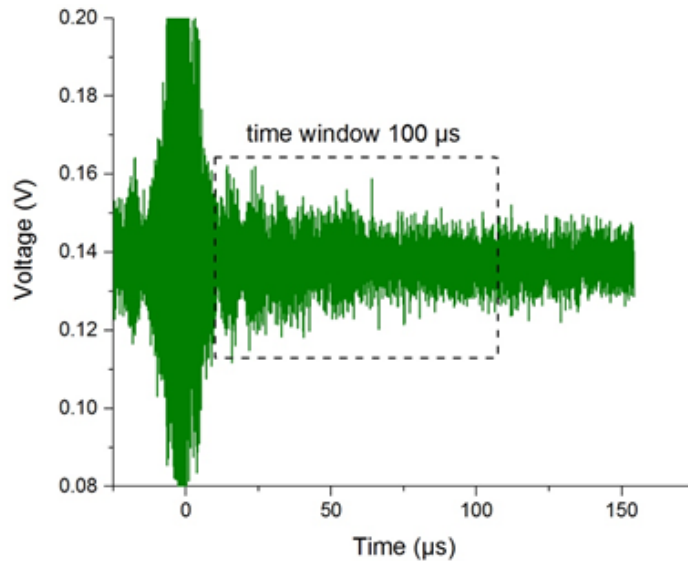


Figure 4.1.4: Interferogram with detail of the time window used for Fourier transform.

Delay line

After separation with the beamsplitter, the pulses travel into a scan- and a reference-arm. The scan-arm is given by a rapid delay scanner that consists of a galvo-mirror, a curved mirror ($f = 50 \text{ mm}$) and a flat mirror aligned in a 4-f geometry as better shown in Fig. 4.1.5. The 4-f configuration allows the returned pulse from the path length scanner to travel back along the same path as the incident pulse except for the time delay produced by the scanner [40]. The angle variation of the resonant scanner in the scan arm is translated into the change in optical-path-length. In this first configuration, we used a non-resonant galvo-mirror, so we were able to pilot it with waveforms of different frequencies and we could also set the amplitude to determine the scanning angle, however the maximum pilot frequency is much smaller than that of a resonant galvo-mirror. The different choices of amplitude and speed of the galvo-mirror trajectory will be specified in Section 4.2.

Depending on the waveform that pilots the galvo-mirror, the delay scanner increases the delay non-linearly in time; it is thus necessary to make a time-grid correction on the CARS interferogram. For this purpose, we use interference signals (CW interferograms) of a collinearly introduced He-Ne laser to the pulsed laser as an external clock for digitizing the CARS interferograms. Greater details about the sampling process will be given in Section 4.3.

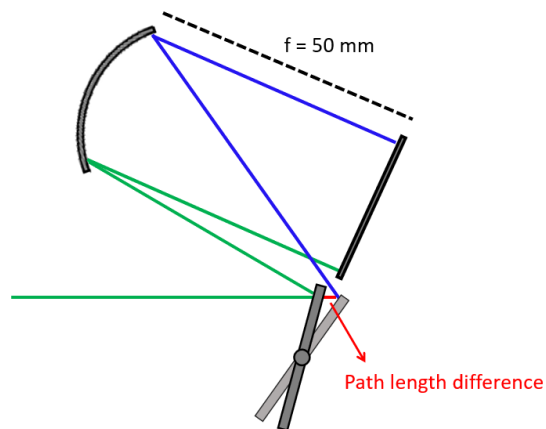


Figure 4.1.5: Scan-arm in 4-f configuration.

4.1.2 Back-reflection configuration

The configuration presented in the previous section was later modified to be used in a back-reflection configuration: the goal was to demonstrate the capability of the technique to detect chemicals deposited on different surfaces. The modified configuration is shown in Fig. 4.1.6.

The setup is very similar to its transmission counterpart; the only difference is that once the pulses are focused on the sample by the lens of 8-mm focal length, the generated CARS signal and the fundamental get to the surface where the sample is deposited and they are reflected back and collected by the same lens. From here, they travel back to the LPF which then extracts the CARS signal and directs it onto the avalanche photodiode.

Back-reflection segment

Even though the two configurations are similar, the back-reflection set up requires some additional attentions, in particular, the distance of the sample from the focusing lens needs to be carefully determined as shown in Fig. 4.1.7.

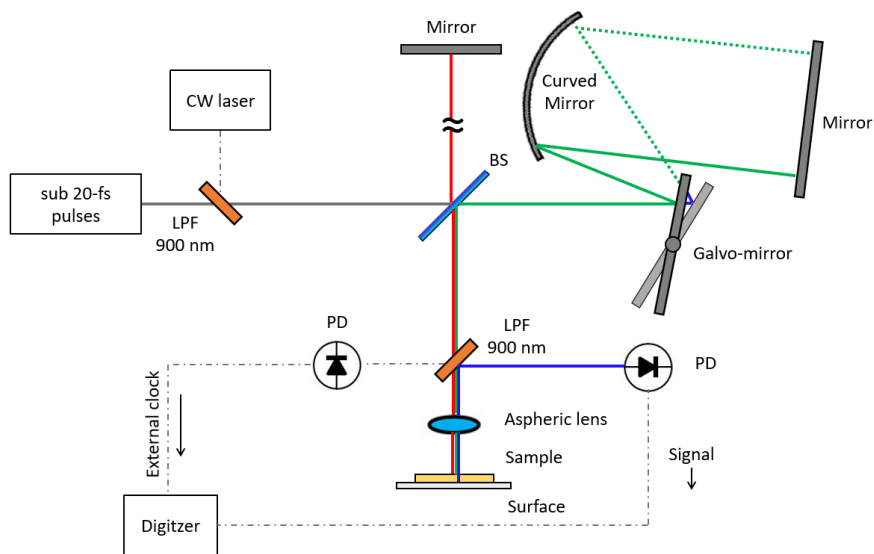


Figure 4.1.6: Schematic of the rapid-scan FT-CARS system in back-reflection configuration.

As the laser beam is focused onto the sample, a strong forward-CARS and a much weaker epi-CARS signal is generated. The epi-CARS signal has a power level below the sensitivity of the avalanche photodiode used for detection, and do not contribute to the measurement. Indeed, epi-CARS signal is expected to have power level similar to the forward generated CARS only if the sample under investigation is a highly scattering medium as in the case of biological samples. However, the samples characterized within this project are highly transparent liquid samples with negligible amount of scattering. For this reason, detecting CARS with transparent liquid samples in back-scattering configuration has always been considered to be very difficult (and even not feasible) by the research community working on CARS spectroscopy. As one can notice however, the strong forward-generated CARS beam reaches the interface between the sample and substrate and is back-scattered or back-reflected, depending on the substrate, with relatively high power levels, so that detection is possible by high-sensitivity detectors such as avalanche or photomultiplier detectors; this is why one should focus the incoming beam in the sample, as near as possible to the surface. It should be noted that the type and settings (resolution, sensitivity, ...) of the instruments adopted in the various databases are not homogeneous, this is why is highly recommended to measure the CARS spectra of interest by using the system operating in transmission mode, before modifying the system for operation in reflection mode, in order to get specific prior knowledge of the target CARS spectra of samples. Prior measurement of the CARS spectra in transmission mode provided a first feedback on the strength and spectral profile of the CARS response of the chemicals of interest, and generally more experimental confidence in view of the change to operation in reflection mode. As a first step in fact, a silver mirror will be just placed after the quartz cuvette, very close to the output surface of cuvette, to back-reflect the CARS signal that is usually collected in transmission mode. This CARS beam will be used to align

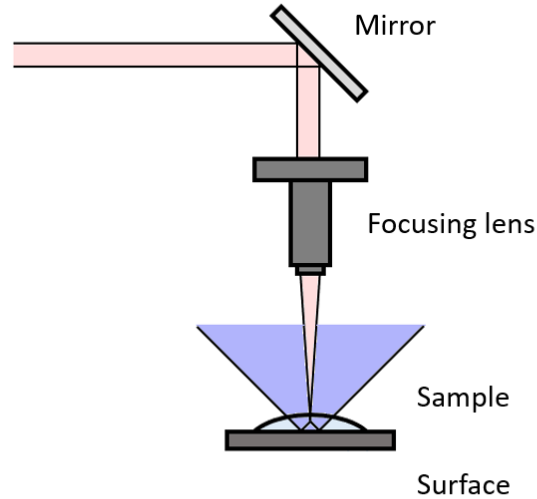


Figure 4.1.7: Back-reflection segment.

and optimize the detection unit for following detection of back-scattered CARS radiation.

4.1.3 Transmission Configuration with a Resonant Galvo-Mirror

The previous version of the system was mainly limited by the rotation speed of the non-resonant galvo-mirror of the interferometer and the dead-time between adjacent interferograms. The physical limit to the measurement is represented by the Raman relaxation oscillations with duration of around $100 \mu\text{s}$, corresponding to an acquisition rate of 104 spectra/s (10 kHz). The last configuration we tested is thus the same transmission setup as before, but with a resonant galvo-mirror (CRS4kHz by Cambridge Technology). Since it is a resonant device, it can be piloted only with a sine wave at the resonant frequency, in our case 4 kHz. This modified design will avoid the dead time between adjacent interferograms, reducing the measurement time close to the theoretical limit. Without this re-design, the performance in terms of minimum integration time required will be far from the ultimate performance achievable by the system.

Since in this case a sine wave is used, the delay is increased non-linearly, thus in this configuration the time-grid correction on the CARS interferogram will be completely necessary. So, the use of the interference signals of the He-Ne laser are fully exploited in this case. Again, greater details about the results obtained and about the sampling will be presented in Sections 4.2 and 4.3 respectively.

A photo of the set up in this last implementation is shown in Fig. 4.1.8.

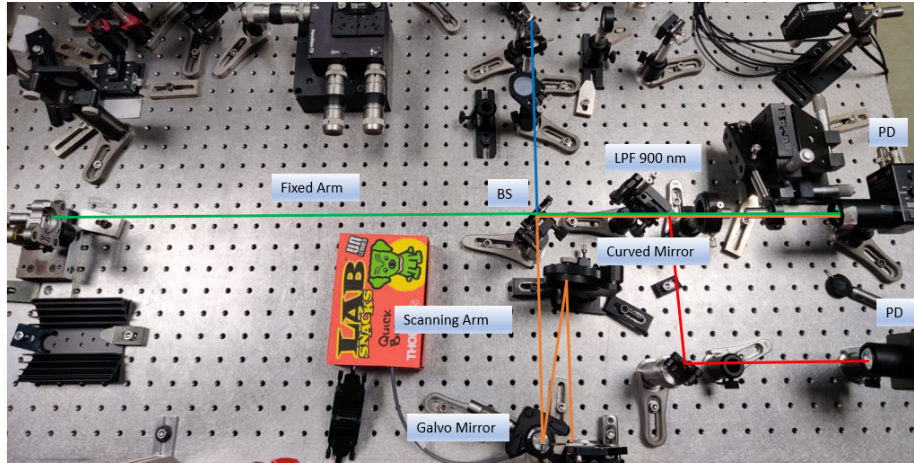


Figure 4.1.8: Photo of the implemented set up.

4.1.4 Electronics

As discussed previously, in the implementation of the scanning arm of the Michelson interferometer, two different galvo-mirrors were used: a non-resonant one (GVS001 Thorlabs) and a resonant one (CRS4kHz by Cambridge Technology). Pictures of the two devices are reported in Fig. 4.1.9 [3] and Fig. 4.1.10 [4].

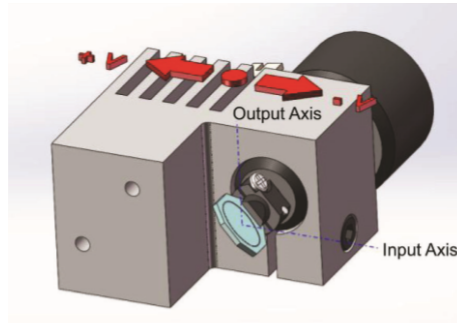


Figure 4.1.9: Non resonant galvo-mirror [3].



Figure 4.1.10: Resonant galvo-mirror [4].

Non-Resonant Galvo-Mirror

In order to use this device one has to proceed with some electrical connections. In Fig. 4.1.11 [3] an image of the the driver board is shown.

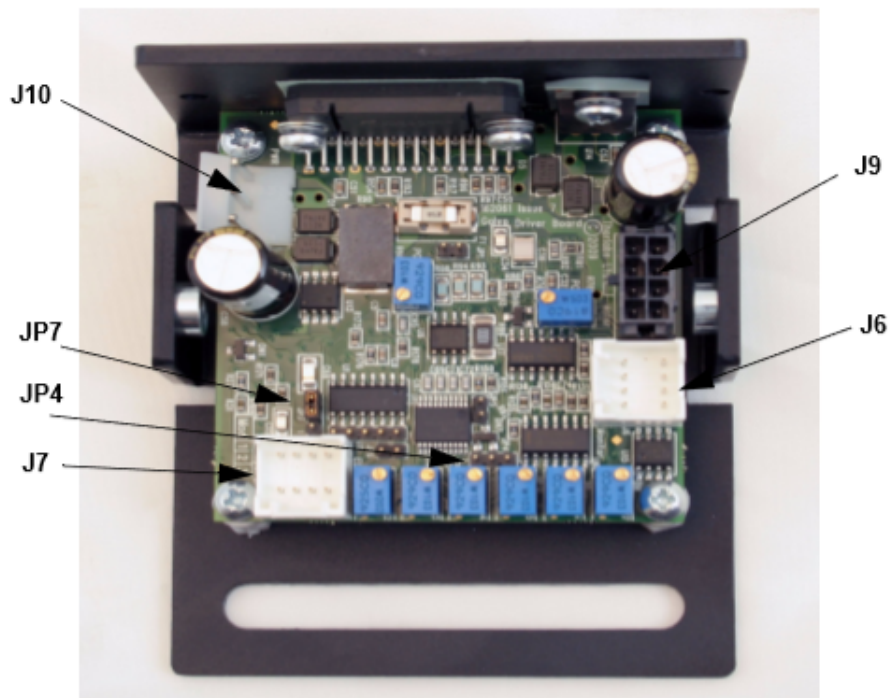


Figure 4.1.11: Driver board of GVS001 Thorlabs [3].

Connector J10 is used to power up the driver through a linear power supply while connector J9 instead is used to connect the driver to the motor of the galvo-mirror. Connector J7 is the command input connector and the pin identification is shown in Fig. 4.1.12 [3].

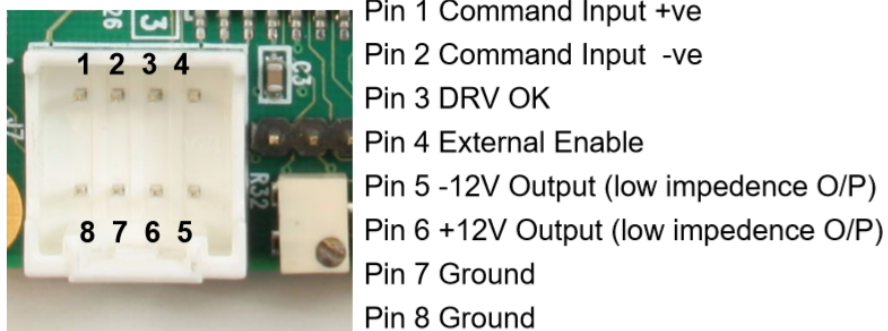


Figure 4.1.12: Command input connector pin identification [3].

The scanner accepts a differential analog command input between -10 V and 10 V. The selected scaling was 0.8 V per degree mechanical movement, giving -12.5 to +12.5 degrees maximum mechanical movement. To give the command input to the driver the wave generator Siglent SDG 5162 reported in Fig. 4.1.13 was used. The same device is used to provide the trigger signal to the oscilloscope used to observe the interferogram.



Figure 4.1.13: Siglent SDG 5162 wave generator.

Resonant Galvo-Mirror

The driver board for the resonant galvo mirror is shown in Fig. 4.1.14.

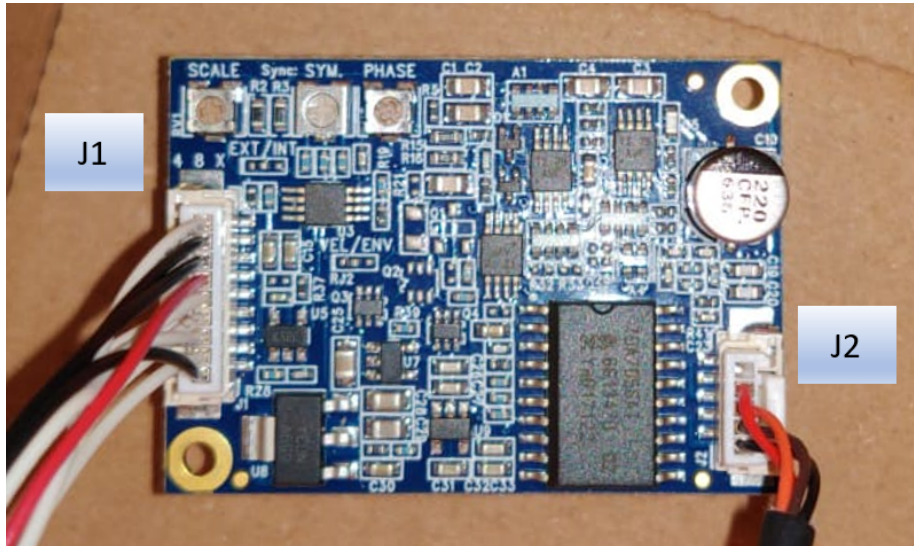


Figure 4.1.14: Driver board of CRS4Hz Cambridge Technology.

Connector J2 powers up the galvo-mirror itself, while connector J1 is related both to the power supply of the driver and the command input. The identification of the pin of connector J1 is reported in Fig. 4.1.15 [4].

Pin	Signal	Comments
1	GND	
2	Velocity	Unscaled; for safety verification only
3	Sync	At each change in direction
4	Fault	Not in regulation
5	Disable	Pull down to disable servo
6	Power	12V DC
7	GND	
8	GND	
9	Ext. Amplitude Control	0-5V DC for zero to full scan angle

Figure 4.1.15: Pin identification of connector J2 [4].

One can see that it is possible to pilot the driver with a voltage 0-5 V, with a maximum angle of 26 degrees. The sync signal is at each change of direction and it is given to the oscilloscope as an input.

4.2 Results and Discussion

4.2.1 Transmission Configuration

First of all we developed the system in the configuration shown in Fig. 4.1.1, i.e. a transmission configuration using a non-resonant galvo-mirror along the delay line. At this stage, the goal was actually to test the goodness of the experimental setup and to gain the experimental knowledge required to later pass to the reflection configuration. To do so, first of all we measured the spectrum of a liquid sample of acetonitrile, which has a rather intense Raman spectrum.

As described in Chapter 3, the generated continuum has a spectral range of 900-1200 nm ($11111\text{-}8333\text{ cm}^{-1}$) and thanks to compression by the prism pair, the pulse duration at the sample is shorter than 20 fs with a power of ≈ 400 mW.

A ramp signal is used to pilot the non-resonant galvo-mirror, in particular we set an amplitude of 4 V (8 V peak to peak), corresponding to a rotation angle $\theta = 20^\circ$. This angle corresponds to a maximum optical-path-length difference between the arms of $\approx 0.9\text{ mm}$, corresponding to the spectral resolution of $\approx 11\text{ cm}^{-1}$. The chosen frequency is 100 Hz.

In order to align the configuration and set the right amount of compression, we first measured the anti-Stokes Raman spectrum generated by the acetonitrile sample, using a spectrometer. The result is shown in Fig. 4.2.1.

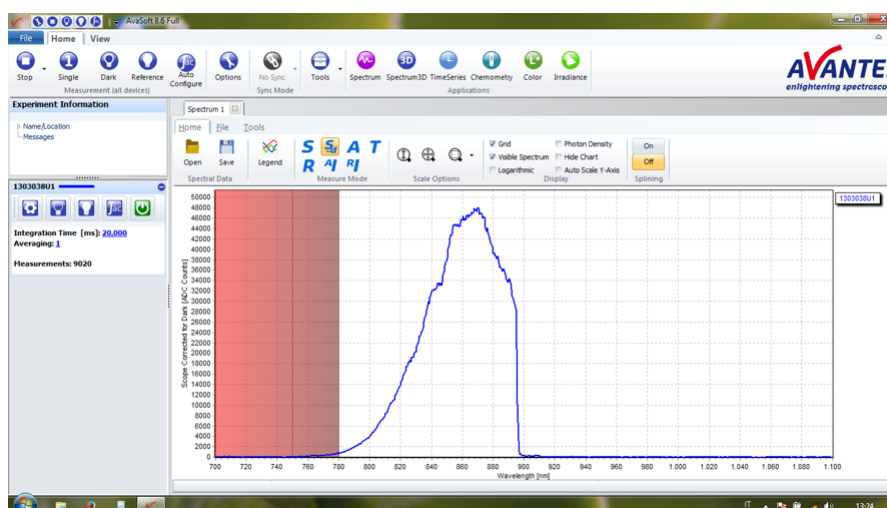


Figure 4.2.1: CARS spectrum generated by an acetonitrile sample.

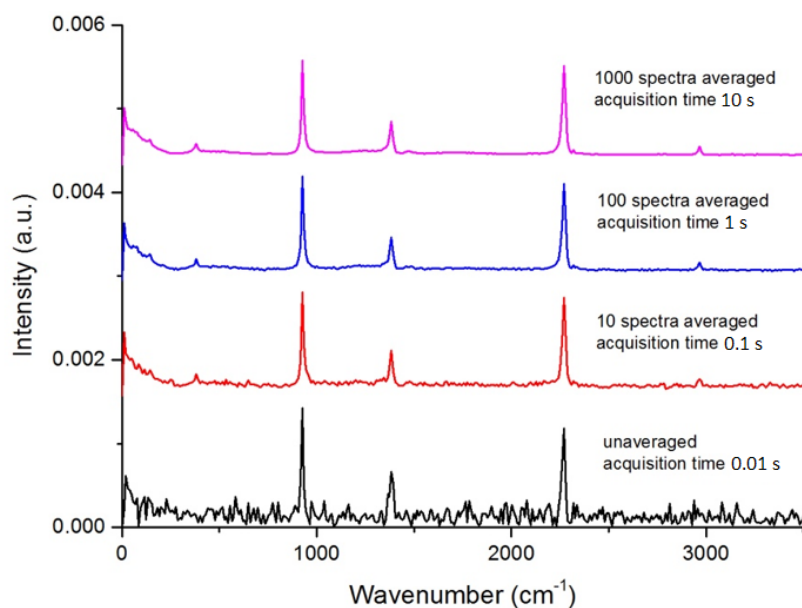


Figure 4.2.2: Raman spectra of acetonitrile as observed by Fourier transform of one interferogram (no averaging, black line), and 10 (red line), 100 (blue line), 1000 (pink line) averaged interferograms.

One can see that the CARS spectrum extends from 750 nm (13333 cm^{-1}) to 900 nm (11111 cm^{-1}), corresponding to a Raman frequency span of 2200 cm^{-1} .

The generated CARS signal is then detected by an avalanche photodiode and digitized. The measured interferogram was shown in Fig. 4.1.4. Rejecting the non-resonant impulsive background and performing the Fourier transform of the decaying ringing signal related to molecular vibrations, we obtained the Raman spectrum of acetonitrile, as shown in Fig. 4.2.2. As one can see, different CARS spectra are presented: without averaging (black line), and when averaging over 10, 100, or 1000 consecutive spectra (red, blue, and pink line, respectively). The Raman resonance of cyanide can be clearly seen at 2250 cm^{-1} in all cases. The signal to noise ratio (SNR) of the spectrum obtained with 1000 averages is ≈ 870 (defined as the ratio of the intensity of the strongest Raman line and the standard deviation of the noise in the Raman shift range where no lines are present).

After this first successful test using acetonitrile, we passed to the actual contaminants of interest, in particular, the contaminants we tested are:

- dimethyl methylphosphonate (DMMP) (CAS # 756-79-6);
- tris(2-ethylhexyl) phosphate (TEHP) (CAS # 78-42-2);
- thiodiglycol (TDG) (CAS # 111-48-8).

The choice of these substances is driven by the fact that they represent simulants of dangerous CWAs. In particular, DMMP has a chemical structure similar (but with a much lower toxicity) to nerve agent sarin (2-(fluoro-methyl-phosphoryl)oxypropane) [41], one of the most toxic warfare agents. TEHP instead is a simulant of the nerve agent VX [42], while TDG is a simulant of sulfur mustard, commonly known as mustard gas [43].

Representative Raman spectra of these simulants have been found in literature and various publicly accessible databases (NIST databases), and are reported in Figures 4.2.3, 4.2.4 and 4.2.5 [5]; one can see the relevant Raman features are located in the spectral range extending from 0 to 1800 cm^{-1} .

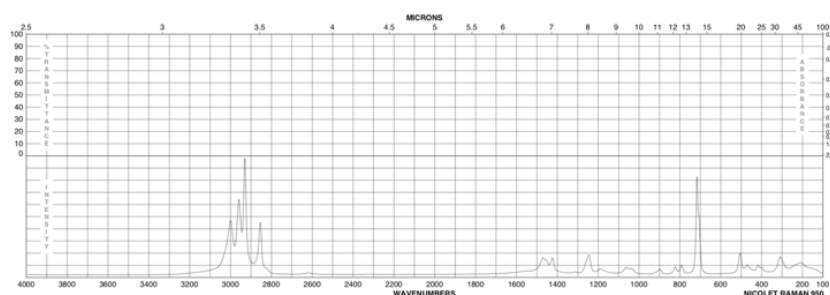


Figure 4.2.3: Raman spectrum of dimethyl methylphosphonate (DMMP) (CAS number 756-79-6) [5].

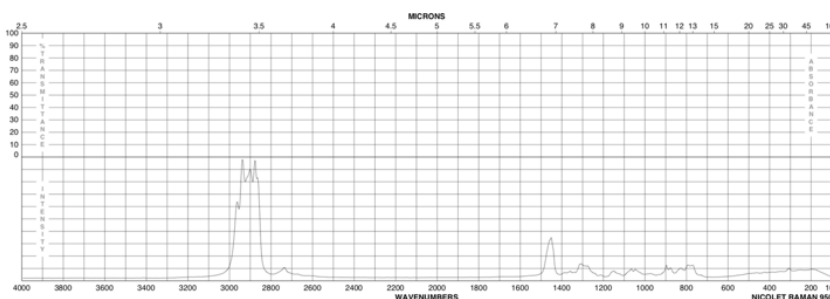


Figure 4.2.4: Raman spectrum of tris(2-ethylhexyl) phosphate (TEHP) (CAS number 78-42-2) [5].

The observable Raman band enabled by the system should be tailored to the CARS spectra of the CWAs simulants specified. In particular, the current observable Raman band is way larger than that required by the CWAs simulants, yielding to inefficient CARS excitation, as a considerable amount of pump power is distributed at frequencies where the samples do not exhibit any Raman vibration, and hence is basically lost. According to the Raman spectra reported in Figures 4.2.3, 4.2.4 and 4.2.5, the CWAs simulants of interest are characterized by weak Raman responses, and thus it is important to improve and optimize the efficiency of the excitation process by reducing the band of the pump laser, i.e.

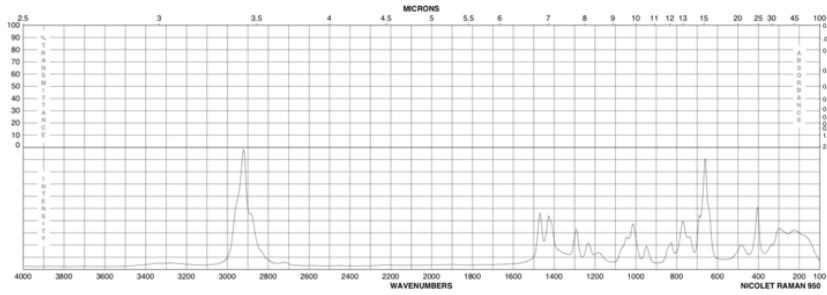


Figure 4.2.5: Raman spectrum of Thiodiglycol (TDG) (CAS number 111-48-8) [5].

concentrating more power in the Raman band of interest. This band tuning can be done by reducing the length of the PCF fiber adopted for spectral broadening after amplification inside the Yb-fiber amplifier. The present PCF fiber has a length of 50 mm , yielding a supercontinuum radiation covering the spectral range from $900\text{ to }1200\text{ nm}$; as the spectral range required in this case is $950\text{--}1150\text{ nm}$, it is expected that a fiber length of around 30 mm would probably be more appropriate for this purpose and thus represents room for improvement of the configuration.

We set the parameters of the system as discussed before ($\theta = 20^\circ$, $f = 100\text{ Hz}$) and we considered DMMP first, since between the chemicals of interest, it is the best Raman scatterer, with a cross-section for Raman excitation comparable to that observed with acetonitrile.

Fig. 4.2.6 shows the CARS spectra of DMMP corresponding to a single spectrum (Fourier Transform of a single interferogram) and to the average of 10, 100 and 1000 spectra. As the interferograms are acquired with a frequency of 100 Hz , the measurement times with averaging of 10, 100, 1000 spectra corresponds to 0.1, 1, and 10 s, respectively. Table 4.1 reports the observed SNR as a function of the number of spectral averages. All measured spectra are of very high-quality, due to effective strength of DMMP for CARS spectroscopy.

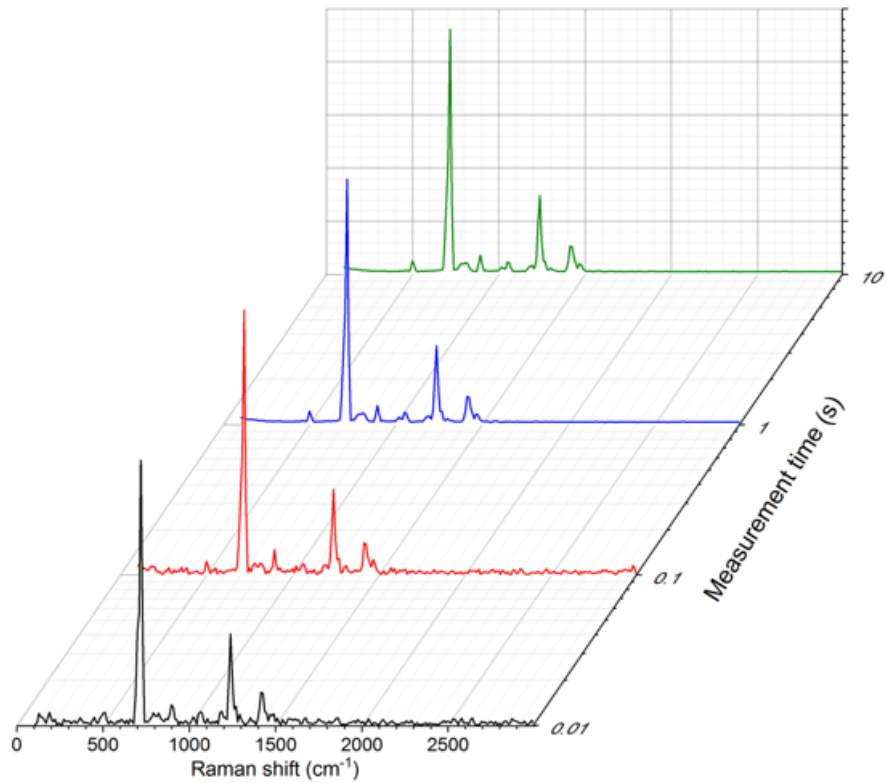


Figure 4.2.6: CARS spectra of DMMP as measured with a single acquisition (black line) and by the average of 10 (red line), 100 (blue line), 1000 (green line) spectra.

Table 4.1: SNR of DMMP strongest Raman line as a function of spectral averaging.

Averaging	1	10	100	1000
SNR	172	712	2350	6250

Fig. 4.2.7 shows the CARS spectrum of DMMP as measured by averaging over 1000 spectra (top red line) and the Spontaneous Raman spectrum of DMMP [5] as measured using a commercial Raman spectrometer (bottom blue line). The inset reports the Raman shifts and relative intensity of the main Raman lines observed.

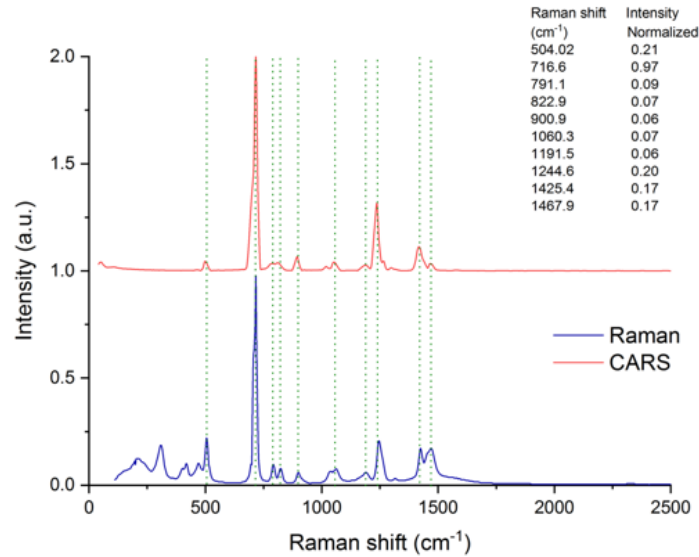


Figure 4.2.7: CARS spectrum of DMMP as measured by the average of 1000 spectra (red line), and spontaneous Raman spectrum (blue line) as measured with a commercial Nicolet Raman 950 [5].

The Raman shift of the main Raman lines are precisely identified: this is a very important aspect in view of an implementation of a software-based system for identification of CWAs by technique such as Principal Component Analysis and Partial Least Squares regression (PCA and PLS). It is worth noting that the reduced amplitude of the peaks at lower Raman shifts with respect to the reference spectrum is intrinsic to the detection technique: only a small part of the low-frequency anti-Stokes power can pass the LPF and contribute to the detection. The range from 1000 to 2000 cm^{-1} is typically favored due to distribution of excitation power in the incident laser light. Generally, spontaneous Raman and coherent Raman spectra such as CARS have slightly different shapes due to the various excitation schemes involved. Moreover, spontaneous Raman is typically excited by a single-frequency pump laser, whereas the CARS technique adopted here belongs to the general class of broadband coherent Raman, where the intensity of a certain Raman feature is due to the additive effect of all spectral components in the pump radiation participating to excitation at the Raman shift of interest.

Next we considered TDG: as opposite with DMMP, TDG is well known to be a very weak Raman scatterer, having a very low Raman cross-section. Fig. 4.2.8 shows the CARS spectra of TDG corresponding to a single spectrum (Fourier Transform of a single interferogram) and to the average of 10, 100, and 1000 spectra. Table 4.2 reports the observed SNR as a function of the number of spectral averages.

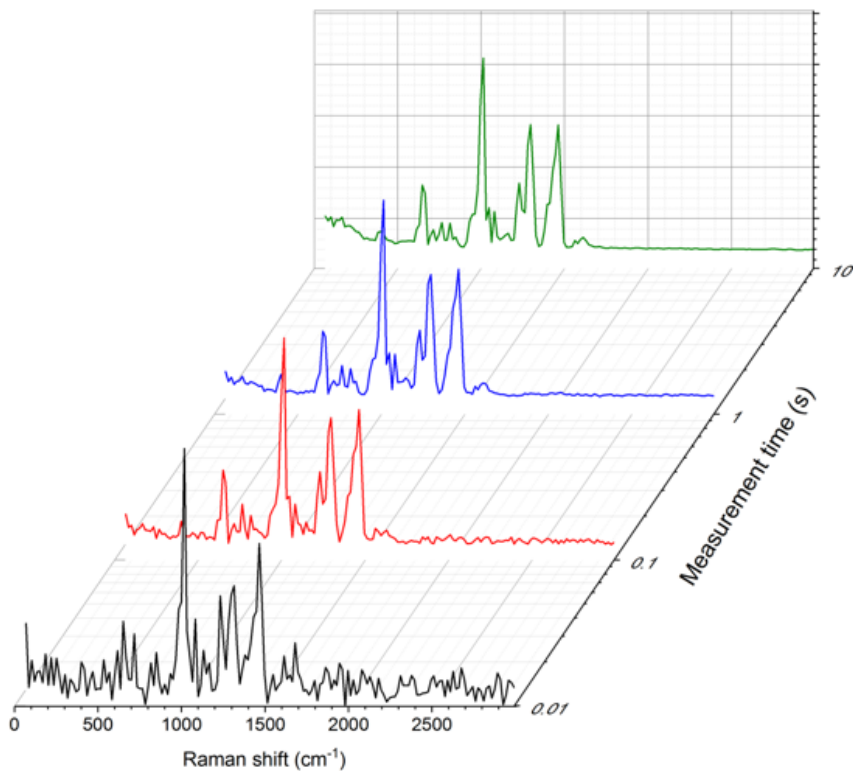


Figure 4.2.8: CARS spectra of TDG as measured with a single acquisition (black line) and by the average of 10 (red line), 100 (blue line), 1000 (green line) spectra.

Table 4.2: SNR of TDG strongest Raman line as a function of spectral averaging.

Averaging	1	10	100	1000
SNR	23	90	316	540

The fact that TDG is a weak scatterer can be easily seen by comparing the SNRs obtained with those of DMMP. As a test of this feature, a 50:50 solution by volume of TDG and acetonitrile has been analyzed. The resulting CARS spectrum is shown in Fig. 4.2.9. As it can be seen, the intensity ratio of the main peak of TDG at 1013 cm^{-1} and acetonitrile at 918 cm^{-1} is around 0.15, meaning that the SNR observed with TDG is correspondingly reduced with respect to acetonitrile.

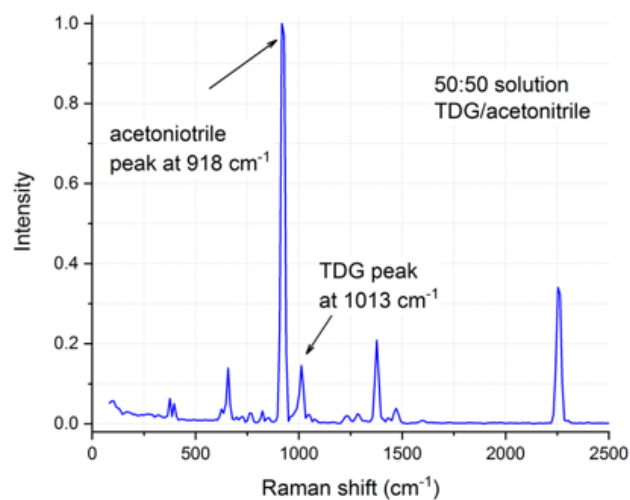


Figure 4.2.9: CARS spectrum of a 50:50 solution by volume of TDG and acetonitrile.

Figure 4.2.10 shows the CARS spectrum of TDG as measured by averaging over 1000 spectra (top red line) and the Spontaneous Raman spectrum of TDG [5] as measured using a commercial Raman spectrometer (bottom blue line). The inset reports the Raman shifts and relative intensity of the main Raman lines observed.

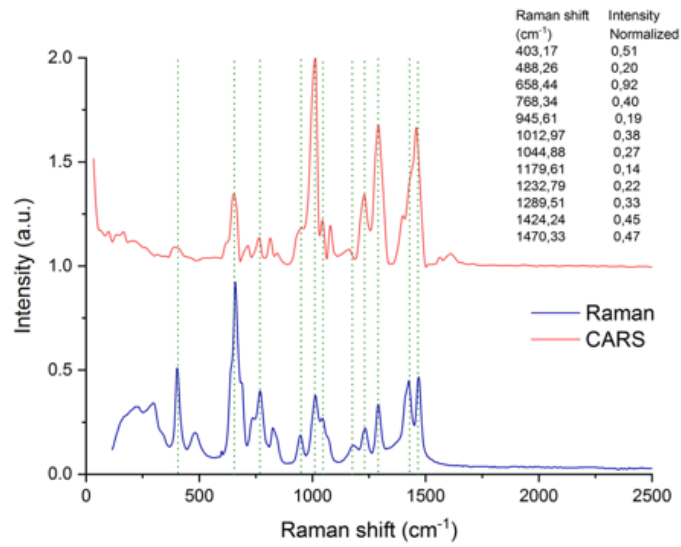


Figure 4.2.10: CARS spectrum of TDG as measured by the average of 1000 spectra (red line), and spontaneous Raman spectrum (blue line) as measured with a commercial Nicolet Raman 950 [5].

To conclude, we considered TEHP: as common to TDG, it should be noted that TEHP is also a weak Raman scatterer.

Fig. 4.2.11 shows the CARS spectra of TEHP corresponding to a single spectrum (Fourier Transform of a single interferogram) and to the average of 10, 100, and 1000 spectra. Table 4.3 reports the observed SNR as a function of the number of spectral averages.

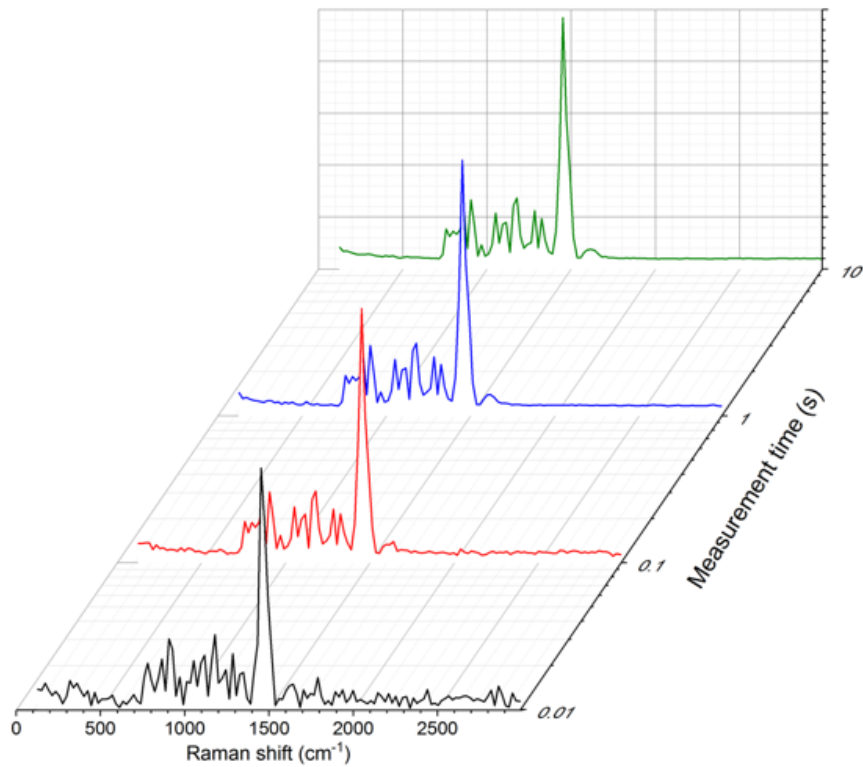


Figure 4.2.11: CARS spectra of TEHP as measured with a single acquisition (black line) and by the average of 10 (red line), 100 (blue line), 1000 (green line) spectra.

Table 4.3: SNR of TEHP strongest Raman line as a function of spectral averaging.

Averaging	1	10	100	1000
SNR	22	80	250	650

Fig. 4.2.12 shows the CARS spectrum of TEHP as measured by averaging over 1000 spectra (top red line) and the Spontaneous Raman spectrum of TEHP [5] as measured using a commercial Raman spectrometer (bottom blue line). The inset reports the Raman shifts and relative intensity of the main Raman lines observed.

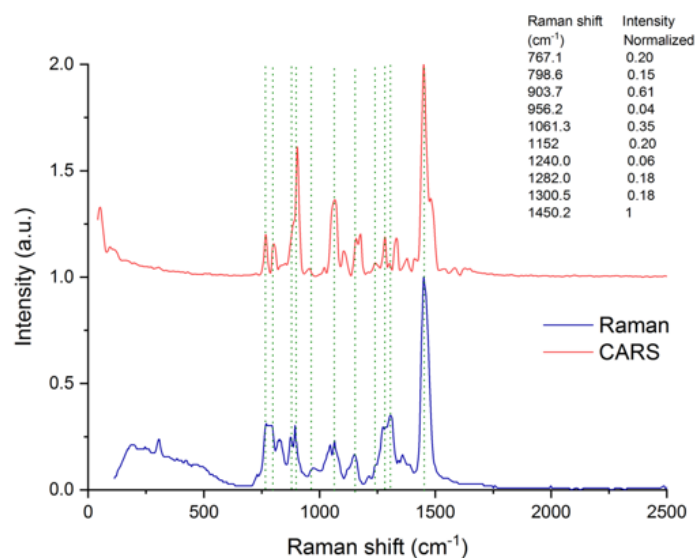


Figure 4.2.12: CARS spectrum of TEHP as measured by the average of 1000 spectra (red line), and spontaneous Raman spectrum (blue line) as measured with a commercial Nicolet Raman 950 [5].

By considering the results obtained, it should be expected that DMMP will be the most favorable CWA simulant when switching to a back-scattering detection setup. On the other hand, the observation of TDG and TEHP under unfavorable conditions such as back-scattering CARS will be more challenging. As DMMP shows strong CARS excitation cross-section, the back-scattering configuration has been developed using DMMP as the target as will be discussed in the following. Once the performance of the back-scattering detection system have been optimized, TDG and TEHP will be used to test the performance of the system under conditions of very low CARS level.

4.2.2 Back-reflection Configuration

After testing the setup in transmission, we passed to the back-reflection configuration described in Fig. 4.1.6. The parameters of the system remained unchanged ($\theta = 20^\circ$, $f = 100$ Hz), but now the generated CARS signal is collected after back-reflection by a certain surface.

The amount of CWAs we considered are within the droplet volume range 1 – 20 μL . Droplet volume are calibrated using precision micro pipette with resolution of 0.1 μL . The starting configuration for the evaluation of the performance of the system was based on depositing a 1 μL droplet of substance onto a proper surface and detecting the back-scattered CARS signal. It is important to keep in mind that the actual amount of substance probed by the laser beam is orders of magnitude lower than the amount of deposited substance, in particular, only the volume over which the laser is focused is probed. This provides an additional degree of freedom on the focused beam diameter adopted for detection, that could be eventually tailored to the purpose of increasing the sensitivity of the system.

The rationale of the experiment is as follows. The power of the laser beam adopted is initially reduced to a proper level in order to avoid the ablation of the droplet under investigation; after this, the additional degree of freedom provided by the beam's focus diameter is used to tune the performance of the system when probing larger sample volume up to the minimum amount of 1 μL . The focused beam diameter will be increased to probe a droplet of 1 μL ; as a consequence of increasing the beam diameter on the sample, a reduction of the intensity at the focus is observed: the consequent loss of CARS signal is compensated by increasing the power level.

At the power level, ≈ 400 mW, there is no observable damage (ablation) induced onto the surface of the substrate by the high laser intensities at the beam focus, however, there is evidence of point sample evaporation, that could be reduced by attenuating the laser power to a level of around 50 mW. Sample evaporation is not due to direct absorption by the sample, which is negligible at the pump laser wavelength of 1030 nm, but more likely to heating of the substrate, especially in the case of the stainless-steel sample, which in turns causes heating of the sample and hence evaporation. Sample evaporation can be avoided by putting a cover glass onto the liquid sample deposited on the substrate with a 1-mm thick chamber on the inner side filled by the sample; once placed, there is no evidence of sample evaporation, at least within the time scale of the experiment. All the results presented in the following have been obtained at the maximum power of 400 mW available at the sample with the cover glass chamber placed onto it to avoid evaporation. This allows for clear identification of the sample and estimation of the SNR under well reproducible conditions. Reducing the power incident onto the sample to around 50 mW leads to reduction of the SNR (CARS signal has cubic scaling law as a function of excitation power) so that the CARS spectra of the sample could not be clearly recognized.

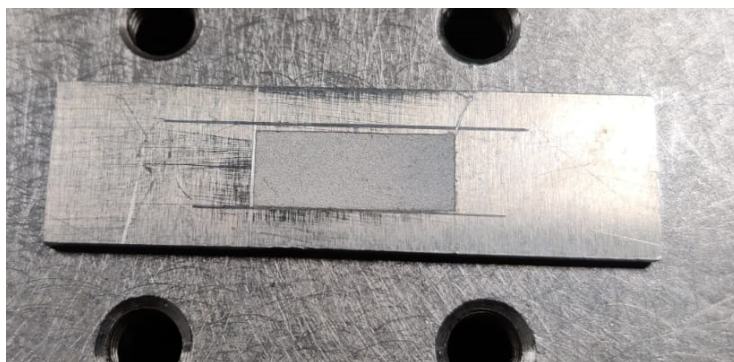


Figure 4.2.13: Stainless-steel substrate.

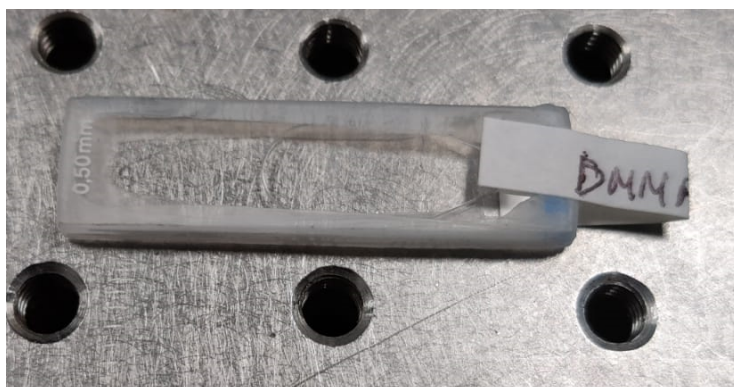


Figure 4.2.14: Glass substrate.

Two different substrates have been used for experiments: a stainless-steel a microscope fused silica slide. The images of the two substrates are reported in Fig. 4.2.13 and Fig. 4.2.14.

As discussed previously, we are considering droplet of chemicals in the range of 1-20 μL , however, the sample volume probed is intrinsically limited by the dimension of the laser beam focus on the sample, thus the probed volumes are much lower than 1 μL . In particular, the laser beam is focused to a radius of around $2.5 \mu\text{m}$, corresponding to an effective area of $0.5 \times \pi \times (2.5 \mu\text{m}) \times 2 = 10 \mu\text{m}^2$. The Rayleigh range corresponding to this laser beam focus is $z_R = 20 \mu\text{m}$. Multiplying by 2 the Rayleigh range, one obtains the measure of the distance over which the beam can be assumed of nearly constant radius, i.e. the depth of focus. The sample's volume probed by the laser beam focus is nearly equal to the effective area multiplied by the depth of focus, that is $10 \mu\text{m}^2 \times 40 \mu\text{m} = 4 \times 10^{-16} \text{m}^3$. Thus, since 1 μL of liquid substance corresponds to a volume 10^{-9}m^3 , the volume probed by the configuration is 7 orders of magnitude lower.

We considered first the stainless steel substrate since we expected it to be a more favorable case with respect to glass. It is worth noting that, in this case, the detected CARS signal is due to scattering from the gritted surface

(no polishing) of the stainless-steel substrate which is collected by the focusing lens. Fig. 4.2.15 shows the epi-CARS spectrum of DMMP deposited on stainless steel substrate as measured with integration times of 0.01, 0.1, 1, and 10 s, corresponding to 1, 10, 100 and 1000 averaged spectra respectively. Table 4.4 shows the corresponding SNRs.

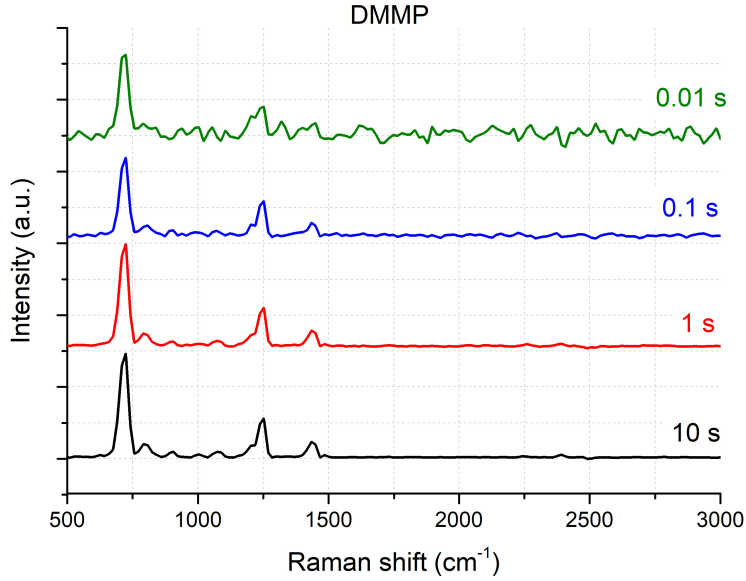


Figure 4.2.15: Epi-CARS of DMMP deposited on stainless steel for 0.01 s (green line), 0.1 s (blue line), 1 s (red line) and 10 s (black line) integration times.

Table 4.4: SNR of DMMP strongest Raman line as a function of spectral averaging, with DMMP deposited onto a stainless steel substrate.

Averaging	1	10	100	1000
SNR	30	130	450	800

As expected, the SNRs are severely reduced with respect to the ones obtained with the transmission setup, however, since DMMP is a good Raman scatterer we still have a good quality result for acquisition time of 1 s and 10 s: the non-resonant background is almost totally rejected, and all main spectral features under investigation are clearly identified and resolved. This feature is shown in Fig. 4.2.16, where the comparison between the spectrum of DMMP obtained with an acquisition time of 10 s with epi-CARS (top red line) and the Spontaneous Raman spectrum of DMMP [5] as measured using a commercial Raman spectrometer (bottom black line).

It is worth noting that the spectral shape of the epi-CARS spectra and spontaneous Raman spectra are slightly different, this is because of two main reasons: first, the spectral profile of a CARS resonance is always altered to some extent by the presence of non-resonant background contribution, which makes

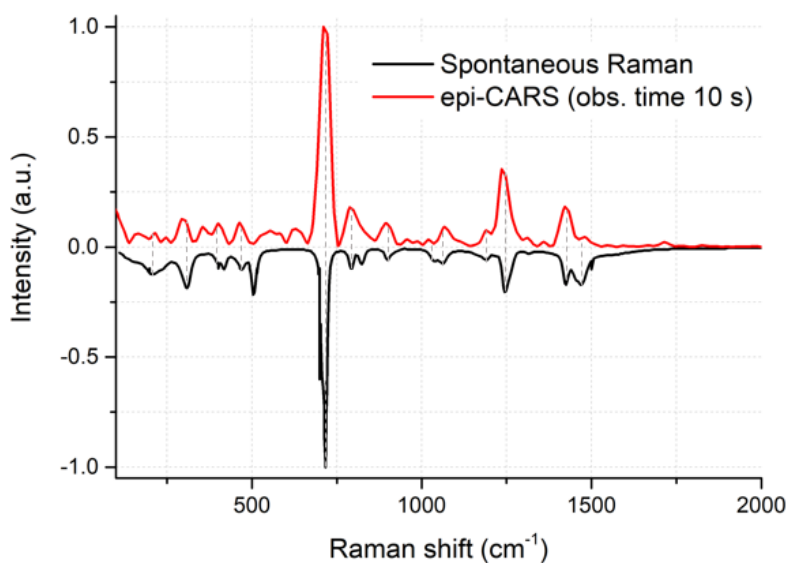


Figure 4.2.16: Epi-CARS spectrum of DMMP as measured with acquisition time 10 s (red line), and spontaneous Raman spectrum (black line) [5].

the profile slightly different with respect to the spontaneous Raman resonance; second, the relative intensity of the CARS peaks depend on the power content of the excitation source at the Raman shift of interest, which in turn depends on the spectral profile of the pump laser.

Consider now TDG deposited on stainless steel. Fig. 4.2.17 shows the epi-CARS spectrum of TDG deposited on stainless steel substrate as measured with integration times of 0.01, 0.1, 1, and 10 s; Table 4.5 shows the corresponding SNRs.

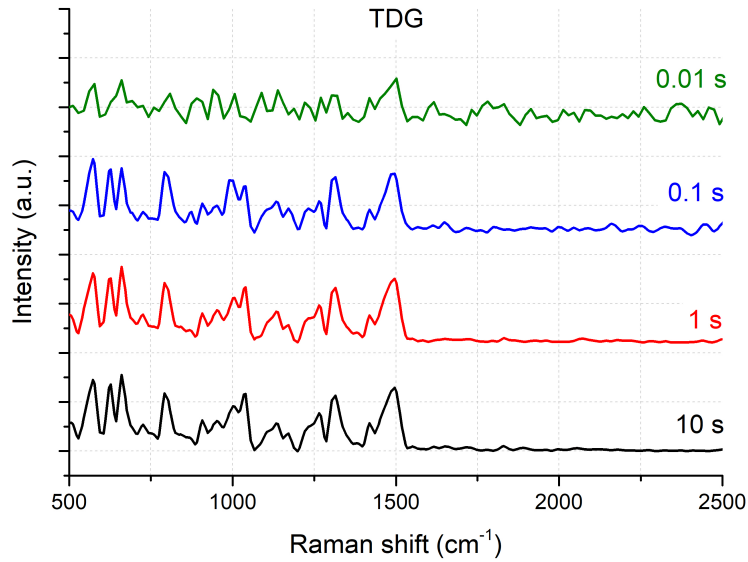


Figure 4.2.17: Epi-CARS of TDG deposited on stainless steel for 0.01 s (green line), 0.1 s (blue line), 1 s (red line) and 10 s (black line) integration times.

Table 4.5: SNR of TDG strongest Raman line as a function of spectral averaging, with TDG deposited onto a stainless steel substrate.

Averaging	1	10	100	1000
SNR	8	45	72	250

As expected, TDG is a much weaker Raman scatterer with respect DMMP as one can see comparing the SNRs. However, we still have good quality results for acquisition times of 1 s and 10 s. Fig. 4.2.18 shows in fact how all the main spectral features are identified.

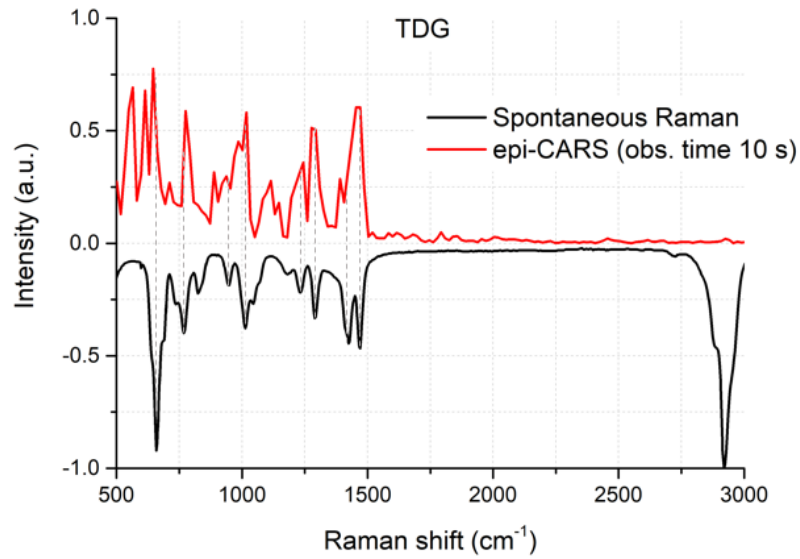


Figure 4.2.18: Epi-CARS spectrum of TDG as measured with acquisition time 10 s (red line), and spontaneous Raman spectrum (black line) [5].

Last, we consider TEHP deposited on stainless steel. As discussed before, TEHP, as TDG is a weak Raman scatterer, so the detection in this configuration was expected to be challenging. Fig. 4.2.19 shows the epi-CARS spectrum of TEHP deposited on stainless steel substrate as measured with integration times of 0.01, 0.1, 1, and 10 s; Table 4.6 shows the corresponding SNRs.

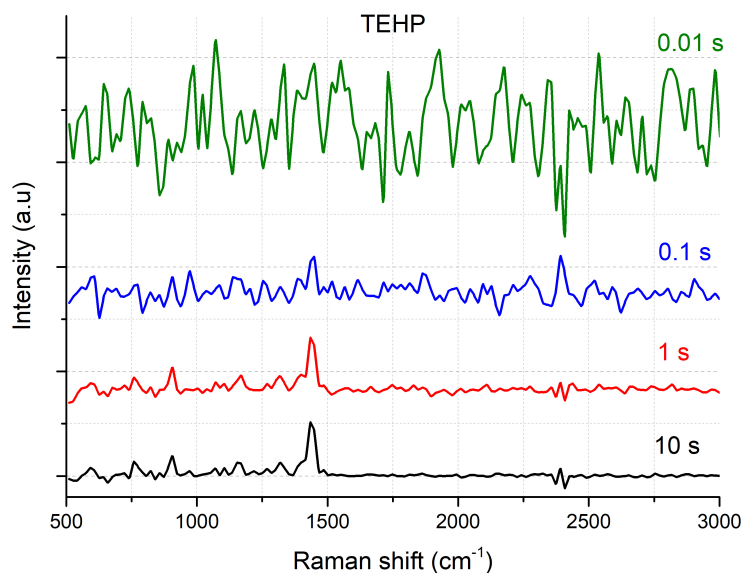


Figure 4.2.19: Epi-CARS of TEHP deposited on stainless steel for 0.01 s (green line), 0.1 s (blue line), 1 s (red line) and 10 s (black line) integration times.

Table 4.6: SNR of TEHP strongest Raman line as a function of spectral averaging, with TEHP deposited onto a stainless steel substrate.

Averaging	1	10	100	1000
SNR	-	2	32	80

As one can see, TEHP resulted as the worst substance to detect in this configuration. The spectrum is completely hidden by noise with a single acquisition and the SNRs at larger acquisition times are low even compared with the ones obtained with TDG. Even in this case however, considering the spectrum obtained at 10 s acquisition time, it is still possible to identify the main spectral features of the substance, as shown in Fig 4.2.20.

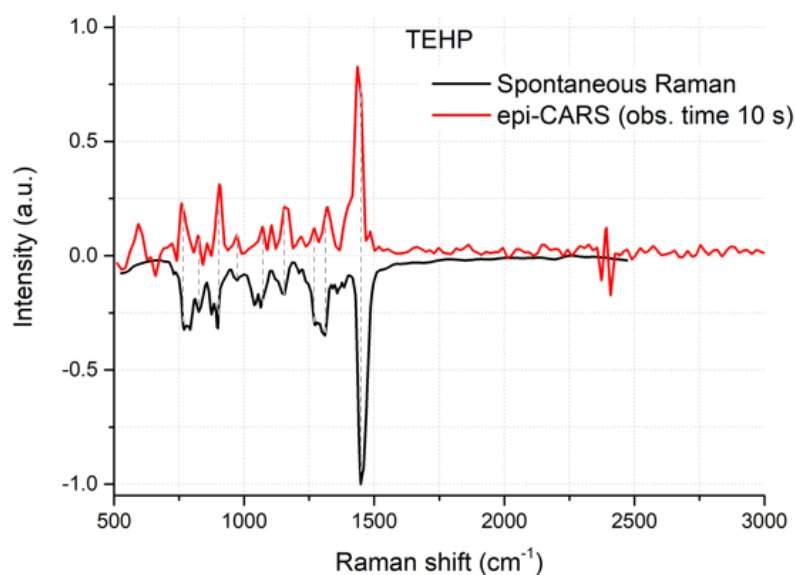


Figure 4.2.20: Epi-CARS spectrum of TEHP as measured with acquisition time 10 s (red line), and spontaneous Raman spectrum (black line) [5].

Overall, the spectral quality obtained with integration time of 1 s and 10 s is high and all main spectral features of all three samples under investigation are clearly identified and resolved. A machine learning algorithm for rapid identification of the samples has been developed and preliminary tested on the acquired spectra under various experimental conditions, and all samples have been identified with no occurrence of errors.

It is also possible to make a comment about the limit of detection (LOD), defined here as the minimum volume of sample that could be detected with a SNR higher than 10, allowing for clear identification of the agent under analysis. As discussed above, all experiments have been performed on a sample volume probed by the laser beam that is estimated to be 0.4 fL (1 fL = 10^{-15} L). Considering the SNRs we obtained, DMMP can be detected over stainless-steel with a LOD of 0.4 fL and integration times of only 10 ms. TDG on stainless-steel has a LOD of 0.4 fL at integration times of 100 ms. TEHP on stainless-steel has a LOD of 0.4 fL at integration times of 1 s.

Consider now the chemicals deposited on the glass surface. Fig. 4.2.21 shows the epi-CARS spectrum of DMMP deposited over the surface of a fused silica slide, as measured with integration times of 0.01, 0.1, 1, and 10 s; Table 4.7 shows the corresponding SNRs.

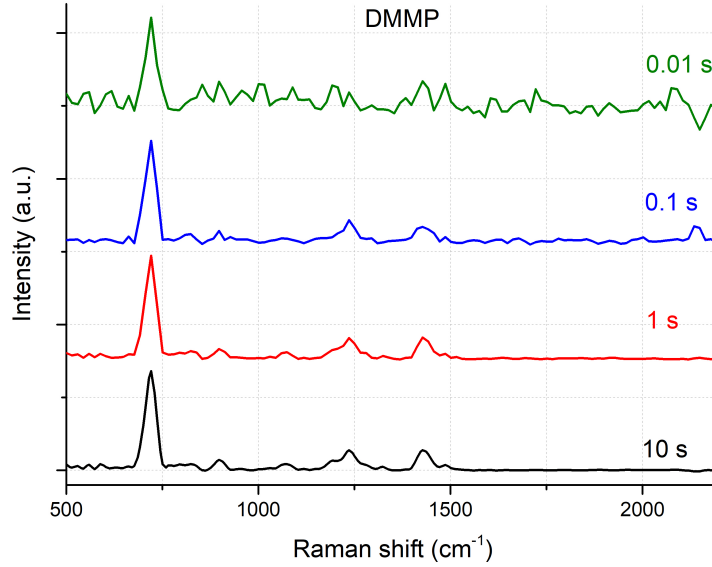


Figure 4.2.21: Epi-CARS of DMMP deposited on glass for 0.01 s (green line), 0.1 s (blue line), 1 s (red line) and 10 s (black line) integration times.

Table 4.7: SNR of DMMP strongest Raman line as a function of spectral averaging, with DMMP deposited onto a glass substrate.

Averaging	1	10	100	1000
SNR	15	90	300	650

It is worth noting that the SNR ratio observed with DMMP deposited on glass is similar to that observed on stainless-steel. This is due to the different reflecting and scattering properties of the surfaces: the stainless-steel surface has a high reflectance of around 70% at 800-900 *nm* and it is sand-blasted, so that the forward generated CARS beam is mainly back-scattered; on the other hand, the glass surface has low reflectance, but it is polished to optical quality and the CARS beam is back-reflected (no scattering), hence the higher spatial quality (improved collimation and focusing to the avalanche detector) of the pure back-reflected beam compensates for the lower reflectance of the glass surface, yielding an overall SNR similar to that observed with stainless-steel. More specifically, the detected CARS signal with glass substrate is due to pure Fresnel reflection of the forward generated CARS primarily at the interface between sample and glass. As the refractive index of the samples and glass are very similar ($n_{FS} = 1.45$, $n_{TDG} = 1.51$, $n_{TEHP} = 1.44$, $n_{DMMP} = 1.41$ at 1030 *nm*)

actually the amount of reflection is very low. A secondary reflection contribution from the interface between glass and air below the substrate could also contribute to the measured signal, however, as the glass substrate has a thickness of 1 mm, there is low matching to the imaging condition for back-collection by the focusing lens, due to high divergence of the focused beam.

In Fig. 4.2.22, the comparison between the spectrum of DMMP obtained with an acquisition time of 10 s with epi-CARS (top red line) and the Spontaneous Raman spectrum of DMMP [5] as measured using a commercial Raman spectrometer (bottom black line).

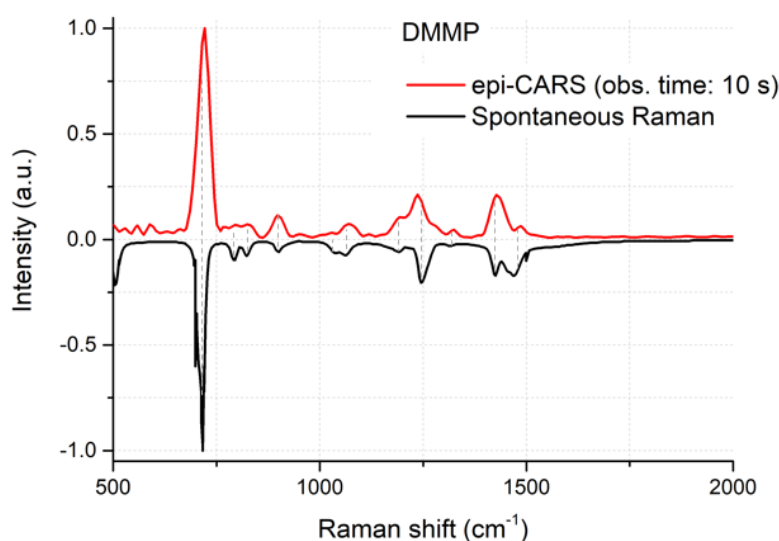


Figure 4.2.22: Epi-CARS spectrum of DMMP as measured with acquisition time 10 s (red line), and spontaneous Raman spectrum (black line) [5].

One can see that DMMP can be detected over glass with a LOD of 0.4 fL and integration time of only 10 ms.

Epi-CARS detection of TDG and TEHP was not possible with the fused silica substrate: even though the interferograms were visible in the time domain, the corresponding spectra in frequency domain were barely recognizable due to very low SNR. This is ascribed to the reduced strength of TDG and TEHP as Raman scatterers with respect to DMMP. Detection of TDG and TEHP over glass substrate would require working on the detection section to increase the sensitivity.

As a final test, we tried to proceed with the identification of CWAs deposited onto a packed sand substrate, obtained by pressing purified SiO₂ powder to a round shape. However, Epi-CARS detection of DMMP, TEHP and TDG was not possible on this substrate. The interferograms could be seen in the time domain, however the corresponding spectra in the frequency domain were characterized by very low SNR, so that identification of the spectral fingerprint was not possible. This was not expected, as actually the packed sand substrate

is white colored and hence it provides high reflection in the wavelength range where the CARS signal is detected (800-900 nm). The low SNR is ascribed to the porousness nature of the substrate: few seconds after deposition onto the substrate, the sample is completely absorbed by the substrate itself, so that the medium probed by the laser beam during epi-CARS measurement is a mixture of sand and deposited sample, where actually sand represents the main components (estimated sand concentration >90%). As a consequence, the resulting epi-CARS signal is reduced to a level below the sensitivity of the detector. Again, detection of DMMP, TDG and TEHP over packed sand substrate would require working on the detection section to increase the sensitivity.

In conclusion, the activities developed within this project have shown the feasibility of epi-CARS detection of relevant CWA simulants deposited on different substrates. All CWAs simulants have been detected on stainless steel at high spectral quality with integration times of 1 s. DMMP was clearly detected also on fused silica glass with integration time of 1 s. One main limitation of the present experimental setup is the relatively low sensitivity, which prevented the observation of epi-CARS spectra of TDG and TEHP on glass substrate and of all the CWAs onto the sand substrate. The avalanche silicon photodiode used in the present setup is actually already very sensitive, however, the detection of back-scattered beam is extremely challenging due to the very low power levels available at the detector. Photomultiplier tube would be the best choice for the measurement performed within this study, with much better figures of merit in terms of noise floor and gain.

In addition, the pulse repetition frequency of the system should be changed to lower frequency in order to reduce the average power incident onto the sample. This would be beneficial for reducing the risk of damage to the substrate and for inhibiting sample evaporation.

Transmission Configuration with a Resonant Galvo-Mirror

The previous version of the system was designed to operate at an acquisition rate of 100 spectra/s, mainly limited by the rotation speed of the non-resonant galvo-mirror. This is why we tested one last configuration, this time using a resonant galvo-mirror CRS4kHz by the company Cambridge Technology: the scanning arm features a rapid delay scanner that consists of a resonant scanner operating at frequency of 4 kHz. The delay scanner will allow for delay scanning of 2.5 mm at the frequency of 4 kHz, corresponding to a resolution in the Raman spectrum of 5 cm^{-1} .

Apart from the new resonant galvo-mirror, the setup is in the same transmission configuration shown in Fig. 4.1.1. All the other parameters (incident power on the sample $\approx 400\text{ mW}$, ...) are left unchanged. As mentioned before, being this galvo-mirror very fast and piloted by a sine wave, the delay is introduced in a non-linear way, thus the resampling using the He-Ne interferograms is exploited as will be discussed in Section 4.3.

First of all we started with acetonitrile, to align and test the new setup, together with the new sampling method. Fig. 4.2.23 shows acetonitrile spectra as measured with a single acquisition, 10, 100 and 1000 averages, corresponding to 125 μs , 1.25 ms, 12.5 ms and 125 ms respectively.

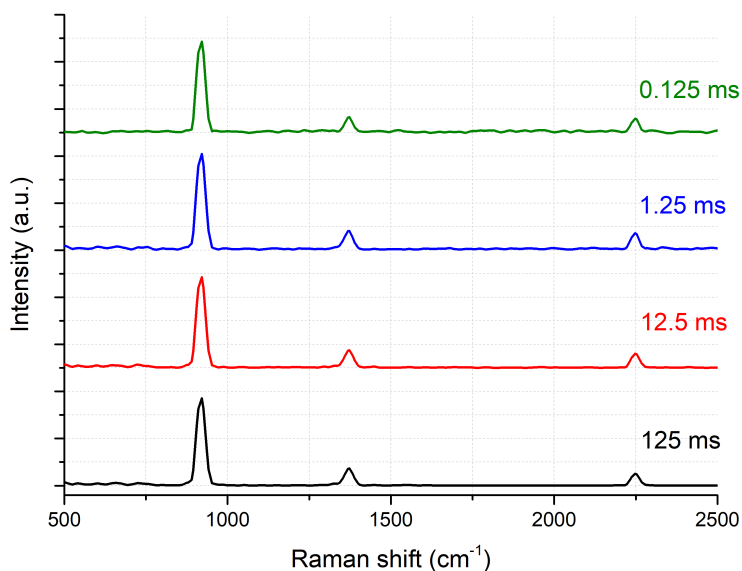


Figure 4.2.23: CARS of acetonitrile for a single acquisition (green line), 10 (blue line), 100 (red line) and 1000 (black line) averages, at 4kHz.

One can see that now, good quality spectra can be obtained much faster than with the previous configuration.

In order to test the potential of the setup as a CWAs fast detecting system, we measured DMMP, given its good Raman response. Fig. 4.2.24 shows spectra as measured with integration times 125 μ s, 1.25 ms, 12.5 ms and 125 ms; Table 4.8 shows the corresponding SNRs.

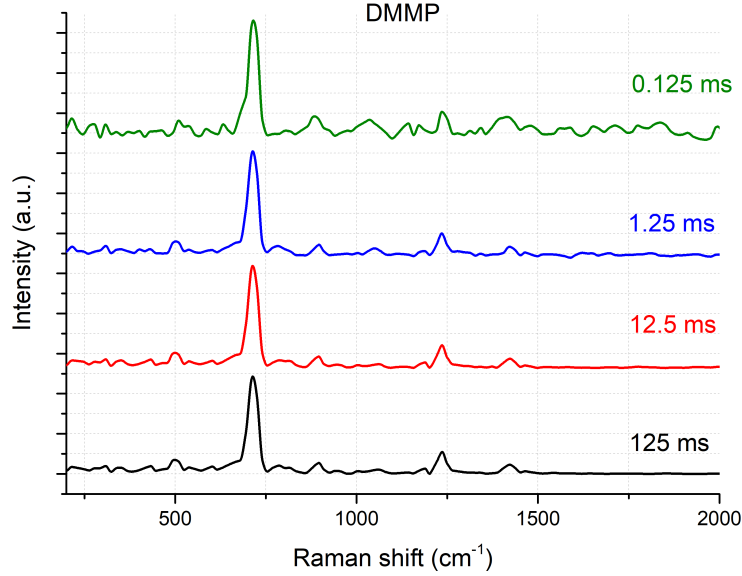


Figure 4.2.24: CARS of DMMP for 125 μ s (green line), 1.25 ms (blue line), 12.5 ms (red line) and 125 ms (black line) integration times.

Table 4.8: SNR of DMMP strongest Raman line as a function of spectral averaging at 4 kHz.

Averaging	1	10	100	1000
SNR	30	120	480	1500

We can see high quality spectra are already obtained at 12.5 ms, against the 1 s threshold of the previous configuration. However, the SNRs obtained in this case were kind of unexpected. Being this a transmission configuration, we expected the SNRs to be comparable with the one reported in Table 4.1. Instead, the SNRs obtained in this case, even though very good, are significantly lower. A possible explanation for this result is ...

In any case, we can see that the system is still able to detect all the main spectral features of the sample under analysis as shown in Fig 4.2.25, where the spectra of DMMP obtained with an acquisition time of 125 ms is compared with the spontaneous Raman spectrum of DMMP [5].

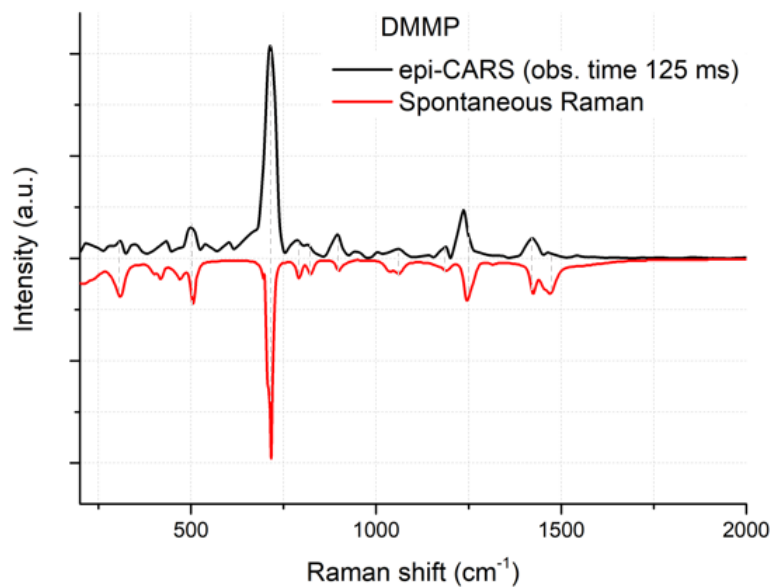


Figure 4.2.25: CARS spectrum of DMMP as measured with acquisition time 125 ms (red line), and spontaneous Raman spectrum (black line) [5].

This result prove the potential of this configuration for fast detection and identification of CWAs. The next step would be to test again this setup in a backreflection configuration.

4.3 Sampling Process

As mentioned before, a beam from a helium-neon (He-Ne) laser is spatially combined with the Yb-laser and the continuous interference signal of the He-Ne laser is detected with a photodiode after the interferometer. This signal is used as an external clock for data sampling, which calibrates the nonlinear optical-path-length-difference that comes along with the rapid-scan interferometer, in particular, samples are collected when the interferograms cross the zero value. As discussed, in our first implementations of the system we use a non-resonant galvo-mirror, piloted with a ramp signal at 100 Hz. Fig. 4.3.1 shows the corresponding interferogram of the He-Ne.

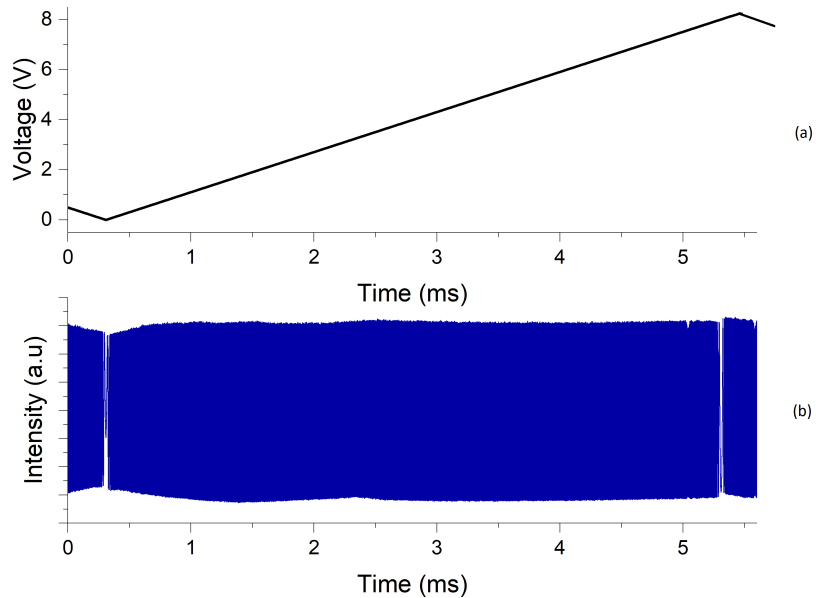


Figure 4.3.1: (a) Ramp signal at 100 Hz used to pilot the galvo-mirror; (b) Interferogram of the He-Ne.

This interferogram can be also used to characterize the interferometer. As one would expects, when we get to the ramp edges and we have the inversion of direction of the galvo-mirror, the interferogram is distorted, as better shown in Fig. 4.3.2. This means that in these cases, the delay is introduced strongly non-linearly. This is natural and these areas of the interferograms can be easily avoided by placing the trigger afterwards.

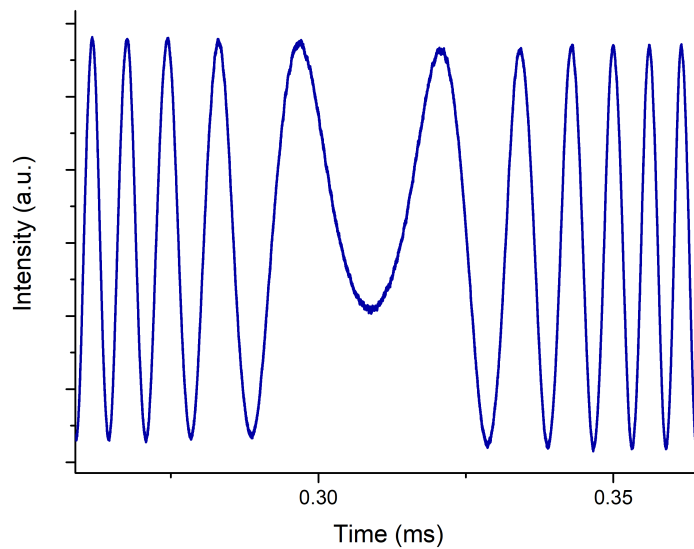


Figure 4.3.2: Distorted interferogram at the edges of the ramp.

Even though we are using a ramp, the delay is not introduced in a completely linear way. This is the reason why asynchronous sampling is not optimal, leading to a distortion of the collected spectrum, with respect to the result obtained with synchronous sampling by means of the He-Ne interferograms. This claim is confirmed by Fig. 4.3.3, where the spectrum of acetonitrile acquired with 1000 averages is shown, using asynchronous and synchronous sampling, using a ramp signal.

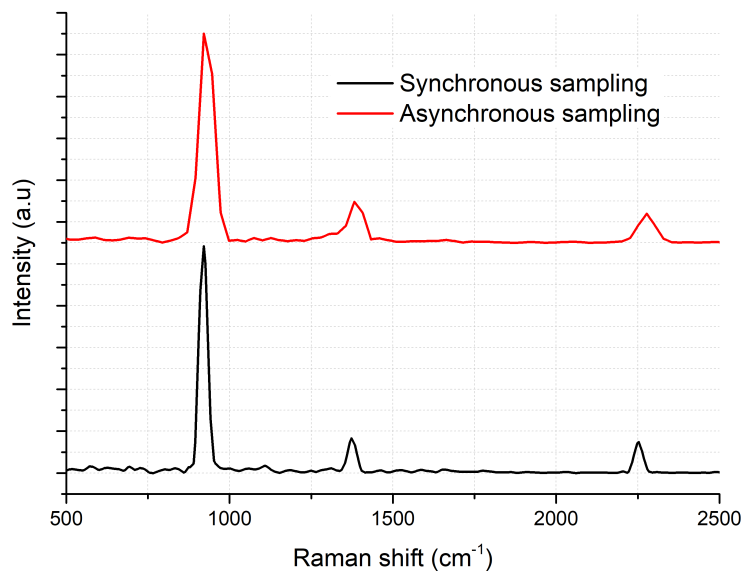


Figure 4.3.3: Comparison between acetonitrile measured with 1000 averages, using asynchronous (red line) and synchronous (black line) sampling, using a ramp signal at 100 Hz.

As one can see, the asynchronous sampling returns a meaningful spectrum, where the main spectral features are still identified, but with larger Raman lines. This broadening is due to the fact that the linear sampling is not completely suitable even in the favorable case of a ramp signal.

The same argument is better demonstrated considering a sine wave at 100 Hz as a piloting signal for the galvo-mirror, as shown in Fig. 4.3.4.

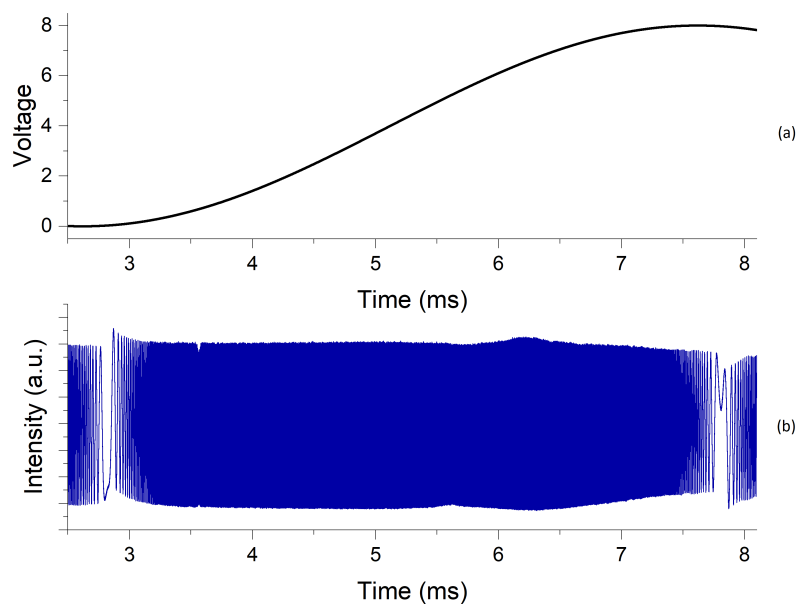


Figure 4.3.4: (a) Sine signal at 100 Hz used to pilot the galvo-mirror; (b) Interferogram of the He-Ne.

Again at the inversion of direction of the galvo-mirror, we have a distortion of the interferogram as discussed before. Moreover, since we are using a sine wave, the delay is introduced in a severe non-linear way, thus the usual sampling process is not suitable at all to get good quality spectra.

This is better demonstrated in Fig. 4.3.5. It shows the spectrum of acetonitrile acquired with 1000 averages, using asynchronous and synchronous sampling, using a sine signal.

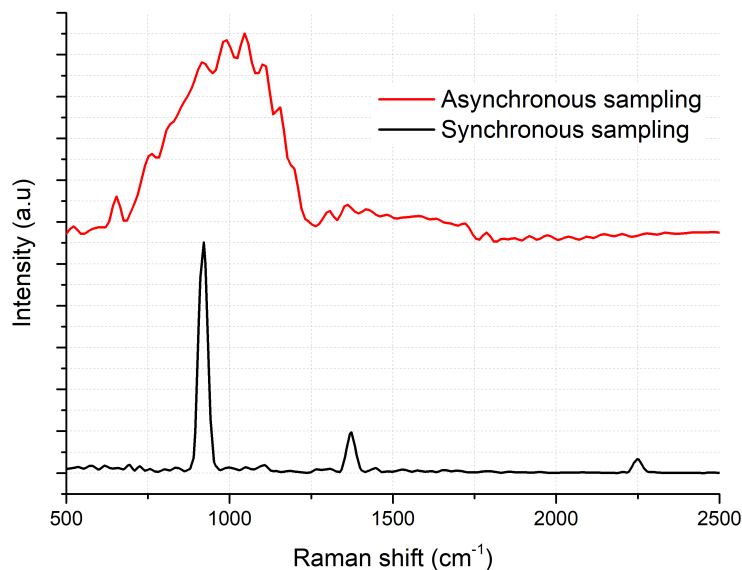


Figure 4.3.5: Comparison between acetonitrile measured with 1000 averages, using asynchronous (red line) and synchronous (black line) sampling, using a sine signal at 100 Hz.

With respect to the case of the ramp signal, the broadening is much more severe and the result is a spectrum where the main spectral features are completely lost and the result is thus meaningless.

This result shows how using a sine wave requires synchronous sampling to get a non-meaningless spectrum. Moreover, we expect the broadening to be even worse the higher is the speed of the galvo-mirror. This is interesting since in our last iteration of the system, we used a resonant galvo-mirror, oscillating at 4 kHz, piloted by a sine wave. The interferogram in this case is shown in Fig. 4.3.6.

Again, we can compare the spectra of acetonitrile obtained with asynchronous and synchronous sampling. The comparison is reported in Fig. 4.3.7.

We can see again that the spectrum is meaningless due to the distortion given by asynchronous sampling, thus the resampling using He-Ne is required.

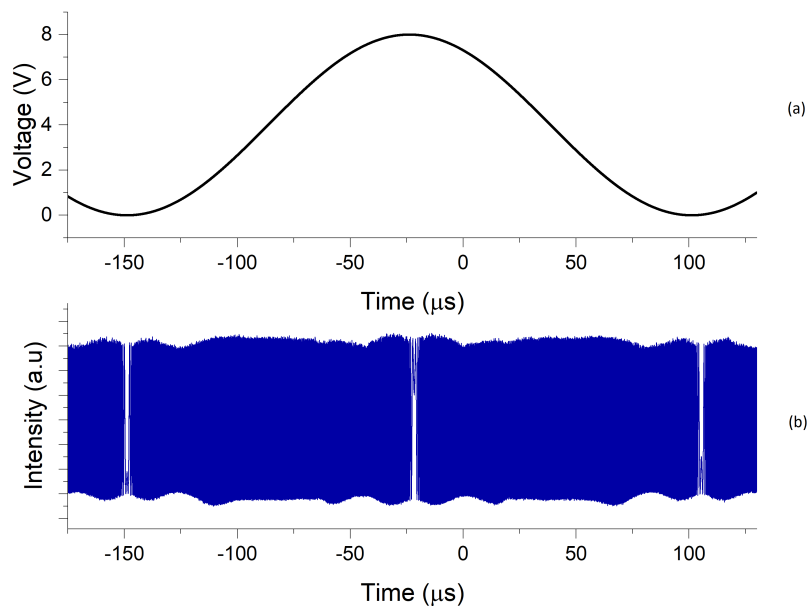


Figure 4.3.6: (a) Sine signal at 4 kHz used to pilot the galvo-mirror; (b) Interferogram of the He-Ne.

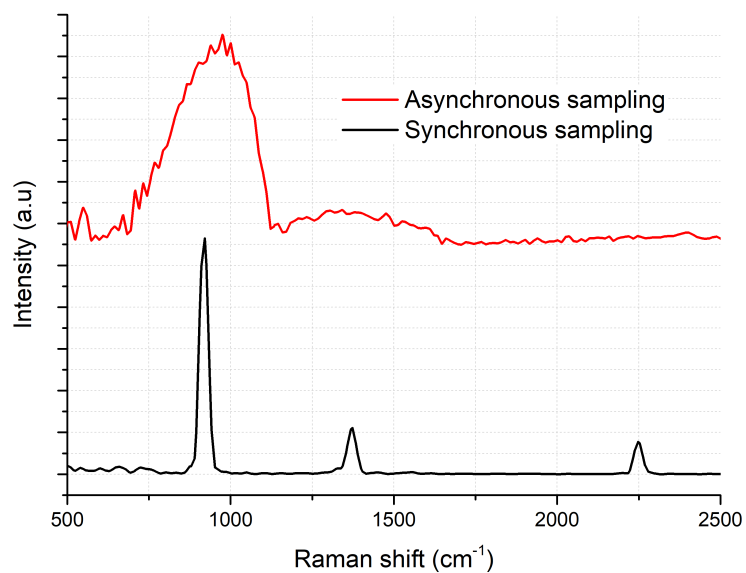


Figure 4.3.7: Comparison between acetonitrile measured with 1000 averages, using asynchronous (red line) and synchronous (black line) sampling, using a sine signal at 4 kHz.

Chapter 5

Conclusions

In conclusion, the activities developed within this project have shown the feasibility CARS detection of relevant CWAs simulants in a transmission configuration and of epi-CARS detection on different substrates. The CWA simulants used for experiments were TDG, TEHP, and DMMP, whereas the substrates were stainless steel, fused silica glass, and packed sand. All CWAs simulants have been detected in the transmission configuration and on stainless steel at high spectral quality with integration times of 1 s. DMMP was clearly detected also on fused silica glass with integration time of 1 s. Samples could not be detected on packed sand due to low SNR. The transmission configuration was also tested with a faster resonant galvo-mirror which let us detect high quality spectra with integration times of few ms.

One main limitation of the present experimental setup is the relatively low sensitivity, which prevented the observation of epi-CARS spectra of TDG and TEHP on glass substrate, and of all samples on packed sand. The avalanche silicon photodiode used in the present setup is actually already very sensitive, however, the detection of back-scattered beam is extremely challenging due to the very low power levels available at the detector. Photomultiplier tube would be the best choice for the measurement performed within this study, with much better figures of merit in terms of noise floor and gain.

We were able to obtain such results by successfully generating ultra-short pulses centered at 1030 nm with our scheme based on a low power Yb oscillator followed by an Yb fiber amplifier and achieving almost pure SPM in a subsequent PCF. However, the system performance would benefit from the adoption of a commercial Yb-fiber laser in substitution of the present scheme. In fact, the footprint of the system would be greatly reduced and all optical components would be integrated over a single platform so that the system stability (short- and long-term) would be improved.

In addition, the pulse repetition frequency of the system should be changed to lower frequency in order to reduce the average power incident onto the sample. This will be beneficial for reducing the risk of damage to the substrate and for inhibiting sample evaporation.

Bibliography

- [1] Rüdiger Paschotta. Saturable absorbers.
- [2] Wei Liu. *Advanced ultrafast fiber laser sources enabled by fiber nonlinearities*. PhD thesis, Universität Hamburg, 2016.
- [3] Thorlabs. *GVS001 and GVS002, Scanning Galvo Systems*.
- [4] Cambridge Technology. *CRS Series, Resonant Scanners*.
- [5] Sigma-aldrich online database.
- [6] Vasuki Durairaj. *Amplification in Ytterbium-doped fibers*. PhD thesis, Aalto Univeristy, 2013.
- [7] Orazio Svelto. *Principi dei Laser (Italian) [Principles of Laser]*. Plenum Press, 1976.
- [8] Ursula Keller; Lukas Gallmann. Ultrafast laser physics, chapter 8: Passive modelocking.
- [9] Rüdiger Paschotta. Bragg mirrors.
- [10] Mauro Nisoli. *Semiconductor Photonics, Principles and Applications*. Società Editrice Esculapio, 2016.
- [11] Rsam - resonant saturable absorber mirror. Technical report, BATOP GmbH.
- [12] J. Hecht. Optical amplifiers. *Photonics New*, 2002.
- [13] A. Tünnermann; T. Schreiber and J. Limpert. Fiber lasers and amplifiers: an ultrafast performance evolution. *Applied optics*, 49(25), 2010.
- [14] E. Snitzer; H. Po; F. Hakimi; R. Tumminelli and B. C. McCollum. Double-clad, offset core nd fiber laser. In *Optical Fiber Sensors*. Optical Society of America, 1988.
- [15] M. H. Muendel. Optimal inner cladding shapes for double-clad fiber lasers. In *Lasers and Electro-Optics*, 1996.
- [16] D. Kouznetsov and J. V. Moloney. Efficiency of pump absorption in double-clad fiber amplifiers. iii. calculation of modes. *Journal of the Optical Society of America B*, 19(6), 2002.

- [17] Robert W. Boyd. *Nonlinear Optics*. Academic Press, 2003.
- [18] Jean Toulouse. Optical nonlinearities in fibers: review, recent examples, and systems applications. *Journal of Lightwave Technology*, 2005.
- [19] Robert Hellwarth; Joel Cherlow and Tien-Tsai Yang. Origin and frequency dependence of nonlinear optical susceptibilities of glasses. *Physical Review B*, 1975.
- [20] RW Hellwarth. *Progress in Quantum Electronics*, chapter Third-order optical susceptibilities of liquids and solids. 1977.
- [21] Stephen Jacobs; Murray Sargent III; James F Scott and Marlan O Scully. *Physics of Quantum Electronics Vol. 2: Laser Applications to Optics and Spectroscopy*. 1975.
- [22] Govind P Agrawal. *Nonlinear fiber optics*. Academic press, 2007.
- [23] D. Kassegne; S. S. Ouro-Djobo; B-M. Mao; G. Djanta; K. Sagna. Impact of self-steepening and stimulated raman scattering effects in a wavelength division multiplexing system. *International Journal of Advanced Research in Electrical, Electronics and Instrumentation Engineering*, 2017.
- [24] G'abor Keresztury. Raman spectroscopy: Theory. *John Wiley & Sons Ltd*, 2002.
- [25] Takuro Ideguchi. *Nonlinear Dual-Comb Spectroscopy*. PhD thesis, Ludwig Maximilians Universität München, 2014.
- [26] Cinzia Emmanuello. Comparison of spontaneous and coherent raman spectroscopy for biophysical analysis. Master's thesis, Politecnico di Milano, 2017.
- [27] Miu Tamamitsu; Yusuke Sakaki; Tasuku Nakamura; G. Krishna Podagatlapalli; Takuro Ideguchi and Keisuke Goda. Ultrafast broadband fourier-transform cars spectroscopy at 50000 spectra/s enabled by a scanning fourier-domain delay line. *Vibrational Spectroscopy*, 91:163–169, 2017.
- [28] Ji-Xin Cheng; X. Sunney Xie and E. Potma. Coherent anti-stokes raman scattering microscopy. *Handbook of Biological Confocal Microscopy*, 2006.
- [29] H. Graener and A. Laubereau. High resolution fourier transform raman spectroscopy with ultrashort laser pulses. *Optics Communications*, 54:141–146, 1985.
- [30] A. Volkmer; L. D. Book and X. Xie. Time-resolved coherent anti-stokes raman scattering microscopy: Imaging based on raman free induction decay. *Applied Physics Letters*, 80:1505–1507, 2002.
- [31] J. P. Ogilvie; E. Beaurepaire; A. Alexandrou and M. Joffre. Fourier-transform coherent anti-stokes raman scattering microscopy. *Opt. Lett.*, 31(4):480–482, 2006.
- [32] N. Dudovich; D. Oron and Y. Silberberg. Single-pulse coherently controlled nonlinear raman spectroscopy and microscopy. *Nature*, 418:5, 2002.

- [33] Yong-Xin Yan; Edward B. Gamble Jr.; and Keith A. Nelson. Impulsive stimulated scattering: General importance in femtosecond laser pulse interactions with matter, and spectroscopic applications. *J. Chem. Phys.*, 83(5391), 1985.
- [34] J. K. Ranka; R. S. Windeler and A. J. Stenz. *Opt. Lett.*, 25(25), 2000.
- [35] R. R. Alfano and S. L. Shapiro. *Phys. Rev. Lett.*, 24(587), 1970.
- [36] Haohua Tu and Stephen Boppart. Coherent fiber supercontinuum for biophotonics. *Laser Photonics Rev.*, 7(5):628–645, 2013.
- [37] Haohua Tu; Yuan Liu; Jesper Lægsgaard; Utkarsh Sharma; Martin Siegel; Daniel Kopf and Stephen A. Boppart. Scalar generalized nonlinear schrödinger equation-quantified continuum generation in an all-normal dispersion photonic crystal fiber for broadband coherent optical sources. *Optics Express*, 18(26), 2010.
- [38] Yuan Liu; Youbo Zhao; Jens Lyngsø; Sixian You; William L. Wilson; Haohua Tu and Stephen A. Boppart. Suppressing short-term polarization noise and related spectral decoherence in all-normal dispersion fiber supercontinuum generation. *Journal of Lightwave Technology*, 33(9):1814–1820, 2015.
- [39] Kazuki Hashimoto; Junko Omachi and Takuro Ideguchi. Ultra-broadband rapid-scan fourier-transform cars spectroscopy with sub-10-fs optical pulses. *Optics Express*, 26(11), 2018.
- [40] Kazuki Hashimoto; Megumi Takahashi; Takuro Ideguchi and Keisuke Goda. Broadband coherent raman spectroscopy running at 24,000 spectra per second. *Scientific Reports*, 6(21036), 2016.
- [41] Qi Zheng; Yong chun Fu and Jia qiang Xu. Advances in the chemical sensors for the detection of dmmp — a simulant for nerve agent sarin. *Procedia Engineering*, 7:179–184, 2010.
- [42] National Academies of Sciences Engineering and Medicine. *Assesing Health Outcomes Among Veterans of Project SHAD (Shipboard Hazard and Defense)*. Washington, DC : the National Academic Press, 2016.
- [43] Beer; Sikarwar Bhavna; Sharma Pushpendra K.; Singh Virendra V.; Boopathi Mannan; Singh and Jaiswal Yogesh K. Xanthine oxidase immobilized electrode for electrochemical sensing of chemical warfare agent simulant. *Sensor Letters*, 15(3):227–235, 2017.